

ELECTROSTATIC INTERACTIONS OF BIOLOGICAL PROCESSES: CELLULAR
INTERNALIZATION OF PANCREATIC-TYPE RIBONUCLEASES AND SALT-BRIDGE
FORMATION IN A DNA-WRAPPING PROTEIN

by

Nadia K. Sundlass

A dissertation submitted in partial fulfillment of the requirements for the degree of

Doctor of Philosophy

(Biophysics)

at the

UNIVERSITY OF WISCONSIN-MADISON

2011

ELECTROSTATIC INTERACTIONS OF
BIOLOGICAL PROCESSES: CELLULAR
INTERNALIZATION OF PANCREATIC-TYPE
RIBONUCLEASES AND SALT-BRIDGE
FORMATION IN A DNA-WRAPPING PROTEIN

submitted to the Graduate School of the
University of Wisconsin-Madison
in partial fulfillment of the requirements for the
degree of Doctor of Philosophy

By

Nadia Sundlass

Date of final oral examination: October 6, 2011

Month and year degree to be awarded: December 2011

The dissertation is approved by the following members of the Final Oral Committee:

Ronald T. Raines, Professor of Biochemistry and Chemistry

Qiang Cui, Professor of Chemistry

Deane F. Mosher, Professor of Medicine

M. Thomas Record, Professor of Biochemistry and Chemistry

Alessandro Senes, Assistant Professor of Biochemistry

ELECTROSTATIC INTERACTIONS OF BIOLOGICAL PROCESSES: CELLULAR
INTERNALIZATION OF PANCREATIC-TYPE RIBONUCLEASES AND SALT-BRIDGE
FORMATION IN A DNA-WRAPPING PROTEIN

Nadia K. Sundlass

Under the supervision of Professor Ronald T. Raines

At the University of Wisconsin–Madison

Pancreatic-type ribonucleases were studied extensively in the 20th century and have produced a wealth of knowledge about protein structure, protein function, and enzyme catalysis. The 21st century brings a new era in which ribonucleases are being developed as potential clinical therapeutics in a wide variety of fields.

In order for ribonucleases to be cytotoxic to cells, the ribonuclease must be internalized through endocytosis. Secondly, the ribonuclease must escape from the endosomal pathway by crossing the membrane. Once in the cytosol, the ribonuclease must be able to evade ribonuclease inhibitor (RI) in order to catalyze the degradation of RNA, which triggers the apoptotic cascade within the cell. This thesis focuses on the role of electrostatics in the internalization and endosomal escape of ribonucleases.

The three homologous members of the pancreatic-type ribonuclease superfamily studied in this thesis are Onconase (amphibian), RNase A (bovine), and RNase 1 (human). Increasing the surface positive charge of ribonucleases has been associated with increased cellular uptake and cytotoxicity. Additionally, arginine residues have been shown to be more effective than

lysine residues at increasing cellular uptake of some peptides. In CHAPTER 2, the role of lysine and arginine residues in the cellular uptake and stability of Onconase is compared and contrasted through the use of a variety of experimental methods. In CHAPTER 3, the contribution of electrostatics to the binding of ONC, RNase A, and RNase 1 to model membranes is studied. By comparing experimental binding data with computational electrostatic calculations, we were able to show that whereas electrostatic forces are sufficient to explain the cellular uptake of ONC, the cellular uptake of RNase A and RNase 1 is much higher than expected based on electrostatic forces alone.

In CHAPTER 4, explicit MD simulations are used to study the effect of salt concentration on the behavior and formation of salt bridges in IHF, a DNA wrapping protein. CHAPTER 5 describes possible future directions of research regarding the future of ribonucleases as clinical therapeutics. Specifically, methods to increase cell specificity and pharmacological half-life are proposed therein.

Acknowledgements

I would like to take this opportunity to express gratitude towards the many people who have provided guidance, encouragement, and support during my graduate career. First, I would like to thank my advisor, Professor Ronald T. Raines, for his support, optimism, and patience. The opportunity to work in his research group has allowed me to grow both personally and professionally. I would also like to thank Professor Raines for his optimism and encouragement in science: After talking to Ron about my project or future career, I always believe that I can do anything that I want to do, a powerful sentiment.

My thesis committee members, past and present, Professor Tom Record, Dr. Deane Mosher, Professor Qiang Cui, Professor Alessandro Senes, Professor Arun Yethiraj, and Professor Jim Weisshaar have been very helpful through their probing questions and invaluable insight. I am deeply grateful to them for sharing their time, expertise, and thoughts with me.

Professor Qiang Cui has played a critical role in my development as a scientist. I would like to thank him for welcoming me to his group and for always leaving his office door open for me to ask questions and to learn from him and his group members. My research would not have been possible without him and current and former members of his research group, including Jejoong Yoo, Liang Ma, Shuo Yang, Zhe Wu, Puja Goyal, and Guanhua Hou.

I would like to thank Dr. Deane Mosher for displaying confidence in my ability to succeed as a physician–scientist and for sharing his wisdom and excellent advice with me. I would like to thank Professor Jim Skinner, Professor JR Schmidt, and Revati Kumar, Ben Auer, Yu Shan

Lin, and Justin Shorb for their support and advice starting from when I was an undergraduate and continuing through the present. I would like to thank my clinical mentors, Dr. Eliot Williams and Dr. Jim Svenson, Dr. Svenson, especially, has given me invaluable advice about balancing research and clinical medicine, about clinical decision-making, and about effective history taking, for which I'm very grateful..

My colleagues in the Raines Lab have always been willing to lend a helping hand and to give great feedback. I am grateful for the help of Matt Shoulders, Daniel Gottlieb, Rebecca Turcotte, Mike Levine, Margie Borra, and Kelly Gorres when I first joined the lab. Greg Ellis has been an invaluable source of information and help. Mike Palte, Joelle Lomax, Chelcie Eller, Sayani Chattopadhyay, Sean Johnston, Ben Caes, Rex Watkins, Cindy Chao, Eddie Myers, Langdon Martin, and Caglar Tanrikulu have all been wonderful colleagues and friends.

My friends outside of the lab have been an incredible source of strength to me. I would like to thank my fellow MSTPers, Stacy Valkenaar, Lisa Maurer, and Sarah Wernimont for being wonderful friends, for their support, and for our wonderful cross-discipline discussions. Izzy Smith, a member of the Biophysics Training Program, has been a great colleague and friend whose insightful questions and thoughts have always been helpful. I would also like to thank Katherine Rankin, the Biophysics Program Coordinator, and Paul Cook, the MSTP administrator, who have always been a great help and able to answer my questions.

Last but not least, I would like to thank my family and the Troiano's for always being there for me. You've encouraged me from a very early age to ask deep questions, have always believed that I can do anything I want to do, and have given me wonderful advice. Thank you.

Table of Contents

ELECTROSTATIC INTERACTIONS OF BIOLOGICAL PROCESSES: CELLULAR INTERNALIZATION OF PANCREATIC-TYPE RIBONUCLEASES AND SALT BRIDGE FORMATION IN A DNA-WRAPPING PROTEIN.....	i
Acknowledgements.....	iii
List of Tables	ix
List of Figures.....	x
List of Abbreviations	xii
CHAPTER 1	
Introduction: Electrostatic Interactions between Proteins and Lipid Bilayers	1
1.1 Abstract	2
1.2 Introduction.....	2
1.3 Pancreatic Ribonucleases.....	5
1.4 Ribonuclease–Cell Surface Interactions	6
1.5 Pancreatic Ribonuclease-Lipid Bilayer Interaction	8
1.6 Computational Analysis of Protein/Membrane Interactions.....	10
CHAPTER 2	
Arginine Residues are More Effective than Lysine Residues in Eliciting the Cellular Uptake of Onconase	19
2.1 Abstract	20

2.2	Introduction	20
2.3	Methods	23
2.3.1	Materials	23
2.3.2	Analytical Instruments	23
2.3.3	Production of Ribonucleases	24
2.3.4	Production of Labeled Ribonucleases	25
2.3.5	Assays of Catalytic Activity	26
2.3.6	Cytotoxicity Assays	27
2.3.7	Flow Cytometry Assays	27
2.3.8	Heparin-affinity Chromatography	28
2.3.9	Guanidine-HCl Induced Transition Curves	28
2.3.10	Protease Susceptibility	30
2.4	Result	30
2.4.1	Design, Production, and Purification of R-Onconase	30
2.4.2	Production and Purification of Labeled R-ONC	31
2.4.3	Catalytic Activity	32
2.4.4	Cellular Internalization	32
2.4.5	Heparin-affinity	32
2.4.6	Cytotoxic Activity	32
2.4.7	Conformational Stability	33
2.4.8	Protease Susceptibility	33
2.5	Discussion	34

CHAPTER 3

Contribution of Electrostatics to the Binding of Pancreatic Ribonucleases to Membrane.....44

3.1 Abstract45**3.2 Introduction45****3.3 Methods49**

3.3.1 Materials49

3.3.2 Analytical Instruments49

3.3.3 Production of Fluorescently-labeled Ribonucleases49

3.3.4 Large Unilamellar Vesicle Formation50

3.3.5 Protein-Liposome Binding Assay50

3.3.6 Poisson-Boltzmann Calculations51

3.3.7 IMM1-GC Calculations53

3.4 Results54

3.4.1 Production of Labeled Ribonucleases54

3.4.2 Ribonuclease-LUV Binding Affinity55

3.4.3 Poisson-Boltzmann Calculations56

3.4.4 IMM1-GC Simulations57

3.5 Discussion58

CHAPTER 4

Disruption and Formation of Surface Salt Bridges are Coupled to DNA Binding by

Integration Host Factor: A Computational Analysis72

4.1 Abstract73

4.2	Introduction	74
4.3	Methods	77
4.3.1	Molecular Dynamic Simulations of IHF in the Unbound State	77
4.3.2	Calculations of Protein Surface Electrostatic Potential.....	79
4.3.3	Prediction of DNA Binding Interface	80
4.3.4	Salt Dependence of Thermodynamics of Salt-Bridge Interactions	81
4.4	Results and Discussion	81
4.4.1	Overall Conformational Stability of IHF in the Absence of DNA	81
4.4.2	Salt Bridge Dynamics	83
4.4.3	Impact on the Prediction of DNA Binding Sites.....	91
4.5	Conclusions	93
 CHAPTER 5		
	Future Directions	119
5.1	Cellular Uptake of Pancreatic-type Ribonucleases.....	120
5.2	Pharmacological Targeting of Ribonucleases	121
5.3	Plasma Clearance of Ribonucleases	123
	REFERENCES	125

List of Tables

Table 3.1	Observed and calculated affinity of ribonucleases for a phosphatidylserine membrane.....	69
Table 3.2	Summary of IMM1–GC simulations	70
Table 4.1	Summary of salt-bridge activity for binding-site cationic residues.....	95
Table 4.2	Summary of salt bridge activity for non-binding site cationic activity	96
Table 4.3	Dependence of thermodynamic properties of K–Cl association on [KCl]	97

List of Figures

Figure 1.1	Structures of pancreatic-type ribonucleases.	16
Figure 1.2	Cytotoxic pathway of pancreatic-type ribonucleases	18
Figure 2.1	Three-dimensional structure of Onconase.....	38
Figure 2.2	Effect of arginine residues on the cellular uptake of Onconase.	39
Figure 2.3	Elution profile of ONC (A) and R-ONC (B) from immobilized heparin.....	40
Figure 2.4	Effect of arginine residues on the cytotoxicity of Onconase.....	41
Figure 2.5	Effect of arginine residues on the conformational stability of Onconase.	42
Figure 2.6	Effect of arginine residues on the protease susceptibility of Onconase.	43
Figure 3.1	Ribonuclease binding isotherms toward phosphatidylserine liposomes.	62
Figure 3.2	Computational calculation of the binding of RNase 1 to model membranes.....	63
Figure 3.3	Computational calculation of the binding of RNase A to model membranes.....	65
Figure 3.4	Computational calculation of ONC binding to model membranes	67
Figure 4.1	Structure of IHF.....	98
Figure 4.2	Conformational transitions in IHF observed within 50 ns MD simulations	99
Figure 4.3	Normalized histogram $H(r)$ of salt bridge distance.....	100
Figure 4.4	Behaviors of stable salt bridges involving binding-site cationic residues during MD simulations.....	101
Figure 4.5	Behaviors of binding-site cationic residues without significant salt-bridge formation during MD simulations	103
Figure 4.6	Behavior of salt-bridges of binding-site cationic residues in MD simulations ..	105

Figure 4.7 Behavior of non-binding site cationic residues with large rinit that engage in salt-bridge behavior during MD simulations.....	107
Figure 4.8 Behavior of non-binding-site cationic residues with small rinit values that demonstrate formation of salt-bridges during MD simulations.....	109
Figure 4.9 Behavior of non-binding site cationic residues with large rinit values that do not engage in significant salt-bridge interactions during MD simulations.....	112
Figure 4.10 Salt-bridge behavior of K20 β , a non-binding site cationic residue, during MD simulations.....	113
Figure 4.11 Behavior of cationic residues in IHF during MD simulations.	114
Figure 4.12 The positions of K3, K20, E23, D24, K27 on the β subunit.	116
Figure 4.13 Differential residue-averaged electrostatic potential ($\Delta\phi_{res}$) between the simulated apo structure and the crystal apo structure, mapped onto the crystal apo structure.	117
Figure 4.14 Results of DNA binding site prediction using two popular online servers.	118

List of Abbreviations

ϵ	extinction coefficient
6-FAM	6-carboxyfluorescein
6-TAMRA	6-carboxytetramethylrhodamine
BODIPY	boron-dipyrromethene
CD	circular dichroism
CHO	chinese hamster ovary cells
CPP	cell-penetrating peptide
DMSO	dimethylsulfoxide
ECP	eosinophilic cationic protein; human ribonuclease 3
DNA	deoxyribonucleic acid
FBS	fetal bovine serum
FPLC	fast performance liquid chromatography
GAG	glycosaminoglycan
GC	Gouy–Chapman
h	hour
HCl	hydrochloric acid
HIV–TAT	residues 47–57 of the HIV-1 trans-activator of transcription
HU	histone-like protein from <i>E. coli</i> strain U93
IC ₅₀	half maximal inhibitory concentration
IMM1–GC	Implicit membrane model supplemented with Gouy–Chapman term

IHF	integration host factor
k_{cat}	first-order equilibrium rate constant
K_{d}	equilibrium dissociation constant
kDa	kilodalton
K_{M}	Michaelis constant
LUV	large unilamellar vesicles
MALDI–TOF	matrix-assisted laser desorption/ionization time-of-flight
MES	2-(<i>N</i> -morpholino)-ethanesulfonic acid
MD	Molecular Dynamics
NaCl	sodium chlorine
ONC	Onconase [®] (a registered trademark of Tamir Biotechnology, Inc.; otherwise, ranpirnase)
PB	Poisson–Boltzmann
PDB	protein data bank
PBS	phosphate–buffered saline
Pyr	pyroglutamate
R-ONC	R-Onconase
RMSD(F)	root mean square difference (fluctuation)
RI	Ribonuclease Inhibitor
RNA	ribonucleic acid
RNase A	bovine pancreatic ribonuclease
RNase 1	human pancreatic ribonuclease

RNase 7	human ribonuclease 7
SDS–PAGE	sodium dodecyl sulfate poly(acrylamide) gel electrophoresis
T_m	temperature at the midpoint of the denaturation curve
Tris	2-amino-2-(hydroxymethyl)-1,3-propanediol
Z	net molecular charge: Arg + Lys – Asp – Glu – Pyr.

CHAPTER 1

Introduction:

Electrostatic Interactions between Proteins and Lipid Bilayers

1.1 Abstract

Pancreatic-type ribonucleases form a conserved class of secreted enzymes that are able to catalyze the degradation of RNA. The known functions of ribonucleases include angiogenesis, bactericidal and helminthic activity, and anti-tumoral activity. The endogenous anti-tumoral activity of Onconase, an amphibian member of the pancreatic-type ribonuclease family, is well documented, but its use has been limited by its ability to access the cytoplasm. Engineered cytotoxic variants of RNase A and RNase 1, mammalian pancreatic ribonucleases, while internalized more efficiently than Onconase, still face a limit to their cytotoxicity due to low internalization efficiency. In order to gain access to the cytoplasm, ribonucleases must be endocytosed by the cell and must cross the endosomal membrane. An important factor for cellular uptake and cytotoxicity has been shown to involve electrostatic interactions. In this chapter, we provide an overview of the cell membrane, an introduction to ribonucleases, and discuss what is known about the electrostatic interaction between the two. We also review methods for computational modeling of electrostatics and the plasma membrane.

1.2 Introduction

The cell membrane is a barrier that separates cellular contents from the external environment.¹ The cell membrane is a complex structure composed of regions with distinct physical properties. It is composed of a phospholipid bilayer with anionic phosphate headgroups sandwiching an interior hydrophobic region formed by lipid alkyl chains.

Interspersed laterally throughout the membrane are lipid rafts, which are cholesterol-rich regions, and proteins, which can serve as signaling species, channels, or enzymes.¹ Cell membranes are asymmetric due to the differing composition of their inner (cytoplasmic) and outer (environmental) leaflets, which is maintained actively. The inner leaflet has a higher concentration of lipids such as phosphatidylserine and phosphatidylethanolamine.² The outer leaflet contains glycosaminoglycans (GAGs), such as heparan sulfate, which are oligosaccharides with carboxyl or sulfuryl groups that form the highly anionic glycocalyx.¹ In cancerous cells, membrane asymmetry is lost, resulting in the outer membrane containing phosphatidylserine and differential expression patterns of heparan sulfate.³

The cell membrane serves as a selectively permeable barrier that small hydrophobic molecules can cross. The cell uses endocytosis to internalize charged and large molecules, including nutrients, proteins, and even cells. Endocytosis is an energy-dependent process in which extracellular contents are internalized when the plasma membrane invaginates to form an endosome.⁴ The contents of the endosome are sorted for trafficking to various cellular compartments or degradation in the lysosome.

There are several types of endocytosis, including phagocytosis, receptor-mediated endocytosis, and pinocytosis. These broad endocytic pathways use overlapping machinery. Large particles, even cells, are internalized with phagocytosis by specialized immune cells.⁵ Receptor-mediated endocytosis, used by all cells, requires a specific ligand–receptor interaction that triggers endocytosis.⁶ Phagocytosis and receptor-mediated endocytosis use clathrin-coated pits. Dynamin is a protein used in receptor-mediated endocytosis and pinocytosis. Pinocytosis is nonspecific, adsorptive endocytosis and is used primarily for the

uptake of fluid and solutes by all cells.⁴ Molecules that bind to GAGs in the glycocalyx, such as heparan sulfate or sialic acid, can be internalized by GAG-mediated endocytosis, which can be either pinocytosis or mediated by a receptor.⁷

Long-range electrostatic interactions are important for membrane association and internalization. Because of the anionic nature of the cell membrane, cationic molecules are attracted to the cell surface.⁸ The importance of electrostatic forces for a particular interaction can be probed by altering the electrostatic nature of the components or by altering solute concentration. If electrostatics perform an important role in binding, increasing or decreasing the amount of charge in a component should affect binding accordingly. Alternatively, because of the screening nature of ions, increasing the salt concentration of a reaction will also decrease the rate of association. For example, DNA and RNA, which are highly anionic, show a strong salt dependence in their interactions with other biological molecules.⁹⁻¹¹ In this thesis, I use both of these methods to study electrostatic forces.

While endocytosis is a useful tool necessary for cell survival, some pathogens and toxins are able to hijack the endocytotic machinery to enter the cell. For example, the hemagglutinin protein on influenza A virus binds to sialic acid in the glycocalyx, triggering endocytosis.¹² The cell-penetrating peptide, nonaarginine, binds to heparan sulfate¹³ and is not only endocytosed: importantly, it can internalize attached cargo.¹⁴ Increasing our understanding of endocytosis is of importance as a basic biological question, but could also provide information on how to both defend against pathogens and deliver pharmacological therapeutics directly to the cytoplasm.

1.3 Pancreatic Ribonucleases

Pancreatic-type ribonucleases form a class of secretory ribonucleases that were among the most-studied enzymes of the 20th century. Secretory ribonucleases are small secreted enzymes composed of approximately 100 amino acids with a characteristic tertiary structure composed of a central four stranded anti-parallel β -sheet flanked by two α -helices.¹⁵ The active site lies in a cleft created by an N-terminal α -helix and a β -sheet. Pancreatic ribonucleases catalyze the cleavage of RNA with varying efficiency ranging from $k_{\text{cat}}/K_M = 310 \text{ M}^{-1}\cdot\text{s}^{-1}$ to $52 \times 10^6 \text{ M}^{-1}\cdot\text{s}^{-1}$.^{16,17} Of the many functions attributed to pancreatic ribonucleases, most depend on their ability to catalyze the degradation of RNA.¹⁸ Although they have a common structure, pancreatic ribonucleases have evolved significantly and demonstrate extensive sequence variance, possibly explaining the wide variety of functions displayed by the family. Described functions of pancreatic ribonucleases include angiogenesis,¹⁹ immunity,²⁰ and cytotoxicity.¹⁵

The cytotoxicity of pancreatic ribonucleases is currently being investigated with applications towards the treatment of cancer.²¹ In order to be cytotoxic, ribonucleases must be endocytosed, escape the endosome, evade a cytoplasmic ribonuclease inhibitor (RI), and retain the ability to degrade RNA.²² Onconase (ONC), an amphibian member of the pancreatic ribonuclease family, was discovered to have innate cytotoxicity towards mammalian cancer cells,²³ which was understood later to be due to its ability to evade RI.²⁴ RI is a ~50 kDa protein present in the cytoplasm at concentrations of ~4 μM .¹⁸ RI binds ribonucleases and inhibits their catalytic activity through steric occlusion of their active site,²⁵ resulting in an abolishment of their biological function. RNase A, bovine pancreatic

ribonuclease, and RNase 1, the human pancreatic ribonuclease, bind RI with femtomolar affinity, resulting in a lack of cytotoxicity.²⁶

Cytotoxic variants of RNase A and RNase 1 have been engineered to evade RI.^{17,26} ONC and a cytotoxic variant of RNase 1²⁷ are currently in clinical trials for cancer.²⁸ Interestingly, cytotoxic variants of RNase A and RNase 1 have similar IC_{50} values to ONC, despite having k_{cat}/K_M values 3 orders of magnitude higher than ONC and demonstrating cellular uptake up to 10-fold higher than ONC.^{17,29,27,30} Understanding the cellular uptake of ribonucleases and the contribution of cell-surface components could provide important information for their chemotherapeutic potential

1.4 Ribonuclease–Cell Surface Interactions

Ribonuclease internalization limits their cytotoxic potential. Injection of ribonucleases directly into the cytoplasm yields toxicity at picomolar levels.³¹ By comparison, cell incubation with ribonucleases results in IC_{50} values in the micromolar range.¹⁵ Ribonuclease–uptake by cells is energy-dependent and occurs via endocytosis.³² ONC, RNase 1, and RNase A exhibit insaturable cellular uptake in HeLa, CHO, and K-562 cells at concentrations up to 10 μ M at 37 °C, which is consistent with non-receptor mediated endocytosis.^{32,29,30} Additionally, ONC is internalized at a rate similar to bulk-rate endocytosis and does not bind to sialic acid or heparan sulfate. Yet, an inhibition of dynamin and AP2, proteins involved in receptor-mediated endocytosis, does result in a decrease in ONC internalization.³³ Additionally, a high-affinity receptor has been reported for ONC on cultured 9L glioma

cells;³⁴ however, this receptor has never been identified. In summary, whereas receptor-mediated endocytosis could play a role in ONC internalization, it appears that the vast majority of ONC internalization occurs by pinocytosis.

An RI-evasive variant of RNase A, D38R/R39D/N67R/G88R (DRNG) RNase A ($Z = +6$), has been shown to bind to sialic acid and heparan sulfate on the cell surface, possibly explaining why it is internalized at a 10-fold higher rate compared to ONC. Although RNase A ($Z = +4$), RNase 1 ($Z = +6$), and ONC ($Z = +5$) all have similar net charges, as mentioned above, they exhibit highly variable cellular uptake.^{35,30} Both the cellular uptake and cytotoxicity of RNase A are strongly determined by electrostatic interactions. A strong positive correlation between net charge and both cellular uptake and cytotoxicity was demonstrated by measuring these properties in variants of RNase A where the carboxyl groups in RNase A were amidated with ethylenediamine (converting the negative charges to positive charges), with 2-aminoethanol (neutralizing the negative charges), or with taurine (maintaining the negative charges).³⁶ Site-directed mutagenesis was used to create an E49R/D53R/G88R RNase A variant that also demonstrated increased cytotoxicity.³⁷ Both of these types of experiments increased the net positive charge of RNase A, but also altered the surface electrostatic distribution.

A neutral RI-evasive variant of RNase 1, R39D/N67D/N88A/G89D/R91D (DDADD) RNase 1, was engineered and found to be mildly cytotoxic.²⁶ DDADD RNase 1 ($Z = 0$) was internalized to a much lower degree as compared to wild-type RNase 1 ($Z = +6$), most likely because of its decreased charge.²⁹ In summary, although the net charge of RNase 1 shows a

positive correlation with internalization, the distribution of surface charge could also drive membrane association, thus making a net positive charge not critical for internalization.

After ribonucleases are internalized, they must translocate across the endosomal membrane in order to access the cytoplasm. After the endosome forms, its interior is quickly acidified and non-specific esterases cleave the glycocalyx from the endosomal membrane, leaving a lipid bilayer with phosphate head groups. At this point, endosomes can fuse with lysosomes, targeting its contents for degradation, or can be targeted for returning to the plasma membrane via the recycling endosomes.

1.5 Pancreatic Ribonuclease-Lipid Bilayer Interaction

Translocation across the endosomal membrane in order to reach the cytoplasm limits cytotoxicity as minimal amounts of ribonuclease are able to cross the endosomal membrane.³⁸ The intracellular trafficking of RNase 1, RNase A, and ONC has been studied *in cellulo*. RNase 1 and RNase A are trafficked to the late endosome or lysosome,^{32,39} while ONC most likely enters the cytoplasm from the recycling endosomes.³³ As endosomes mature, the internal pH becomes more acidic. Neutralizing the pH of endosomes *in cellulo* greatly increases the cytotoxicity of ONC,³³ implying that ONC translocates across the endosomal membrane more efficiently at neutral pH. Though as discussed above, the cellular uptake of ONC does not depend upon its surface charge distribution. Cytotoxicity, however, is affected by changes to surface charge distribution, possibly due to changes in the ability of ONC to translocate across the endosomal membrane.³⁵

Large unilamellar vesicles (LUV; $r \sim 50$ nm) are used as an *in vitro* model for studying protein–lipid bilayer interaction and have provided insight into the interaction between ribonucleases and lipid bilayers. RNase 1 is able to bind to LUVs containing anionic lipids, but it is unable to induce aggregation or fusion of vesicles. RNase A does not bind to LUVs containing anionic lipids.⁴⁰ Eosinophil cationic protein (ECP) ($Z = +14$), which is human RNase 3, interacts with the cell surface of bacteria and helminthes to cause cell death through the disruption of the plasma membrane.⁴¹ ECP can induce aggregation of vesicles followed by disruption of LUV structure, resulting in small pores. In contrast, another human member of the pancreatic ribonuclease family, RNase 7, causes small pores to form in the vesicles before causing aggregation.⁴² Interestingly, while RNase 7 and ECP have similar net charges, they have a very different composition of basic residues. RNase 7 has 18 lysine residues and 4 arginine residues whereas ECP has 18 arginine residues and 1 lysine residue. Lysine and arginine may not have equivalent effects on lipid bilayers, despite having similar charge.

To increase our understanding of potential mechanisms for ribonuclease translocation across lipid bilayers, studying cell-penetrating peptides (CPP), such as penetratin and mellitin, can provide insight. CPP's are ~ 10 – 30 amino acids long, have a high ratio of cationic:anionic/neutral residues, and are also able to internalize attached cargo.⁴³ Mellitin is derived from bee venom and is able to cross a lipid bilayer. The translocation mechanism involves the formation of a toroidal shaped pore in the lipid bilayer, allowing solutes to cross the membrane.⁴⁴ Penetratin forms an amphipathic α -helix that allows insertion into the membrane.^{45,46} Studying the effect of CPPs on membrane structure and stability can also be done with computational modeling.

1.6 Computational Analysis of Protein/Membrane Interactions

While noncovalent molecular forces can be investigated experimentally, computer modeling can be a useful technique as well. Computer modeling can provide mechanistic or structural insight that would be difficult to obtain experimentally. For example, it is fairly straightforward to measure thermodynamic and kinetic parameters for the binding of CPPs to a lipid vesicle.⁴⁷ As mentioned above, from experimental evidence, melittin was believed to form a toroidal pore in lipid bilayers based on the pore's size and irregularity. These pores were hypothesized to have lipid headgroups on their sides to minimize charge repulsion from multiple melittin helices within the pore. Molecular Dynamic (MD) simulations were able to confirm the presence of lipid headgroups on the sides of the pores in addition to matching the experimental pore size.⁴⁸ MD Simulations have also been used to describe the distortion of the lipid bilayer caused by CPPs, as well as the introduction of water into the hydrophobic region due to charged amino acid insertion.⁴⁹ Computer modeling is also useful as a predictive tool for experimental design. De novo proteins have been designed with desired functions by using software and tools that predict protein structure and folding, such as Rosetta⁵⁰ and distributed computing.⁵¹

The major hurdle to modeling biological questions involves the timescale of biological processes and the size of the macromolecules involved in biological questions.⁹ Traditionally, explicit computational modeling includes every atom in the system and calculates the forces and velocities of all atoms at every timestep, usually a femtosecond. Although this approach

works well for small molecules or reactions that occur on the nanosecond timescale, many biological processes occur on a millisecond to minute timescale⁵² and involve thousands of atoms. The computational expense involved is prohibitive for questions involving conformational changes in proteins or the binding of large macromolecules, among others. To avoid this prohibitive time expense, implicit modeling averages the effect of system properties.

Because electrostatics plays a large role in conformational changes in proteins and binding processes, continuum electrostatics are used to implicitly model parts of the system to decrease computational expense.⁵³ For example, solvent electrostatic properties are averaged as a dielectric continuum. When the electrostatic energy of the system is calculated, the electrostatic energies between the solute and explicit solvent molecules are replaced by the electrostatic energy between the solute and the averaged solvent. By replacing explicit water molecules with a continuum to describe the solvent, the computational demands are decreased. Implicit solvents work well at approximating bulk solvent properties; however, explicit water molecules should be included at solvent interfaces or if necessary for conformational stability.⁵⁴

The Poisson–Boltzmann equation has been used to solve the energetics of systems with implicit solvents.⁵⁵ Starting from the Poisson equation,

$$-\nabla^2 V(\vec{r}) = \frac{\rho(\vec{r})}{\epsilon_o} \quad (1.1)$$

where $V(\vec{r})$ is the electrostatic potential, $\rho(\vec{r})$ is the charge distribution, and ϵ_0 is the permittivity of free space, we first account for the presence of an inhomogeneous dielectric, $\epsilon(\vec{r})$. This results in the following equation:

$$-\nabla \cdot \epsilon(\vec{r}) \nabla V(\vec{r}) = \rho(\vec{r}) \quad (1.2)$$

The charge distribution refers to the fixed charges in the system and the ions in the system, which are mobile. The Boltzmann distribution is used to describe the ion distribution. The number density for positive and negative ions is given by:

$$n_{\pm} = n_{\infty} \exp(-U_{\pm} / k_B T) \quad (1.3)$$

where n_{∞} is the bulk ion concentration, k_B is Boltzmann's constant, T is the temperature, and U_{\pm} is the free energy for the position of the ion. Substituting the ion distribution into the Poisson equation and assuming a 1:1 electrolyte and fixed charge distribution $\rho_f(\vec{r})$ results in:

$$-\nabla \cdot \epsilon(\vec{r}) \nabla V(\vec{r}) = \rho_f(\vec{r}) + qn_{+} - qn_{-} \quad (1.4)$$

If one assumes that the free energy of the potential mean force of the ion is its charge times the potential, then equation 1.4 leads to the Poisson-Boltzmann equation:

$$-\nabla \cdot \epsilon(\vec{r}) \nabla V(\vec{r}) = \rho_f(\vec{r}) - 2qn_{\infty} \sinh(qV(\vec{r})/k_B T) \quad (1.5)$$

The Poisson–Boltzmann equation is a nonlinear differential equation and can only be solved numerically. In summary, the assumptions of the model are that the ions are treated as point charges that do not interact with the polarization on other induced charges.⁵⁵ The charges are treated additively in a Coulombic treatment.

Lipid bilayers are an active area of implicit model development. The heterogeneous nature of the bilayer complicates model development. While aqueous bulk solvent can be assumed to be homogeneous and modeled with a dielectric of ~ 80 because the extensive hydrogen bonding network in water results in high levels of charge shielding and excellent solvation of charged species. In contrast, any implicit membrane model must account for the presence of the hydrophobic interior and the hydrophilic region. The hydrophilic region of a lipid bilayer has a high density of charge due to the presence of phosphate head groups and the sulfate and sugar groups on the glycocalyx, and therefore has a dielectric similar to that of water.⁵⁶ This region can be modeled as negative charges of a determined density, as dipoles, or with a term derived from the Gouy–Chapman theory for an electrostatic double layer. The hydrophobic interior, on the other hand, is composed of the carbon alkyl chains of lipids and cholesterol and can be modeled as an organic solvent region. An organic solvent, such as cyclohexane, has a dielectric of ~ 2 and provides negligible solvation for charged species.⁵⁶ One drawback of modeling membranes implicitly includes the inability to capture protein-induced lipid clustering.

Computational studies of proteins with implicit membranes have been used for several purposes. Poisson–Boltzmann calculations using an implicit membrane with the hydrophilic

region modeled as a anionic spheres were used to determine the most energetically favorable protein–membrane orientation for cytochrome *c*.⁵⁷ Recently, an elasticity model was incorporated into an implicit membrane with dipole charges to account for membrane deformation in studies on the favorability of amino acid insertion into the hydrophobic region. Using continuum electrostatics combined with an elasticity model, workers were able to recreate insertion energies of amino acids to within an average 1.3 kcal/mol from explicit MD simulations.⁵⁸

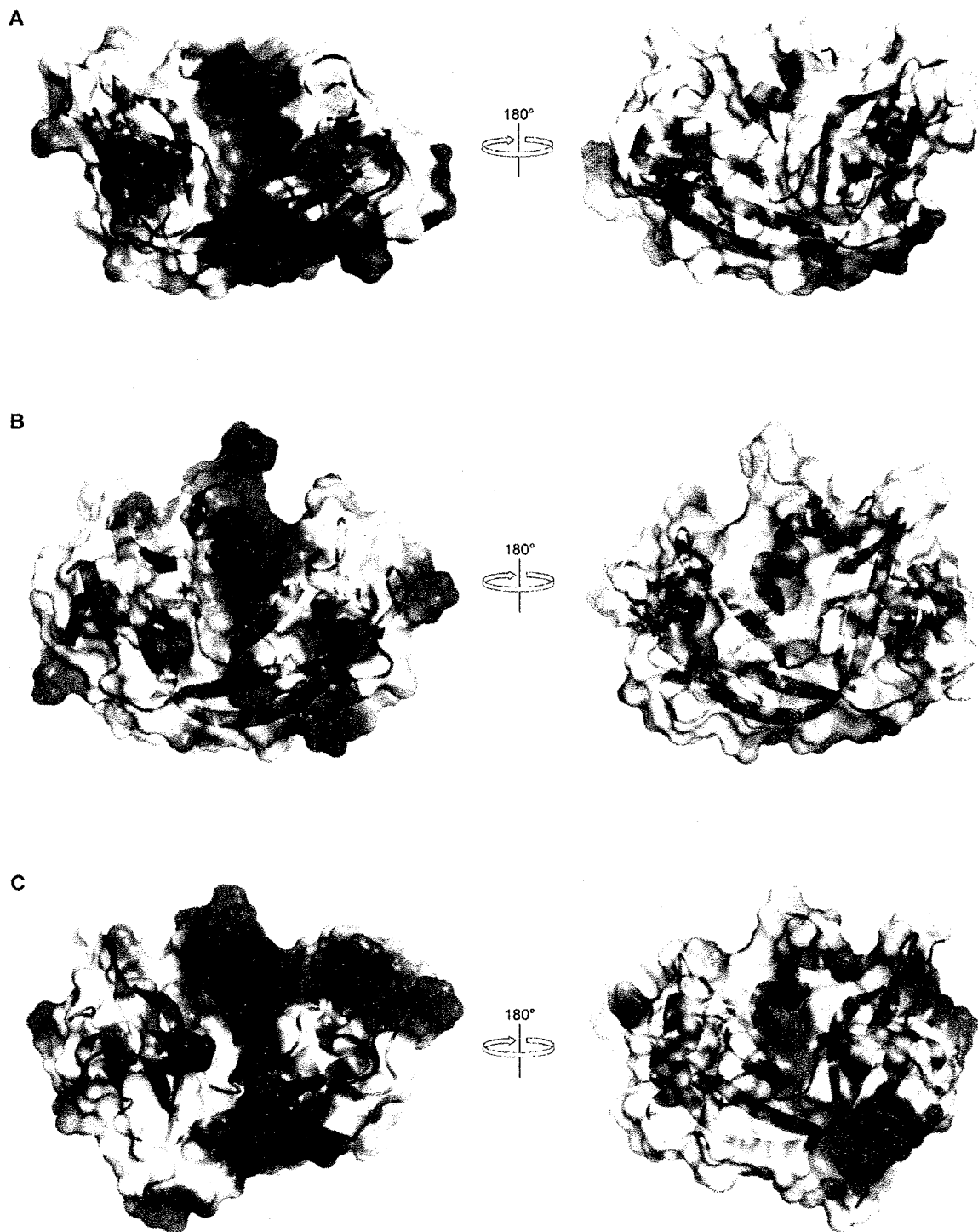
The binding of CPPs with an implicit membrane incorporating a Gouy–Chapman electrostatic term accurately captured the energetics and behavior of CPPs in implicit MD simulations. Additionally, the MD simulations provided insight into the penetration of hydrophobic residues into the hydrophobic lipid core. In simulations of penetratin, which forms an amphipathic helix in membranes, the final snapshot showed insertion of approximately one-third of the helix after 1 ns.⁵⁹

This thesis investigates the role of electrostatic interactions in macromolecular association and behavior. In Chapter 2, the effect of lysine and arginine residues on the cellular uptake and biochemical properties of Onconase is studied by using a variety of experimental methods. In Chapter 3, the contribution of electrostatics to the binding of ONC, RNase A, and RNase 1 to model membranes is studied by using both experimental and computational techniques. In Chapter 4, explicit MD simulations are used to study the effect of salt concentration on salt bridge formation in IHF, a DNA wrapping protein. Chapter 5 directs the reader to future directions of the work. Together, the work extends extant knowledge of

ribonuclease internalization and provokes new ideas for designing cytotoxic variants of ribonucleases.

Figure 1.1 Structures of pancreatic-type ribonucleases.

Cartoon models of ONC (A), RNase A (B), and RNase 1 (C) are superimposed with electrostatic potential maps using PyMOL (PDB entries 1ONC, 7RSA, and 1Z7X, respectively). Areas with positive electrostatic potential are blue and areas with negative electrostatic potential are red.



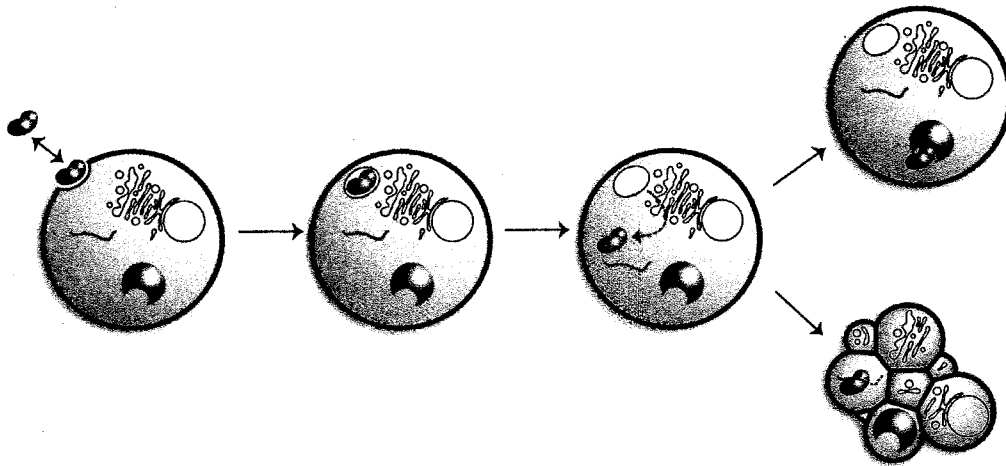


Figure 1.2 Cytotoxic pathway of pancreatic-type ribonucleases

Pancreatic-type ribonucleases (depicted as the blue kidney-shaped object) bind to the cell surface and undergo endocytosis. The ribonuclease must then escape from the endosomal organelles into the cytosol. Ribonuclease inhibitor (the red pacman-shaped object) can prevent ribonuclease-mediated cytotoxicity provided the ribonuclease is unable to evade it. Onconase is able to evade RI, however, RNase A and RNase 1 bind to RI with femtomolar affinity.

CHAPTER 2

Arginine Residues are More Effective than Lysine Residues in Eliciting the Cellular Uptake of Onconase

Contribution:

This chapter was submitted as:

Sundlass, N. K., Raines, R. T. (2011) Arginine Residues are More Effective than Lysine Residues in Eliciting the Cellular Uptake of Onconase.

2.1 Abstract

Onconase is an amphibian member of the pancreatic ribonuclease family of enzymes and is in clinical trials for the treatment of cancer. Onconase, which has an abundance of lysine residues, is internalized by cancer cells through endocytosis in a mechanism similar to that of cell-penetrating peptides. Here, we compare the effect of lysine versus arginine residues on the biochemical attributes necessary for Onconase to elicit its cytotoxic activity. In the variant R-Onconase, ten of the twelve lysine residues in Onconase are replaced with arginine, leaving only the two active-site lysines intact. Cytometric assays quantifying internalization showed a 3-fold increase in the internalization of R-Onconase compared with Onconase. R-Onconase also showed a 2-fold increase in ribonucleolytic activity. Nonetheless, arginine substitution endowed only a slight increase in toxicity towards human cancer cells. Analysis of denaturation induced with guanidine-HCl showed that R-Onconase has less conformational stability than does the wild-type enzyme; moreover, R-Onconase is more susceptible to proteolytic degradation. These data indicate that arginine residues are more effective than lysine in eliciting cellular internalization, but can compromise other aspects of protein structure and function.

2.2 Introduction

Delivering an exogenous protein to the cytosol is a challenge. Although some proteins can enter cells by receptor-mediated endocytosis, most do not have cell-surface receptors. Here,

we investigate a key biochemical feature of a protein that lacks a cell-surface receptor but has an intrinsic ability to gain entry to the cytosol of human cells.

Pancreatic-type ribonucleases readily undergo endocytosis and can exhibit specific toxicity towards cancerous cells by degrading cellular RNA. Their binding to the cell surface is not saturable,³² and is mediated by nonspecific Coulombic interactions.²⁹ Onconase (ONC) is an 11.8-kDa pancreatic-type ribonuclease discovered originally in the oocytes of the *Rana pipiens* frog. ONC possesses endogenous anti-tumoral activity and has been granted fast-track and orphan-drug status for the treatment of malignant mesothelioma.^{60,21,22,61,62} Although ONC contains endogenous cytotoxicity, its rate of internalization seems to limit its effectiveness, as the cellular uptake of ONC is only slightly faster than fluid-phase uptake.⁶³ Moreover, the clinical utility of ONC has been limited by its rapid accumulation in the kidneys,^{64,65} resulting in dose-limiting renal toxicity.²⁸ While two saturable binding sites with K_D of 0.062 and 0.25 μM were reported to exist for 9L glioma cells,³⁴ binding to HeLa cells and CHO cells was later shown to be unsaturable at concentrations up to 10 μM , indicative of nonspecific binding.^{32,30}

Natural cell-penetrating peptides, such as HIV-TAT or penetratin, have a preponderance of cationic residues and are endocytosed readily.^{66,67} Interestingly, lysine and arginine residues affect the internalization of such peptides to differing degrees. For example, replacing all of the cationic residues in penetratin with either lysine or arginine revealed a ten-fold advantage for the all-arginine variant compared with the all-lysine variant.⁶⁸ This trend is also apparent with synthetic cell-penetrating peptides, as nonaarginine is internalized more readily and is more disruptive to synthetic lipid bilayers than is nonalysine.⁶⁹ Arginine forms

more stable hydrogen bonds with phosphoryl groups at physiological temperature,⁷⁰ and could also form a stable interaction with the carboxyl, phosphoryl, and sulfuryl groups on the cell surface, thus triggering endocytosis.¹³

Increasing the net positive charge (Z) of a protein by either chemical modification or site-directed mutagenesis can increase its internalization.^{36,71,72} For example, green fluorescent protein (GFP) is a highly anionic protein ($Z = -9$) that is not taken up by cells. Replacing five acidic residues with arginine on one face of the folded protein endowed GFP with the ability to undergo endocytosis.⁷³ Installing even more cationic residues generated a variant ($Z = +36$) that not only undergoes endocytosis, but also internalizes pendant cargo.⁷⁴ Likewise, installing arginine residues in two homologues, bovine pancreatic ribonuclease (RNase A) and the bullfrog sialic acid-binding lectin, increases their internalization.^{75,37} Cytotoxicity has been linked to the net positive charge of a protein,²⁹ as well as the distribution of that charge.⁷⁶ None of these studies, however, examined whether lysine and arginine residues have a differential effect on the cellular internalization of a protein and its subsequent function.

ONC is a highly cationic protein. Among its 104 residues, twelve are lysine and three are arginine (Figure 2.1),⁷⁷ leading to $Z = +5$ and $pI > 9$.⁷⁸ Herein, we report on the consequences of replacing the ten non-active-site lysine residues of ONC with arginine. We find that the increased arginine content has significant effects on cellular uptake as well as on important biochemical attributes of ONC.

2.3 Methods

2.3.1 Materials

K-562 cells were derived from a continuous human chronic myelogenous leukemia cell line and obtained from American Type Culture Collection (Manassas, VA). *Escherichia coli* strain BL21(DE3) cells and plasmid pET22b(+) were from Novagen (Madison, WI).

Restriction enzymes were from New England Biolabs (Ipswich, MA), and other enzymes were from Promega (Madison, WI). 6-Carboxyfluorescein-dArUdGdA-6-carboxytetramethylrhodamine (6-FAM-dArUdGdA-6-TAMRA) was obtained from Integrated DNA Technologies (Coralville, IA). Cell culture medium and supplements were from Invitrogen (Carlsbad, CA). [*methyl*-³H]Thymidine (6.7 Ci/mmol) was from Perkin-Elmer (Boston, MA). Mes was from Sigma-Aldrich (St. Louis, MO); Mes buffers were purified by anion-exchange chromatography to remove oligo(vinylsulfonic acid), which is a potent inhibitor of ribonucleases that contaminates commercial chemicals derived from ethanesulfonic acid.⁷⁹ All other chemicals used were of commercial grade or better, and were used without further purification.

2.3.2 Analytical Instruments

Molecular mass was measured by MALDI-TOF mass spectrometry using a Voyager-DE-PRO Biospectrometry Workstation (Applied Biosystems, Foster City, CA). Fluorescence was quantified with an Infinite M1000 plate reader (Tecan, Männedorf, Switzerland). CD

experiments were performed with a model 62A DS CD spectrophotometer equipped with a temperature controller (Aviv, Lakewood, NJ) at the University of Wisconsin–Madison Biophysics Instrumentation Facility. Radioactivity was quantified by scintillation counting using a Microbeta TriLux liquid scintillation counter (Perkin–Elmer, Wellesley, MA). Flow cytometry data were collected in the University of Wisconsin Paul P. Carbone Comprehensive Cancer Center with a FACSCalibur flow cytometer equipped with a 488 nm argon-ion laser (Becton Dickinson, Franklin Lakes, NJ).

2.3.3 *Production of Ribonucleases*

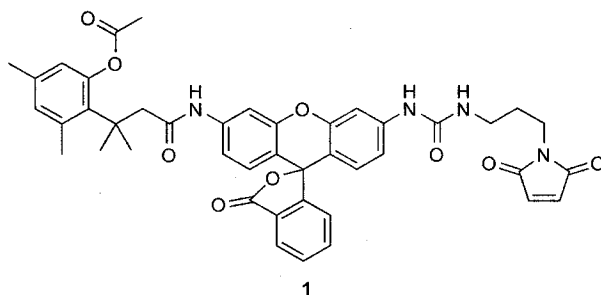
Synthetic DNA encoding a pelB leader sequence followed by R-ONC, in which all lysine residues had been converted to arginine with the exception of the active-site lysines, Lys9 and Lys31, was from GENEART (Burlington, Ontario, Canada). This gene was inserted into plasmid pET(22b)+ using *Nde*I and *Sal*I restriction enzymes. R-ONC was purified from inclusion bodies as described previously¹⁵ with the following exceptions. R-ONC was folded at 4 °C for five days following a slow, ten-fold dilution into 0.10 M Tris–HCl buffer at pH 7.8 containing L-arginine (0.5 M), reduced glutathione (3.0 mM), and oxidized glutathione (0.6 mM). Following concentration by ultrafiltration, R-ONC was purified by FPLC using a Superdex G-75 gel-filtration column (GE Healthcare, Piscataway, NJ) in 50 mM sodium acetate buffer at pH 5.0 containing NaCl (0.10 M) and NaN₃ (0.02% w/v). Further purification by FPLC using a 5 mL HiTrap SPHP column and a linear gradient of NaCl (0.15–0.45 M) in 50 mM sodium acetate buffer at pH 5.0. Protein concentration was

determined using ultraviolet spectroscopy using extinction coefficients of $\epsilon_{280} = 0.87$ ($\text{mg} \cdot \text{mL}^{-1})^{-1} \cdot \text{cm}^{-1}$ for both ONC and R-ONC.

2.3.4 *Production of Labeled Ribonucleases*

The purification of R-ONC was complicated by incomplete cleavage of the pelB leader sequence. Accordingly, site-directed mutagenesis was used to replace the pelB leader sequence with a methionine residue to create Met(–1)R-ONC. In addition, Ser61 was replaced with a cysteine residue to create S61C ONC⁷⁶ and S61C Met(–1) ONC, which are poised for *S*-alkylation. Following gel-filtration chromatography, the sulfhydryl groups of S61C Met(–1)R-ONC and S61C ONC were protected by reaction with 5,5'-dithio-bis(2-nitrobenzoic acid), and the resulting proteins were dialyzed overnight against 50 mM sodium acetate buffer at pH 5.0. Protected S61C ONC and S61C Met(–1)R-ONC were purified by FLPC using a 5-mL HiTrap SPHP column and a linear gradient of NaCl (0.15–0.45 M) in 50 mM sodium acetate buffer at pH 5.0. To remove the methionine at its N-terminus, S61C Met(–1)R-ONC was incubated with aminopeptidase for 24 h at 37 °C in PBS at pH 8.0.

S61C variants protected as a mixed disulfide with 2-nitro-5-thiobenzoic acid were deprotected with a 5-fold molar excess of dithiothreitol, then desalted by using a PD-10 desalting column (GE Biosciences, Piscataway, NJ). Deprotected proteins in PBS were reacted for 4–6 h at 25 °C with a 10-fold molar excess of fluorogenic label **1**,⁸⁰ which was a generous gift from



L. D. Lavis (Janelia Farm Research Campus, Howard Hughes Medical Institute). The reaction was quenched by rapid dilution into 50 mM sodium acetate buffer at pH 5.0. Conjugates were purified by FPLC using a 5-mL HiTrap SPHP column, and the concentration of conjugates were determined with a bicinchoninic acid assay kit (Thermo Fisher Scientific, Rockford, IL) and bovine serum albumin as a standard.

2.3.5 Assays of Catalytic Activity

The ribonucleolytic activity of ONC and its variants was measured by monitoring cleavage of a hypersensitive fluorogenic substrate, 6-FAM–dArUdGdA–6-TAMRA, as described previously.⁸¹ Fluorescence emission at 515 nm, following excitation at 492 nm, in the presence of enzyme was measured in 0.10 M Mes–NaOH buffer at pH 6.0 containing 0.10 M NaCl, 6-FAM–dArUdGdA–6-TAMRA (50 nM), and human ribonuclease inhibitor (0.1 nM) at 25 °C. Values for $k_{\text{cat}}/K_{\text{M}}$ were calculated with the equation:

$$k_{\text{cat}}/K_{\text{M}} = \left(\frac{\Delta F / \Delta t}{F_{\text{max}} - F_0} \right) \frac{1}{[\text{E}]} \quad (2.1)$$

In equation 2.1, $\Delta F/\Delta t$ is the initial slope of the reaction, F_0 is the initial fluorescence intensity, F_{\max} is the fluorescence intensity once the reaction is brought to completion, and $[E]$ is the concentration of the enzyme.

2.3.6 Cytotoxicity Assays

The effect of ONC and R-ONC on the proliferation of K-562 cells was assayed as described previously.¹⁵ K-562 cells were incubated for 44 h with ribonuclease before treatment with [*methyl*-³H]thymidine for 4 h, at which time the incorporation of radioactive thymidine into cellular DNA was quantitated by liquid scintillation counting. The results are shown as the percentage of [*methyl*-³H]thymidine incorporated relative to untreated cells. Values for IC₅₀ were calculated by fitting the curves by nonlinear regression to the equation:

$$y = \frac{100\%}{1 + 10^{(\log(IC_{50}) - \log[ribonuclease])h}} \quad (2.2)$$

where y is the total DNA synthesis following the [*methyl*-³H]thymidine pulse, and h is the slope of the curve.

2.3.7 Flow Cytometry Assays

The internalization of fluorogenic ONC and R-ONC into K-562 cells was determined by monitoring the deprotection of the fluorophore after encountering intracellular esterases.⁷⁶ K-562 cells from near confluent flasks were collected by centrifugation and resuspended at a

density of 1×10^6 cells/mL in fresh RPMI 1640 containing FBS (10% v/v). Labeled or unlabeled ribonuclease (10 μ M) were incubated with K-562 cells for 3 h at 37 °C. To quench internalization, K-562 cells were collected by centrifugation at 1000 rpm for 5 min at 4 °C, washed once with ice-cold PBS, and resuspended in 300 μ L of PBS. Samples remained on ice until analyzed by flow cytometry.

Fluorescence was detected through a 530/30 nm band-pass filter. Cell viability was determined by staining with propidium iodide, which was detected through a 660 nm long-pass filter. The mean channel fluorescence intensity of 10^4 viable cells was determined for each sample with CellQuest software and used for subsequent analysis.

2.3.8 Heparin-affinity Chromatography

The affinity of ONC and R-ONC for heparin was measured *in vitro*. Each ribonuclease was dissolved in PBS at pH 7.0 and loaded onto a 1.0 mL HiTrap Heparin HP column (GE Healthcare, Piscataway, NJ). The column was washed with PBS and ribonucleases were eluted with a gradient of NaCl (0.00–0.45 M) in PBS. Columns were run sequentially, not simultaneously. Protein elution was monitored by absorbance at 280 nm.

2.3.9 Guanidine-HCl Induced Transition Curves

The guanidine-HCl-induced unfolding of ONC and R-ONC were monitored by fluorescence spectroscopy. Assays were performed in 100 mM sodium acetate buffer at pH 5.5 containing protein (25 μ g/mL) and guanidine-HCl (0–6.8 M). After equilibration, five

fluorescence spectra were recorded from 310–380 nm. The bandwidth was 5 nm for excitation at 295 nm and 10 nm for emission. From these spectra, the shift of the wavelength of maximal emission (y) as a concentration of guanidine–HCl was determined and evaluated by nonlinear regression with the program GraphPad Prism 5.0 and the equation.⁸²

$$y = \frac{y_N^0 + m_N[D] + (y_D^0 + m_D[D]) \exp(-m_{\Delta G}([D]_{50\%} - [D])/RT)}{1 + \exp(-m_{\Delta G}([D]_{50\%} - [D])/RT)} \quad (2.3)$$

where $[D]_{50\%}$ is the concentration of denaturant $[D]$ at which 50% of the protein is denatured, $m_{\Delta G}$ is the measure of the dependence of the standard free energy on denaturant concentration, y_N^0 and y_D^0 are the intercepts and m_N and m_D the slopes in the pre- and post-transition region, respectively, in the y versus $[D]$ graph. The fraction of protein in the folded state (f_N) was determined with the equation:

$$f_N = (y_D - y)/(y_D - y_N) \quad (2.4)$$

with

$$y_D = y_D^0 + m_D[D] \quad (2.5)$$

and

$$y_N = y_N^0 + m_N[D] \quad (2.6)$$

where y_N and y_D are the signals of the native and denatured protein as a function of denaturant concentration. Values of the standard free energy were calculated with the equation:

$$\Delta G^{[D]} = \Delta G^{H_2O} - m_{\Delta G}[D] \quad (2.7)$$

where ΔG^{H_2O} is the standard free energy of unfolding in the absence of denaturant.

2.3.10 Protease Susceptibility

ONC and R-ONC (0.2 mg/mL) were treated with pepsin at a w/w ratio of 1:2 pepsin/ribonuclease in 50 mM glycine-HCl buffer at pH 2.4 and 37 °C. Aliquots were removed at known times and 2 M Tris was added to raise the pH to 8.0. Samples were analyzed by SDS-PAGE, and bands stained with Coomassie Brilliant Blue R-250⁸³ were analyzed by densitometry using ImageJ software.

2.4 Result

2.4.1 Design, Production, and Purification of R-Onconase

ONC contains three arginine and twelve lysine residues, two of which, Lys9 and Lys31, are necessary for catalytic activity.⁸¹ In the R-ONC variant, all lysines with the exception of

Lys9 and Lys31 were replaced with arginine. Thus, R-ONC contains 2 lysine and 13 arginine residues.

R-ONC was produced in *E. coli* and purified from inclusion bodies. SDS-PAGE and mass spectrometry revealed two distinct protein populations, consistent with the pelB leader sequence not being cleaved from a significant fraction of R-ONC. The N-terminal residue of wild-type ONC is a glutamine, which cyclizes spontaneously to form a pyroglutamate that is critical for catalytic activity.⁸¹ That cyclization requires an N-terminal amino group, and thus cannot occur when the pendant pelB leader sequence is intact. R-ONC was separated from pelB-R-ONC by using an extended gradient during cation-exchange chromatography. This procedure resulted in pure R-ONC (~1 mg/L of culture) as assessed by SDS-PAGE and mass spectrometry (m/z 12,111; expected: 12,100).

2.4.2 Production and Purification of Labeled R-ONC

The conventional production of S61C R-ONC failed because the pelB leader sequence was not cleaved from the protein and because the uncleaved variant was insoluble. Accordingly, site-directed mutagenesis was used to replace the pelB leader sequence with a methionine residue. S61C Met(-1)R-ONC was produced, folded, and purified successfully (m/z 12,322; expected: 12,311). Aminopeptidase catalyzed the hydrolysis of the Met(-1)-Gln1 peptide bond, enabling Gln1 to cyclize into a pyroglutamate residue (m/z 12,147; expected: 12,134). The integrity of labeled R-ONC was confirmed by MALDI-TOF mass spectrometry (m/z 12,894; expected: 12,873).

2.4.3 Catalytic Activity

The enzymatic activity of a ribonuclease is essential for its cytotoxic activity.^{84,17,85} We found the ribonucleolytic activity of R-ONC ($k_{\text{cat}}/K_{\text{M}} = 88 \pm 17 \times 10^3 \text{ M}^{-1}\cdot\text{s}^{-1}$) to be 2-fold greater than that of ONC ($k_{\text{cat}}/K_{\text{M}} = 39 \pm 9 \times 10^3 \text{ M}^{-1}\cdot\text{s}^{-1}$).

2.4.4 Cellular Internalization

A ribonuclease must enter the cell to exert its cytotoxic activity. We have shown previously that intracellular esterases unmask fluorogenic label **1** within an endosome, enabling quantification using flow cytometry.^{80,30} As shown in Figure 2.2, R-ONC exhibited a 3-fold increase in cellular uptake compared to ONC.

2.4.5 Heparin-affinity

Heparan sulfate is known to be important for the internalization of arginine-rich peptides and some pancreatic-type ribonucleases. We assessed the relative affinity of R-ONC and ONC for heparin and found that R-ONC has greater affinity for heparin than does ONC (Figure 2.3). Because of the prevalence of heparan in the glycocalyx, this could explain the increased internalization of R-ONC as seen in Figure 2.2.

2.4.6 Cytotoxic Activity

Because of its enhanced ribonucleolytic activity and cellular uptake, R-ONC could be more cytotoxic than ONC. We found, however, that ONC has $\text{IC}_{50} = 0.4 \pm 0.1 \text{ }\mu\text{M}$ and R-

ONC has $IC_{50} = 0.29 \pm 0.01 \mu\text{M}$ (Figure 2.4), indicative of only a marginal increase in cytotoxicity that is not statistically significant.

2.4.7 Conformational Stability

Next, we sought a biochemical basis for the unexpectedly low cytotoxic activity of R-ONC. Guanidine-HCl induces the denaturation of proteins,⁸⁶ and we used that attribute to discern the effect of arginine substitution on conformational stability. We found that ONC has $\Delta G^{\text{H}_2\text{O}} = 55 \pm 7 \text{ kJ/mol}$ and $[D]_{50\%} = 4.44 \pm 0.03 \text{ M}$, whereas R-ONC has $\Delta G^{\text{H}_2\text{O}} = 46 \pm 9 \text{ kJ/mol}$ and $[D]_{50\%} = 4.06 \pm 0.06 \text{ M}$ (Figure 2.5). These data indicate that arginine substitution destabilizes ONC although not significantly.

2.4.8 Protease Susceptibility

Finally, we determined whether the decrease in conformational stability of R-ONC might affect its integrity *in cellulo*. To discern the susceptibility of ONC and R-ONC to degradation by proteases, we incubated the protein with pepsin. ONC was resistant to degradation by pepsin over the entire timecourse of the incubation, remaining 90% intact after 22 h (Figure 2.6). By contrast, R-ONC was highly susceptible to degradation—only ~25% remained intact after 22 h.

2.5 Discussion

ONC is a member of the pancreatic ribonuclease family with innate anti-tumoral activity.^{60,21,22,61,62} Because it lacks a cell-surface receptor and elicits a distinctive phenotype—cell death—ONC is an ideal model for assessing biochemical attributes that promote the cellular uptake of proteins. Here, we show that arginine substitution leads to an increase in the cellular uptake of ONC.

The cell surface is highly anionic, containing phospholipids, glycosaminoglycans, and heparan sulfate. Though similar in net charge, cell-penetrating peptides with many arginine residues display more efficient cellular uptake than do their lysine counterparts. The guanidinium group of arginine has a higher pK_a than does the ammonium group of lysine, and is able to form an additional hydrogen bond with the prevalent sulfuryl and phosphoryl groups on the cellular surface. Moreover, arginine is accommodated near the middle of a lipid bilayer with less energetic cost than lysine,⁸⁷ and arginine unlike lysine can be charged or uncharged there due to the induction of large water defects in a host membrane.⁴⁹

R-ONC contains 13 arginine and 2 lysine residues. Here, heparin-affinity chromatography demonstrated that arginine substitution confers the ability for ONC to bind to heparin, which could trigger GAG-mediated endocytosis. The increase in cellular uptake of R-ONC, though significant, is ~10-fold lower than the levels of cellular uptake of human pancreatic ribonuclease (RNase 1), which has 10 arginine and 8 lysine residues, or of RNase A, which has 10 lysine and 4 arginine residues.^{29,76} The distribution of cationic residues could explain the discrepancy in cellular internalization. For example, the cationic residues in RNase 1 and

RNase A are clustered in the active-site cleft, whereas those in ONC are distributed across the protein surface.

ONC is an exceptionally stable protein with $T_m > 90\text{ }^\circ\text{C}$.^{88,81,82} Single amino-acid substitutions in ONC, such as F28T, can result in a decrease in conformational stability of $>20\text{ kJ/mol}$.⁸² The E49R and D53R substitutions in RNase A, which enhance cellular uptake, decrease the value of T_m by $10\text{ }^\circ\text{C}$.³⁷ Yet, we find that replacing 10% of the residues in ONC diminishes conformational stability by $<10\text{ kJ/mol}$, an amount that is not statistically significant. The small observed decrease in conformational stability is surprising in light of the difficulty that we experienced in folding R-ONC *in vitro* (*vide supra*). Moreover, we were unable to determine a T_m value for R-ONC because of its irreversible denaturation and its precipitation when unfolded (data not shown), in contrast to the behavior of wild-type ONC or other variants.^{81,76} We note that another member of the pancreatic ribonuclease family, eosinophil cationic protein, also contains more arginine than lysine residues and also unfolds irreversibly *in vitro*.⁸⁹

R-ONC showed a small decrease in conformational stability and a large increase in protease susceptibility. Protease resistance is an important determinant of cytotoxicity.^{88,90} Several workers have hypothesized that the resistance of ONC to proteolysis is due to its structural rigidity.^{91,82} Di Donato and coworkers found that the M23L substitution, which disrupts the hydrophobic packing of ONC, has effects on protease susceptibility, catalytic activity, and thermodynamic stability comparable to those in R-ONC.⁸⁸ The M23L substitution increases the mobility of the 24–31 loop, which increases its vulnerability to proteases but enables Lys31 to extend further into the active site. An increase in the mobility

of the 24–31 loop due to the K33R substitution could explain the increase in catalytic activity, but is unlikely to have resulted in all of the changes observed herein. The multiple arginine residues in R-ONC could increase the access of a protease to peptide bonds because interactions of the main chain with the side chain of arginine are more likely to be disruptive than are those with the side chain of lysine.⁷⁰

Because the internalization of R-ONC was three-fold greater than that of ONC (Figure 2.2), we expected R-ONC to display a comparable increase in cytotoxicity. Surprisingly, R-ONC remained as cytotoxic as ONC (Figure 2.4). Proteolytic degradation assays showed that the amount of intact R-ONC at 4 h is less than that of intact ONC at 22 h (Figure 2.6). R-ONC may also be trafficked within the cell differently because of its ability to bind to heparin (Figure 2.3), resulting in GAG-mediated endocytosis. Apparently, R-ONC maintains its cytotoxicity through its greater cellular internalization and higher catalytic activity.

Understanding the tumoral targeting and dose-limiting renal toxicity of ONC is important for the development of more effective chemotherapeutic agents based on pancreatic-type ribonucleases. The renal toxicity of ONC can be attributed to its accumulation in the kidneys, combined with its low protease susceptibility. R-ONC maintains high cytotoxicity but could exhibit less renal toxicity because of its increased protease susceptibility. Relevant studies on the consequences of this interdependence are on going in our laboratory.

Acknowledgements. We are grateful to L. D. Lavis for providing fluorogenic label **1**, and U. Arnold, C. H. Eller, G. A. Ellis, L. M. Maurer, and J. E. Lomax for contributive discussions and critical reading of the manuscript. This work was supported by Grant R01

CA073808 (NIH). N.K.S. was supported by Molecular Biophysics Training Grant T32 GM008293 (NIH).

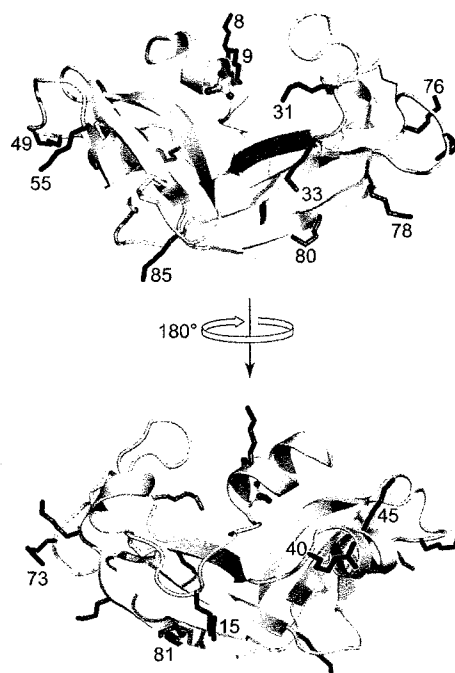


Figure 2.1 Three-dimensional structure of Onconase (PDB entry code 1ONC).⁷⁷ Native arginine side-chains are in black; lysine side chains replaced with arginine in R-ONC are in blue; Lys9 and Lys31 are in magenta and are essential for catalytic activity.

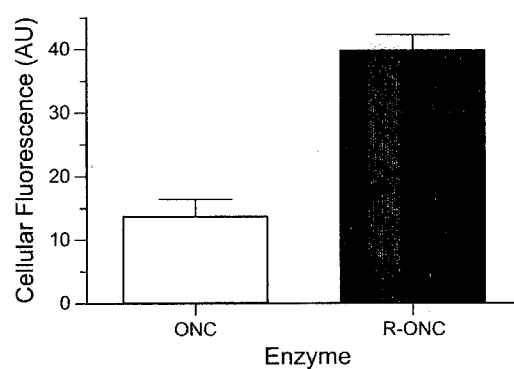


Figure 2.2 Effect of arginine residues on the cellular uptake of Onconase. Ribonucleases were conjugated via Cys61 to latent fluorophores containing fluorogenic label 1. Flow cytometry was used to measure the internalization of ONC and R-ONC into K-562 cells. R-ONC displayed increased internalization compared to ONC ($p < 0.01$).

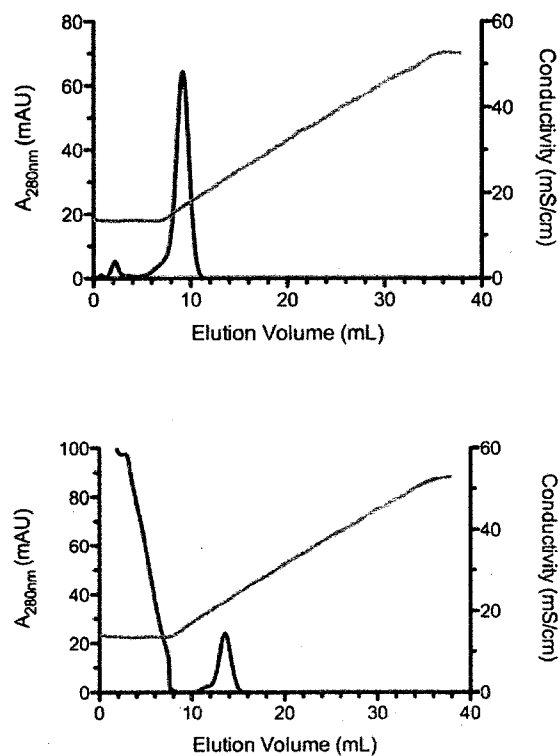


Figure 2.3 Elution profiles of ONC (A) and R-ONC (B) from immobilized heparin

Ribonucleases were detected by their absorbance at 280 nm (black line) during elution with a linear gradient of NaCl in PBS. Conductivity (gray line): PBS, 14 mS/cm; ONC elution, 16 mS/cm; R-ONC elution, 23 mS/cm.

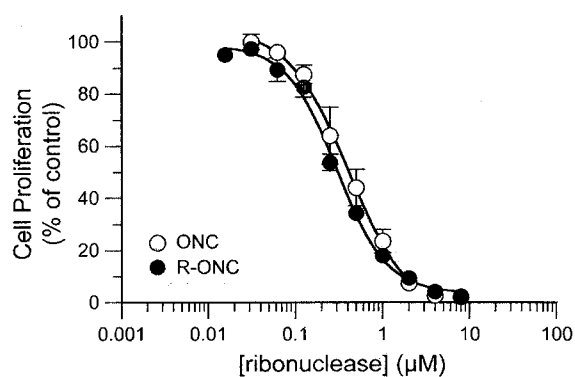


Figure 2.4 Effect of arginine residues on the cytotoxicity of Onconase. Cellular proliferation was assessed by measuring the incorporation of [*methyl*-³H]thymidine into DNA of K-562 cells in the presence of ribonucleases. IC₅₀ values: ONC, 0.4 ± 0.1 μM; R-ONC, 0.29 ± 0.01 μM.

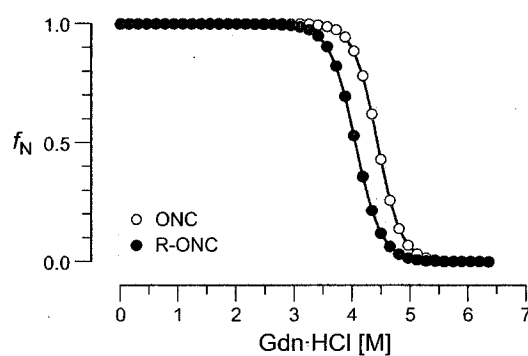


Figure 2.5 Effect of arginine residues on the conformational stability of Onconase. The guanidine-HCl transition curves of ONC and R-ONC were determined by using fluorescence spectroscopy. f_N refers to the fraction of protein in the native state. $[D]_{50\%}$ values: ONC, 4.44 ± 0.03 M; R-ONC, 4.06 ± 0.06 M.

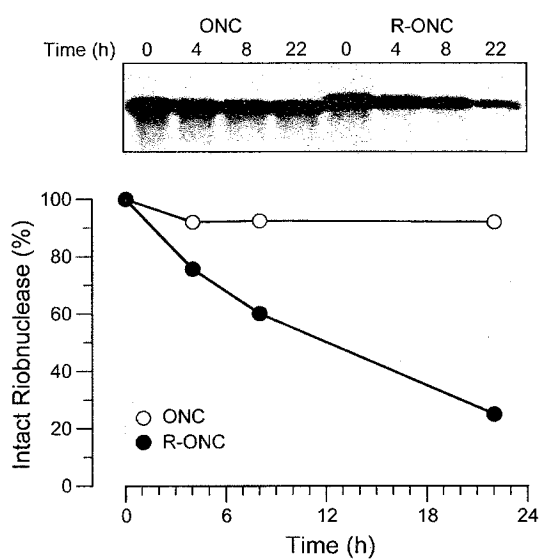


Figure 2.6 Effect of arginine residues on the protease susceptibility of Onconase. ONC and R-ONC were incubated with pepsin in 50 mM glycine-HCl buffer at pH 2.4 and 37 °C. Aliquots were removed at 0, 4, 8, and 22 h. Samples were analyzed with SDS-PAGE, and stained bands were analyzed by densitometry.

CHAPTER 3

Contribution of Electrostatics to the Binding of Pancreatic Ribonucleases to Membrane

3.1 Abstract

Pancreatic-type ribonucleases show great clinical promise as chemotherapeutic agents but are limited in efficacy by their inefficient cellular uptake. Cellular uptake can be increased by the addition of more positive charges onto the surface of ribonucleases through either site-directed mutagenesis or chemical modification. This observation has led to the current hypothesis that ribonuclease uptake by cells depends heavily on the effects of electrostatics. Recent studies, however, show discrepancies in cellular uptake between ribonucleases with similar total net charge. In this study, we use a combination of experimental and computational techniques to determine the contribution of electrostatics to the cellular uptake of ribonucleases. We focus on three homologous ribonucleases: Onconase (amphibian), RNase 1 (human), and RNase A (bovine). Our results suggest that electrostatics is indeed necessary for the cellular uptake of Onconase whereas for RNase 1 and RNase A, specific interactions on the cell surface must contribute significantly more than do electrostatics for cellular uptake. These results can guide the design to new cytotoxic ribonucleases.

3.2 Introduction

Several members of the pancreatic-type ribonuclease superfamily have been found to be cytotoxic or engineered to be cytotoxic to tumor cells. Onconase (ONC), an amphibian ribonuclease discovered in oocytes from *Rana pipiens*, was found to be selectively toxic to tumor cells and granted orphan drug status from the FDA for the treatment of malignant mesothelioma; however, dose-limiting renal toxicity limits its clinical utility.^{60,28,21,22,61}

Promisingly, cytotoxic variants of mammalian ribonucleases such as human pancreatic ribonuclease (RNase 1) and bovine pancreatic ribonuclease (RNase A), do not demonstrate renal accumulation⁶⁴ and thus show great clinical promise.²¹

A cytotoxic ribonuclease must be internalized by tumor cells, translocate across the endosomal membrane to the cytosol, evade cytosolic ribonuclease inhibitor (RI), and catalyze the degradation of RNA.¹⁸ RI is a ~50-kDa cytosolic protein that binds to ribonucleases, inhibiting their ribonucleolytic activity.¹⁸ ONC is naturally cytotoxic to mammalian cells because it does not bind to RI under physiological conditions.²⁴ Similarly, bovine seminal ribonuclease forms dimers, allowing it to evade RI and demonstrate cytotoxicity.⁹² Conversely, RNase A and RNase 1 bind RI with femtomolar affinity and are not cytotoxic.^{93,26} Variants have been engineered to evade RI, and some of those variants demonstrate cytotoxic activity similar to that of ONC.^{17,29} Although RI evasion is one essential criterion for cytotoxicity, further increases in efficacy relies on increased understanding of ribonuclease internalization.¹⁸

The cytotoxic potential of ribonucleases is limited by its cellular internalization. In the absence of RI, ribonucleases demonstrate picomolar IC_{50} values when injected directly into the cytosol but micromolar IC_{50} values when incubated with cells.³¹ Endocytosis of mammalian RNases occurs via a non-saturable and non-receptor mediated mechanism³² similar to that used by cell-penetrating peptides.⁹⁴ Although ONC has been proposed to bind to two saturable sites on 9L glioma cells with K_D values of 0.25 and 0.062 μM ,³⁴ it demonstrates unsaturable binding to HeLa, K-562, and CHO cells.^{32,35,30}

Increasing the endocytosis of ribonucleases increases its cytotoxicity. For example, the conjugation of RNase A to transferrin, which has a cellular receptor, increases both cellular uptake and cytotoxic activity.⁹⁵ Additionally, increasing the net positive charge (Z) of RNase A and RNase 1 through either site-directed mutagenesis or chemical modification increases endocytosis.^{36,37,72} Because increased charge increases internalization and because a receptor has not been identified, the endocytosis of ribonucleases has been assumed to be mediated by electrostatic forces.²⁹

The second half of cellular uptake involves translocation across the endosomal membrane into the cytosol.²² The translocation efficiency of a ribonuclease may affect its cytotoxic efficacy. In a comparison of dimeric ribonucleases such as bovine seminal ribonuclease, cytotoxicity was shown to be correlated with the ability to disrupt anionic membranes.⁴⁰ RNase A was shown to remain largely in the lysosome for 100 h after endocytosis, demonstrating that its translocation to the cytosol is inefficient.³⁸ ONC is trafficked through the recycling endosomes.³³ While the translocation efficiency and mechanism of ONC is unknown, there is some evidence suggesting the importance of electrostatic interactions for this step. Neutralization of pH in the endosomes results in an increase in ONC cytotoxicity, presumably due to increased ease in translocation.³³ Additionally, the surface electrostatic distribution of ONC was altered by site-directed mutagenesis and was hypothesized to impact the translocation based on resulting changes in cytotoxic efficacy.³⁵

Experimental studies altering surface charge could be confounded by increased or decreased specificity conferred by cationic agents. Theoretical approaches are useful to study the contribution of electrostatics alone and can thus provide insight on the interaction between

the cell surface and ribonucleases and the interaction between the endosomal membrane and ribonucleases. Although explicit molecular dynamics (MD) simulations are computationally expensive, several computational methods using implicit solvents provide reliable information. Numerical solution of the Poisson–Boltzmann (PB) equation can be used to calculate the interaction energy between molecules using continuum electrostatics. The PB approach has been used to calculate the binding energy between rigid proteins and model membranes and to find the energetically favorable orientation for binding.⁵⁷ Of special relevance is the use of PB calculations to predict the orientation of membrane-bound dimeric ribonucleases. These calculations indicated that the ensuing electrostatic energy was correlated with both the ability to disrupt membranes and cytotoxicity.⁴⁰

In this paper, we use computational and experimental approaches to measure the contribution of electrostatics to the binding of ONC, RNase A, and RNase 1 to synthetic membranes. We report the effects of salt concentration on the formation of a protein•membrane complex. Computational analysis is used to propose favorable orientations for ribonucleases to a membrane as well as highlighting differences between the ribonuclease's surface electrostatic distributions. A comparison of PB calculations and simulations using the IMM1–GC model to experimental binding measurements demonstrates the different advantages of each method as well as the quality of their predictions. These results indicate that even simple models can help interpret relevant experimental data and be used to answer relevant biological questions.

3.3 Methods

3.3.1 *Materials*

pET22b(+) plasmid were purchased from Novagen (Madison, WI). BODIPY-FL was purchased from Molecular Probes (Carlsbad, CA). The lipids 1,2-dioleoyl-*sn*-glycero-3-phospho-L-serine (DOPS) and 1,2-dioleoyl-*sn*-glycero-3-phosphocholine (DOPC) were obtained from Avanti Polar Lipids (Alabaster, AL). All other chemicals used were of commercial grade or better, and were used without further purification.

3.3.2 *Analytical Instruments*

Molecular mass was measured by MALDI-TOF mass spectrometry using a Voyager-DE-PRO Biospectrometry Workstation from Applied Biosystems (Foster City, CA). Fluorescence was quantified with an Infinite M1000 plate reader (Tecan, Switzerland).

3.3.3 *Production of Fluorescently-labeled Ribonucleases*

The following free cysteine-variants were purified as described previously for thiol-reactive labeling: S61C ONC,³⁵ P19C RNase 1,²⁹ and A19C RNase A.⁸⁰ The free-cysteine variants were protected with 5,5'-dithio-bis(2-nitrobenzoic acid). Prior to attachment of the fluorogenic label, BODIPY-FL, thionitrobenzoic acid-protected variants were deprotected with a fivefold molar excess of dithiothreitol, then desalted by using a PD-10 desalting column from GE Biosciences (Piscataway, NJ). Deprotected proteins were reacted for 4–6 h

at 25 °C in PBS with a 10-fold molar excess of the thiol reactive BODIPY in DMSO. The reaction was quenched by rapid dilution into 50 mM sodium acetate buffer; pH 5.0. Conjugates were purified using a HiTrap SPHP column and concentrations of conjugates were determined with a bicinchoninic acid assay kit from Pierce (Rockford, IL).

3.3.4 *Large Unilamellar Vesicle Formation*

Large unilamellar vesicles were formed by mixing DOPC and DOPS solvated by chloroform in a 3:2 molar ratio at a 5 mM concentration of total lipid. The lipids were dried under N₂ (g) to remove the chloroform, then dried further under vacuum overnight. The lipids were resuspended in 20 mM Tris-HCl buffer, pH 7.0, containing NaCl (50 mM or 80 mM), by vortexing, and were then allowed to hydrate for 1 h at 37 °C. The vesicles were then extruded 19 times through a 100-nm filter to form large unilamellar vesicles (~130 nm in diameter as confirmed by dynamic light scattering).

3.3.5 *Protein-Liposome Binding Assay*

Fluorescence polarization was used to measure the binding affinity of the fluorescently labeled ribonucleases to liposomes. A two-fold concentration range (4.5 mM → 2.25 nM; 2×) of liposomes was incubated with labeled ribonuclease (50 nM) in 20 mM Tris-HCl buffer, pH 7.0, containing NaCl (50 mM or 80 mM) for 1 h at 23 °C while shaking. At this time, the fluorescence polarization was measured and the value of the equilibrium dissociation constant (K_d) was calculated with the following equation:

$$R = \frac{(R_{\max} - R_{\min})[\text{lipid}]}{K_d + [\text{lipid}]} \quad (3.1)$$

where R is the polarization, R_{\max} is the polarization when the ribonuclease is fully bound, R_{\min} is the polarization when the ribonuclease is fully free, and $[\text{lipid}]$ is the concentration of DOPS.

3.3.6 Poisson–Boltzmann Calculations

Electrostatic calculations were performed with the program APBS 1.2.1.⁹⁶ For the calculations presented herein, the free energy of binding, $\Delta\Delta G_{\text{bind}}$, between the protein and membrane was calculated with the following equation:

$$\Delta\Delta G_{\text{bind}} = \Delta\Delta G_{\text{solv}} + \Delta\Delta G_{\text{coul}} \quad (3.2)$$

where $\Delta\Delta G_{\text{solv}}$ refers to the contribution of solvation to binding and $\Delta\Delta G_{\text{coul}}$ refers to the Coulombic contribution to binding. The solvation contribution to binding was calculated as

$$\Delta\Delta G_{\text{solv}} = \Delta G_{\text{solv-complex}} - \Delta G_{\text{solv-membrane}} - \Delta G_{\text{solv-protein}} \quad (3.3)$$

where the terms refer to the solvation free energy of the membrane•protein complex, the protein, and the model membrane, respectively. The individual free energy terms were calculated by numerical solution of the Poisson–Boltzmann equation

$$-\nabla \cdot \epsilon(\vec{r}) \nabla V(\vec{r}) = \rho_f(\vec{r}) - 2qn_\infty \sinh(qV(\vec{r})/k_B T) \quad (3.4)$$

The Coulombic contribution was calculated as

$$\Delta\Delta G_{\text{coul}} = \Delta G_{\text{coul-complex}} - \Delta G_{\text{coul-membrane}} - \Delta G_{\text{coul-protein}} \quad (3.5)$$

where the terms are the summation of all pairwise Coulombic interactions between all atoms within the membrane•protein complex, the protein, or the model membrane.

The structures of ONC, RNase A, and RNase 1 were taken from PDB codes 1onc,⁷⁷ 1kf5,⁹⁷ and 1z7x,²⁶ respectively. All water molecules were removed from the PDB file before PDB2PQR was used to add hydrogen atoms and atomic charges based on the CHARMM 27 forcefield.⁹⁸⁻¹⁰⁰ The model membrane was approximated by an 80 × 80 Å plane of spheres ($r = 3$ Å; $q = -1$; $\epsilon = 78.50$) with a charge density of 1 sphere/130 Å². The solvation free energy of the protein was calculated with 2 levels of focusing calculations in a 400 × 400 × 400 Å box with a 0.5-Å spacing at the finest level. An implicit solvent was used to model the aqueous solvent with $\epsilon = 78.50$. Dielectric maps of the system were outputted and altered so the dielectric constant below the charged plane of spheres was $\epsilon = 2.0$. These dielectric maps

were used in the calculations for the solvation free energies of the membrane and the membrane•protein complex. The model membrane was placed 5 Å below the bottom of the protein. Conformations of the protein relative to the membrane were sampled by applying a rotation matrix based on Euler's angles ($\theta = 0$; $\phi = 0-2\pi$; $\psi = 0-\pi$) in 15° increments on the protein coordinates.

3.3.7 IMM1–GC Calculations

The IMM1–GC model was used to model an anionic membrane in CHARMM. IMM1–GC is based on the IMM1 model with the addition of a Gouy–Chapman (GC) term to describe the interaction between charged amino acids and the charged bilayer.⁵⁹ The IMM1 models the membrane as a low dielectric slab with a smooth transition to the high dielectric solvent. The IMM1 model is based on the EEF1 model for water-soluble proteins,¹⁰¹ which neutralizes ionic side-chains and uses a linear distance-dependent dielectric constant. The solvation free energy for a protein, ΔG_{solv} , is assumed to be the sum of the solvation free energy for individual atoms within the protein. The effective energy of the protein in the presence of the membrane is given by

$$W_{\text{IMM1-GC}} = E_{\text{intra}} + \Delta G_{\text{solv}} + E_{\text{GC}} \quad (3.6)$$

where E_{intra} is the intramolecular energy of the protein and E_{GC} is the interaction between the charged amino acids and the charged lipid bilayer based on the Gouy–Chapman theory for a diffuse electrical bilayer.¹⁰²

The initial coordinates were taken from the same PDB files as for the PB calculations above. Six different initial orientations were generated with each one corresponding to the face of a cube containing the ribonuclease. The membrane was placed 3 Å below the bottom of the protein perpendicular to the z -axis. The salt concentration was set to 0.1 M, the area per lipid to 32 Å², and the anionic fraction of the membrane to 40% to match the experimental fluorescence polarization conditions. MD simulations were performed using CHARMM (c35a1)¹⁰³. The backbone atoms were constrained using an rmsd constraint. The structures were equilibrated for 100 ps at 298 K and then run for another 2000 ps. The conformations were stored every 0.5 ps and used to calculate the effective energy of the protein in solvent and in the presence of a membrane. A total of 12 simulations were run for each protein. The average binding energy was calculated by averaging the binding energy over the last 2 ns of the simulation and a trajectory was said to bind if the binding free energy is stronger than −0.8 kcal/mol.

3.4 Results

3.4.1 Production of Labeled Ribonucleases

As explained above, the binding of ribonucleases to the cell surface was assumed to be mediated primarily by electrostatic force.²⁹ Therefore, the ribonucleases were labeled in areas

(residue 61 in ONC; residue 19 in RNase A and RNase1) with few cationic residues, as these areas were deemed unlikely to interfere with the binding of the ribonucleases to the lipid vesicles. After purification and labeling, the mass of the labeled proteins was determined by using MALDI-TOF spectroscopy (S61C ONC: m/z 12,250; expected: 12,239, A19C RNase A: m/z 14129; expected: 14096, P19C RNase 1: m/z 15,042; expected: 15,014).

3.4.2 Ribonuclease-LUV Binding Affinity

The contribution of electrostatics to the internalization of ribonucleases and endosomal translocation has been difficult to study. Although increasing net positive charge has been shown to increase cellular internalization, this finding could be confounded by specificity induced by the cationization agents. For example, heparan sulfate was found to compete with the cell surface for a RNase A variant altered by polyethylenimine.⁷² Secondly, differences between homologous ribonucleases involving cellular trafficking and sequence variation make it difficult to generalize findings based on charge alone. To simplify the analysis, we directly compared the binding of RNase A, RNase 1, and ONC to large unilamellar vesicles containing 40% phosphatidylserine. Phosphatidylserine has a net negative charge and normally resides in the cytoplasmic leaflet of the lipid bilayer; however, in cancerous cells, it relocates to the extracellular leaflet.¹⁰⁴

The binding affinity of ribonucleases for phosphatidylserine is shown in Figure 3.1. RNase A did not bind to LUVs at either salt concentration. ONC demonstrated some binding

to LUVs at low salt conditions. RNase 1 bound to LUVs at low salt conditions with a K_d value of 27 μM and at high salt concentrations with much less affinity.

3.4.3 Poisson–Boltzmann Calculations

Poisson–Boltzmann calculations were performed to determine the most favorable orientation for ribonucleases to bind a model membrane. The electrostatic map for RNase A reveals that the most energetically favorable orientation has its active site facing the membrane (Figure 3.3a–c.). This orientation provides, however, low affinity ($K_D \sim 20 \text{ mM}$). This computational result is consistent with experimental values showing that RNase A does not bind to LUVs (Figure 3.1). Like RNase A, RNase 1 orients itself so that its active site faces the membrane but RNase 1 binds much more strongly than does RNase A (Figure 3.2a–c.). The predicted value of K_D is 2 mM, which is consistent with the experimental binding seen (Figure 3.1). Interestingly, for both RNase A and RNase 1, the loops that mediate binding to RI also seem to be important for membrane binding. On the other hand, ONC can bind favorably with part of the active site facing the membrane (Figure 3.4a–c.), or in the opposite orientation, which is the least favorable and highly repulsive orientations for RNase A and RNase 1. Moreover, ONC appears to be weakly attractive in any orientation and the most favorable orientation for ONC is only 3-fold more likely than a random orientation. Overall, however, ONC, similar to RNase A, is predicted to bind with low affinity at high salt, consistent with experimental results (Figure 3.1).

The PB calculations predicted whether or not ribonucleases would bind at the higher salt condition. In contrast, discrepancies appeared at lower salt conditions. As seen in Figure 3.1,

the calculated binding free energy for RNase 1 in the low salt condition corresponds to a K_d value of 350 μM but the experimental K_d value is $27 \pm 2 \mu\text{M}$. Similarly, ONC is calculated to have a K_d value of $\sim 8 \text{ mM}$ in low salt conditions but the experimental K_d value is undeterminable from the data. Lastly, although RNase A should display binding similar to ONC based on the results from PB calculation, it does not bind experimentally. These discrepancies could be due to the possible specificity of ONC and RNase 1 for phosphatidylserine.

3.4.4 IMM1-GC Simulations

Whereas the PB calculation results compared well with experimental values, they did not allow for side-chain rearrangements or measure hydrophobic interactions. Hence, we carried out multiple short molecular dynamic simulations using the IMM1-GC model. In the simulations, the main chain was constrained, but side chains were unconstrained and the protein was allowed to rotate and translate. For ONC, because the PB calculation did not predict a favorite or an unfavorable orientation, we were surprised to see that only 7 of the 12 trajectories resulted in binding, although the average binding free energies were comparable to those from the PB calculations. Representative trajectories of simulations that result in a bound and unbound ONC are shown in Figure 4.4d and 4.4e. Although the bound trajectory remains in the areas that are most energetically favorable, as seen in Figure 4.4a, the unbound trajectory was started in a less energetically favorable area where the binding free energy was insufficient to keep ONC on the membrane long enough for it to rotate to a more energetically

favorable orientation. The two simulations starting from orientation $\theta = 270^\circ$, $\psi = 90^\circ$ also demonstrate this phenomenon. While they both move away from the membrane due to a lack of favorable interactions, in simulation 1, ONC does not rotate into a conformation allowing it to return to the membrane whereas, in simulation 2, ONC rotates so its most favorable side faces the membrane, allowing it to return and bind with a final energy of -2 kcal/mol. In contrast to ONC, RNase A and RNase 1 bound in 9 of the 12 trajectories. The energies are quite comparable to those of the PB calculations and the trajectory snapshots follow the energetics predicted by the PB calculations. Lastly, none of the proteins showed insertion into the membrane although they remained close to the membrane. The average predictive binding energy is a measure of how much time the protein remained close to the membrane.

3.5 Discussion

A major factor that limits the efficacy of many proteins as putative chemotherapeutic agents is their cytosolic delivery.¹⁰⁵ Without a receptor, cytotoxic ribonucleases must be endocytosed and escape the endosome.¹⁸ Here, we use a combination of experimental and computational techniques to compare and contrast the effect of electrostatic distribution on the interaction of ONC, RNase A, and RNase 1 with lipid bilayers as a model for better understanding factors that contribute to lipid interaction and translocation.

ONC is internalized by cells via bulk endocytosis and our results suggest that electrostatic forces are sufficient to cause a weak association with the cell surface, where ONC remains until internalized via bulk-rate endocytosis.³⁰ Although computational results predicted a

weak affinity for a negatively-charged surface, they demonstrated that ONC spent the larger part of its simulation time associated with the surface. Because bulk endocytosis occurs constitutively, time spent at the cell surface is critical for internalization. We suggest that the low rate of ONC uptake is explained by its low binding energy combined with a lack of a cell-surface binding partner.

Comparing the cellular uptake to the calculated binding energies for RNase A reveals unusual disparities as compared to ONC and RNase 1. Calculations predicted that RNase A would have a cell-surface affinity similar to that of ONC, yet it is internalized by cells at a rate that is ~2 orders of magnitude greater than that of ONC.³⁰ Recently, removal of heparan and chondroitin sulfate was found to reduce by 4-fold the internalization rate of an RI-evasive variant of RNase A but not affect that of ONC.³⁰ The presence of a cell-surface moiety with affinity for RNase A but not ONC explains this discrepancy between predicted and experimental results. RNase A ($Z = +4$) and RNase 1 ($Z = +6$) display similar levels of cellular uptake,²⁹ even though RNase 1 has a higher density of positive charge at its active site than does RNase A, demonstrates a salt dependence in its lipid binding, and has a much higher predicted binding free energy. It is possible that RNase A has a greater affinity for cell-surface moieties than does RNase 1, but this discrepancy is consistent with the conferral of specificity for moieties on the cell surface being more efficient than increasing the positive charge as a means to increase cellular uptake.

As the endosome is acidified, heparan sulfate is cleaved from the membrane by glycosidases, resulting in the core phospholipid bilayer.¹⁰⁶ RNase 1 has been shown to disrupt large unilamellar vesicles containing DOPG, another anionic lipid, whereas RNase A cannot.

Nor does RNase A bind to DOPG-containing vesicles.⁴⁰ Although phosphatidylserine is upregulated on the cell surface of cancerous cells, ribonuclease access to phosphatidylserine could be obscured by the glycocalyx, meaning that specificity for cancerous cells could take place within the endosome, when ribonucleases encounter phosphatidylserine.

PoissonBoltzmann calculations were used to predict binding constants and whether membrane binding would or would not occur for these three ribonucleases. Given the simplicity of the lipid bilayer model, which consists of an implicit solvent and a plane of negatively charged spheres, above a low-dielectric slab, its consistency with experimental data is encouraging. The simplicity of the lipid bilayer model decreases computational cost compared to explicit lipid models. The PB calculations predicted favorable orientations well as compared to the IMM1–GC simulations and estimated the energetic landscape of the membrane•protein complex.

IMM1–GC simulation results were consistent with PB calculation results and with experimental results. They provided additional insight by clarifying the necessary strength of an interaction for a long-lasting stable interaction to occur in the membrane•protein complex and by showing that hydrophobic interactions are involved only minimally. The lack of ribonuclease penetration of the membrane suggests that in contrast to cell-penetrating peptides,⁵⁹ ribonucleases require more than electrostatic or hydrophobic forces to penetrate a lipid bilayer. IMM1–GC simulations required much less computational resources as compared to the PB calculations and provided more information, making this an attractive option for future studies of protein•membrane complexes.

Previous studies have shown that net charge is correlated with cytotoxicity. Our data supports the hypothesis that whereas electrostatic forces alone are sufficient for cell–surface association and endocytosis. Although they are sufficient, electrostatic forces result in a very weak affinity. Future designs of proteins undergoing cationization should include cationization agents with specificity for cell–surface moieties. Additionally, contrasting experimental and computational data for the contribution of electrostatics can provide insight into the search for cell surface binding partners for proteins.

Acknowledgements. We are grateful to S. Yang for his technical expertise, and C. Tanrikulu, G.A. Ellis, and E. Smith for contributive discussions. This work was supported by Grant R01 CA073808 (NIH) and Grant CHE-0840494 (NSF). N.K.S. was supported by Molecular Biophysics Training Grant T32 GM008293 (NIH).

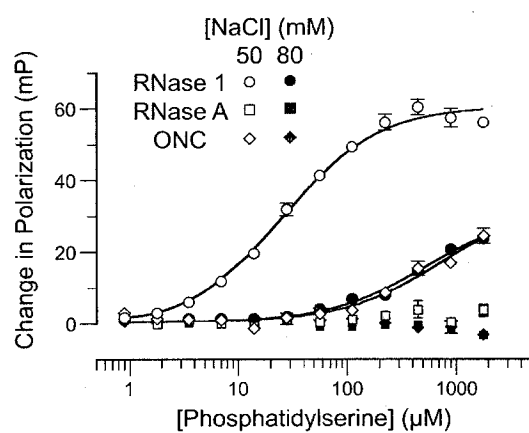
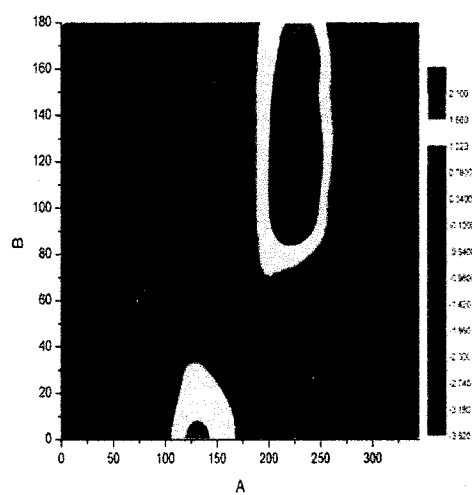


Figure 3.1 Ribonuclease binding isotherms toward phosphatidylserine liposomes. Binding events were measured by fluorescence polarization using fluorescently conjugated ribonucleases and increasing concentration of liposomes containing DOPC and DOPS at a ratio of 3:2. Data were fitted by a non-linear regression curve using GraphPad Prism 5.

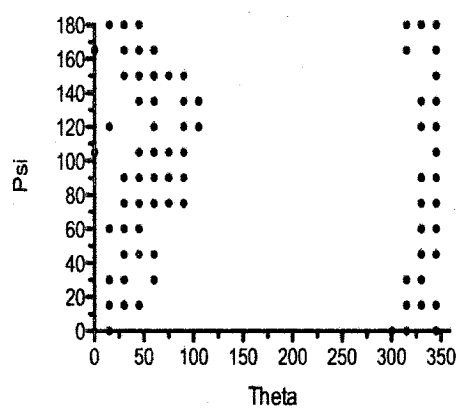
Figure 3.2 Computational calculation of the binding of RNase 1 to model membranes.

A. Poisson–Boltzmann calculations of the electrostatic free energy of interaction between RNase 1 (PDB entry 1z7x), rotated using Euler angles ($\theta = 0\text{--}360^\circ$; $\psi = 0\text{--}180^\circ$; increments of 15°), with a model membrane with an anionic fraction of 1 electron per 130 Å. B. Representative trajectory resulting in protein•membrane binding from IMM1–GC simulation (2 ns). This illustrates the sampling of orientations of RNase 1 with respect to a model membrane when bound. C. Depiction of RNase 1 with a model membrane in the most energetically favorable orientation from the PB calculations made with PYMOL. D. Depiction of RNase 1 with a model membrane in the least energetically favorable orientation from the PB calculations made with PYMOL.

A



B



C



D

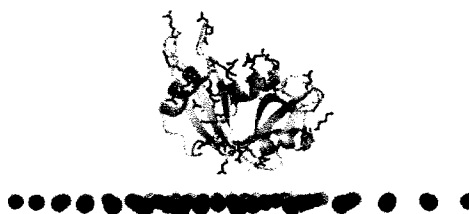
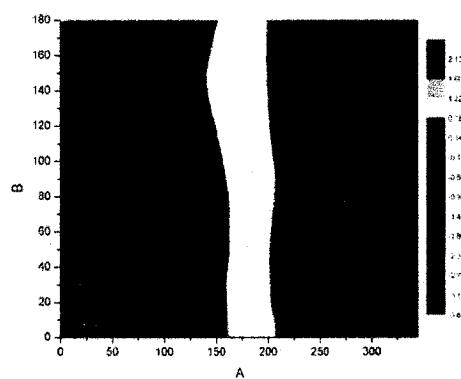


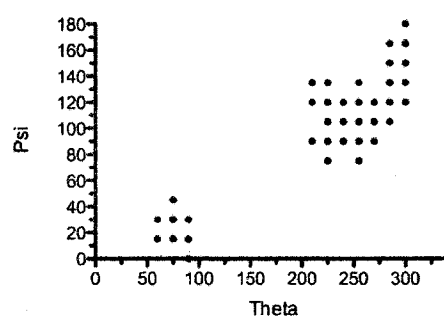
Figure 3.3 Computational calculation of the binding of RNase A to model membranes.

A. Poisson–Boltzmann calculations of the electrostatic free energy of interaction between RNase A (PDB entry 1kf5), rotated using Euler angles ($\theta = 0\text{--}360^\circ$; $\psi = 0\text{--}180^\circ$; increments of 15°), with a model membrane with an anionic fraction of 1 electron per 130 Å. B. Representative trajectory resulting in protein•membrane binding from IMM1–GC simulation (2 ns). This illustrates the sampling of orientations of RNase A with respect to a model membrane when bound. C. Depiction of RNase A with a model membrane in the most energetically favorable orientation from the PB calculations made with PYMOL. D. Depiction of RNase A with a model membrane in the least energetically favorable orientation from the PB calculations made with PYMOL.

A



B



C



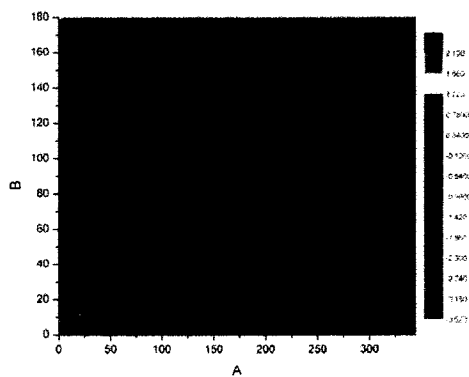
D



Figure 3.4 Computational calculation of ONC binding to model membranes

A. PoissonBoltzmann calculations of the electrostatic free energy of interaction between RNase 1 (PDB entry 1onc), rotated using Euler angles ($\theta = 0-360^\circ$; $\psi = 0-180^\circ$; increments of 15°), with a model membrane with an anionic fraction of 1 electron per 130 Å. B. Depiction of ONC with a model membrane in the most energetically favorable orientation from the PB calculations made with PYMOL. C. Depiction of ONC with a model membrane in the least energetically favorable orientation from the PB calculations made with PYMOL. D. Representative trajectory resulting in protein•membrane binding during IMM1–GC simulation (2 ns). This illustrates the sampling of orientations of ONC with respect to a model membrane when bound for the entire simulation time. E. Representative trajectory resulting in protein•membrane dissociation during IMM1–GC simulation (2 ns). This illustrates the sampling of orientations of ONC with respect to a model membrane that does not lead to formation of a stable protein•membrane complex.

A



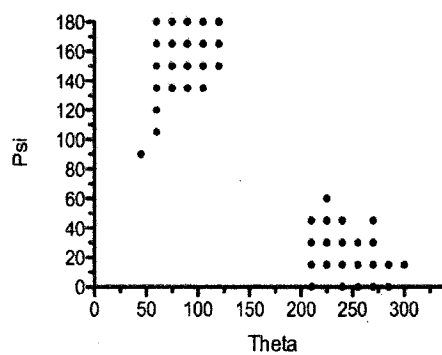
B



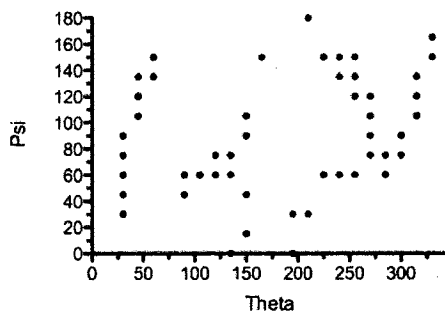
C



D



E



Ribonuclease	Observed		Calculated	
	[NaCl] (mM)	K_d (mM)	$\Delta G_{\text{binding}}$ (kcal/mol)	$\Delta G_{\text{binding}}$ (kcal/mol)
RNase 1	50	0.027 ± 0.002	-6.23 ± 0.02	-4.7
RNase 1	80	0.5 ± 0.1	-4.5 ± 0.1	-3.6
RNase A	50	>1.8	>-3.7	-2.8
RNase A	80	>1.8	>-3.7	-2.2
ONC	50	0.7 ± 0.2	-4.3 ± 0.2	-3.1
ONC	80	>1.8	>-3.7	-2.5

Table 3.1 Observed and calculated affinity of ribonucleases for a phosphatidylserine membrane.

Experimental data were determined by fluorescence polarization in 20 mM Tris-HCl buffer, pH 7.0. Calculated data were determined by Poisson-Boltzmann analysis.

Table 3.2 Summary of IMM1–GC simulations

Each ribonuclease was rotated using Euler angles to obtain 6 starting orientations. Two independent simulations were run for each orientation for 2 ns and the average binding energy is reported here.

	Starting Orientation	Binding Energy (kcal/mol)
ONC	$\theta = 0; \psi = 0$	-2.0 ± 0.5
		-2.5 ± 0.7
	$\theta = 180; \psi = 0$	-1.5 ± 0.7
		-2.0 ± 0.6
	$\theta = 270; \psi = 0$	-1.5 ± 1.2
		-2.6 ± 0.4
	$\theta = 270; \psi = 90$	-0.2 ± 0.4
		-0.8 ± 0.8
	$\theta = 90; \psi = 0$	0.0
		-0.1 ± 0.3
RNase 1	$\theta = 90; \psi = 90$	-0.2 ± 0.5
		0.0 ± 0.1
	$\theta = 0; \psi = 0$	0.0
		0.0
	$\theta = 180; \psi = 0$	-3.9 ± 0.9
		-4.4 ± 0.7
	$\theta = 270; \psi = 0$	-0.1 ± 0.6
		-2.2 ± 1.5
	$\theta = 270; \psi = 90$	-3.4 ± 0.9
		-3.4 ± 0.7
RNase A	$\theta = 90; \psi = 0$	-3.3 ± 0.9
		-4.0 ± 0.8
	$\theta = 90; \psi = 90$	-3.2 ± 1.0
		-3.0 ± 1.2
	$\theta = 0; \psi = 0$	-0.6 ± 0.9
		-2.2 ± 0.7
	$\theta = 180; \psi = 0$	-2.9 ± 0.5
		-2.6 ± 0.6
	$\theta = 270; \psi = 0$	0.0
		-0.1 ± 0.3
	$\theta = 270; \psi = 90$	-1.1 ± 1.3
		-2.5 ± 0.6
	$\theta = 90; \psi = 0$	-2.1 ± 0.7
		-1.6 ± 1.0
	$\theta = 90; \psi = 90$	-1.8 ± 0.8
		-1.3 ± 0.9

CHAPTER 4

Disruption and Formation of Surface Salt Bridges are Coupled to DNA Binding by Integration Host Factor: A Computational Analysis

Contribution:

This chapter was published as:

Ma, L., Sundlass, N. K., Raines, R. T., Cui, Q. (2011). Disruption and formation of surface salt bridges are coupled to DNA binding by Integration Host Factor: A computational analysis. *Biochemistry* **50**, 266-275.

4.1 Abstract

Revealing the thermodynamic driving force of protein–DNA interactions is crucial to the understanding of factors that dictate the properties and function of protein–DNA complexes. For the binding of DNA to DNA-wrapping proteins, such as the integration host factor (IHF), Record and co-workers have proposed that the disruption of a large number of pre-existing salt-bridges is coupled with the binding process [Holbrook, J.A., et al. (2001) *J. Mol. Biol.* 310, 379]. To test this proposal, we have carried out explicit solvent MD simulations (multiple ~25–50 ns trajectories for each salt concentration) to examine the behavior of charged residues in IHF, especially concerning their ability to form salt bridges under different salt concentrations. Of the 17 cationic residues noted by Record and co-workers, most are engaged in salt-bridge interactions for a significant portion of the trajectories, especially in the absence of salt. This observation suggests that, from a structural point of view, their proposal is plausible. However, the complex behaviors of charged residues observed in the MD simulations also suggest that the unusual thermodynamic characteristics for IHF–DNA binding likely arise from the interplay between complex dynamics of charged residues both in and beyond the DNA binding site. Moreover, a comparison of MD simulations at different salt concentrations suggests that the large dependence of the IHF–DNA binding enthalpy on salt concentration may not be due to a significant decrease in the number of stable salt bridges in apo IHF at high salt concentration. In addition to the Hofmeister effects quantified in more recent studies of IHF–DNA binding, we recommend consideration of variation of the enthalpy change of salt bridge disruption at different salt

concentrations. Finally, the current simulation study explicitly highlights that the electrostatic properties of DNA-binding proteins can be rather different in the apo and DNA-bound states, which has important implication to the design of robust methods for predicting DNA binding sites in proteins.

4.2 Introduction

Protein–DNA complexes play multiple important roles in cellular processes that involve DNA “transactions”, such as replication, transcription, recombination and repair as well as the packaging of chromosomal DNA.¹⁰⁷ Proteins that interact with DNA in these complexes either serve as enzymes [e.g., DNA polymerase]¹⁰⁸ to catalyze biochemical reactions or simply act as an “architectural scaffold”¹⁰⁹ to manipulate the structure of DNA by, for example, bending and/or wrapping DNA. Well-known examples in the latter category include Integration Host Factor (IHF)^{110,111} and HU.¹¹¹ Due to significant structural deviation from the equilibrium form of DNA (most often from the B-form), the mechanical work associated with DNA bending/wrapping needs to be compensated by the free energy gain of protein/DNA binding.^{112,113} Therefore, it is important to understand the thermodynamic driving force of protein–DNA binding, especially for architectural scaffolding proteins.

IHF is a remarkable example for DNA-bending/wrapping proteins.^{110,111} It bends the specific 34 bp DNA segment by as much as $\sim 160^\circ$, as illustrated by the crystal structure of an IHF–DNA complex¹¹⁴ (see Figure 4.1a). To investigate the mechanism of IHF–DNA binding, Record and co-workers¹¹⁵ explored extensively the thermodynamics of specific and non-

specific interactions between IHF and DNA using isothermal titration calorimetry. These experiments revealed several unusual thermodynamic features of IHF–DNA interactions: i) the binding is highly exothermic and strongly enthalpy-driven while being entropically unfavorable; ii) the measured salt concentration dependence of the binding constant, SK_{obs} is much smaller in magnitude than that estimated based on the oligocation model of the binding interface; iii) The enthalpy change $\Delta H_{\text{sp}}^{\circ}$ and heat capacity change $\Delta C_{\text{sp}}^{\circ}$ of the specific binding are strongly dependent on the salt concentration [KCl] and their magnitudes decrease significantly with increasing [KCl] between 100 mM and 350 mM.

To rationalize these unexpected features, Record and co-workers proposed that IHF–DNA binding is coupled with the disruption of a large number of salt bridges that exist in the unbound form of IHF.¹¹⁵ In the crystal structure for the IHF–DNA complex,¹¹⁴ there are 23 cationic residues located within 6 Å from DNA phosphoryl groups.¹¹⁵ This number is significantly larger than the average value (~12) found based on a large database of protein–DNA complexes.¹¹⁶ Interestingly, there are also many anionic residues near these cationic residues. Based on an analysis of the position of these charged residues, Record and co-workers suggested that 19 out of these 23 cationic residues can form salt bridges with nearby anionic residues following either side-chain rotations or backbone movements of flexible regions in the protein.¹¹⁵ Accordingly, they proposed that these salt bridges exist in the unbound form of IHF and get disrupted upon DNA binding and that disruption of salt bridges is the origin of the unusual thermodynamic features of the binding process. For example, the enthalpy change of salt bridge disruption is known to be negative,¹¹⁷ which explains the large exothermicity (enthalpic change) of the overall IHF–DNA binding process. They also

proposed that the salt bridges become unstable at high K^+ due presumably to the screening effect of salt ions; the disruption of a reduced number of salt bridges during binding then decreases the magnitude of enthalpy change at high K^+ , which was observed experimentally. Moreover, in a recent review article,¹¹⁸ Saecker and Record further speculated that the disruption of surface salt bridges coupled to DNA binding may not be unique to IHF and may occur in other DNA-wrapping proteins as well, highlighting the possible generality of this phenomenon and its potential role in regulating DNA wrapping. Recent studies of Grove and co-workers have pointed to the potential involvement of surface salt bridges in determining the length of DNA binding site in HU.^{119,120}

Because the proposal of salt bridge disruption was based on a structural analysis of the IHF–DNA complex, one may argue that the evidence is indirect without a high-resolution structure for IHF in the unbound state. For example, considering the small free energy gain associated with salt bridge formation at protein surface,^{121,122} it is not clear if a large number (~23) of surface salt bridges would exist in the unbound state of IHF. Moreover, the simulation study of Elcock and co-workers found that the stability of salt bridges is only marginally perturbed by salt concentration up to 2 M,¹²³ thus the observed KCl dependence of IHF–DNA binding thermodynamics in experiments may not be due to perturbations in the number of stable salt bridges.¹¹⁵ Indeed, more recent analysis of Vander Meulen et al.¹²⁴ that compared binding thermodynamics of IHF–DNA in different salt solutions (KCl, KF, and KGlu) indicated that the large salt dependence of the binding enthalpy is a Hofmeister effect arising from interaction of Cl^- with the surfaces buried in binding. Nevertheless, the

extrapolated binding enthalpy at low salt is still highly negative, which is consistent with the salt bridge disruption model.

These considerations have stimulated us to carry out molecular dynamics simulations to investigate salt bridge dynamics in IHF (see Figure 4.1b for snapshots). Considering the size of the system and complexity of the DNA binding process, we do not anticipate a quantitative comparison to experiments. The goal of the study is to explore whether the salt bridges proposed by Record and co-workers¹¹⁵ are able to form and remain stable when IHF is not interacting with DNA. Along this line, we note that IHF has a large number of charged residues (36 cationic and 28 anionic residues out of 190 residues in total); thus it is interesting to investigate whether the salt bridges near the DNA binding site behave differently compared to other charged residues. In addition, we seek to investigate whether the propensity of salt bridge formation is perturbed by the presence of salt (K^+). Finally, because salt bridge formation and disruption are expected to significantly perturb electrostatic properties, which are used in many algorithms aimed at predicting DNA binding sites in proteins, it is of great interest to explore how sampling salt bridge dynamics impacts such predictions.

4.3 Methods

4.3.1 *Molecular Dynamics Simulations of IHF in the Unbound State*

Because the structure of the apo form of IHF is not available, we generate a model by simply removing DNA from the crystal structure of the IHF–DNA complex [PDB code 1IHF].¹¹⁴ Starting from this structure, MD simulations are carried out at two KCl

concentrations: 0 mM (termed “no-salt”) and 350 mM (termed “high-salt”); 350 mM is chosen because it was the highest salt concentration investigated in the experiments of Record and co-workers.¹¹⁵ The simulations are performed using the GROMACS program^{125 126} with the OPLS-AA force field¹²⁷ for IHF and ions. To set up the simulation, IHF is first solvated with a rhombic dodecahedron solvent box of TIP4P water¹²⁸ ($a = b = c = 100 \text{ \AA}$). The TIP4P water model is adopted due to its compatibility with the OPLS-AA force field. K^+ and Cl^- ions were then added into the simulation box according to the proper salt concentration. Since IHF bears a net charge of +8, 8 Cl^- ions are added in the no-salt system, and 149 K^+ and 157 Cl^- ions are added in the high-salt system, to achieve overall charge neutrality; snapshots of the two systems are shown in Figure 4.1. Periodic boundary condition is applied and long-range electrostatics are treated by the particle mesh Ewald method.¹²⁹ For van der Waals interactions, a switching cutoff scheme for interatomic distances between 10 and 12 \AA is used.¹³⁰ The SETTLE¹³¹ (for water) and SHAKE¹³² (for protein) algorithms are applied to constrain bonds involving hydrogen atoms to allow an integration time step of 2 fs. The systems are equilibrated for 1 ns at 300K with the NVT ensemble, which is followed by 25–50 ns production runs with the NPT ensemble; three independent trajectories are carried out for each salt concentration. Temperature was controlled using the Nose-Hoover scheme^{133 134} and pressure was controlled with the Berendsen scheme.¹³⁵ Considering the large number of charged residues in IHF (36 cationic and 28 anionic), we expect that three independent 25–50 ns trajectories are sufficient for observing statistically meaningful behaviors of salt bridges (see Figures 4.4–4.10).

Because the system has many titratable residues, it is of interest to question whether many residues adopt an unexpected protonation state. Considering the fairly large conformational changes during the simulation, we did not pursue computationally intensive pK_a analysis such as with MCCE;¹³⁶ this is in part justified by the observation that most titratable residues are solvent accessible and therefore not expected to have very large pK_a shift. This is confirmed by running pK_a calculations with the empirical PROPKA approach^{137 138} with several different snapshots from the MD simulations; all Glu/Asp residues are predicted to be deprotonated and Lys/Arg protonated. Along the same line, our work addresses salt-bridge interactions involving residues that are largely solvated rather than buried in the protein interior; thus, the lack of explicit polarization in the force field is unlikely a serious issue. Recent analysis highlights that including polarization is most essential in problems that involve polar–nonpolar interfaces.^{139 140 141}

4.3.2 *Calculations of Protein Surface Electrostatic Potential*

To compare the electrostatic properties of IHF in different structures, we performed linear PB calculations. Calculations are done using the PBEQ module in CHARMM¹⁰³ and the molecular surface is adopted to define the dielectric boundary between protein and solvent. Specifically, the set of atomic radii developed by Roux and co-workers¹⁴² is used together with a solvent probe radius of 1.4 Å and an ion-exclusion layer of 2 Å. The partial charges for protein atoms are adopted from the standard CHARMM 27 force field.⁹⁸ The multigrid setup was used to solve PB numerically and the focusing scheme was applied: the coarser grid is 160 Å × 160 Å × 160 Å with 1.0 Å spacing and the finer grid is 82 Å × 68 Å × 64 Å with 0.4

Å spacing. The salt concentration was set as the physiological concentration of 0.15 M, and the dielectric constant was set to be 2 and 80 for the protein and water, respectively. The electrostatic potential ϕ_i was first calculated for each grid point i in the finer grid enclosing the protein; the values were then used to compute residue-averaged electrostatic potential (ϕ_{res}^j) using the PBAV option in CHARMM.¹⁰³ Specifically, ϕ_{res}^j is the average of ϕ_i over all grid points i that belong to a residue j (within the van der Waals radii of all atoms of residue j):

$$\phi_{\text{res}}^j = \frac{1}{N_j} \sum_{i \in j}^{N_j} \phi_i \quad (4.1)$$

where N_j is the number of grid points that belong to residue j .

4.3.3 Prediction of DNA Binding Interface

To investigate how change in electrostatic potentials (due to salt bridge rearrangements) impact prediction of DNA binding site (see Impact on the Prediction of DNA Binding Sites for a detailed discussion), we select two popular web servers that predict DNA binding interface in proteins. The first one is patch plus finder (PPF)¹⁴³ (<http://pfp.technion.ac.il/>), which finds the largest continuous patch on the protein surface that has positive electrostatic potential. The second one is Preds^{144 145} (<http://pre-s.protein.osaka-u.ac.jp/preds/>), which predicts whether a protein is capable of binding DNA and, if so, the location of the binding interface. The prediction is characterized by a statistical score, P_{score} , which is calculated

based mainly on the surface electrostatic potential and the molecular shape of the protein. The only required input for both web servers is the protein structure in the standard PDB format.

4.3.4 *Salt Dependence of Thermodynamics of Salt-Bridge Interactions*

To qualitatively probe the salt dependence of the thermodynamic quantities (in particular the enthalpy change) of salt-bridge interactions, we have computed the potential of mean force (PMF) for the association of K^+ and Cl^- at three KCl concentrations (0.2 M, 0.5 M and 0.8 M) at three temperatures (280 K, 300 K, 320 K). The OPLS-AA force field and TIP4P water model are used in the simulations. The PMF is directly inverted from the KCl radial distribution function, and the enthalpic/entropic components for the association/dissociation are calculated based on simple finite difference and shown in Table 4.3.

4.4 Results and Discussion

Although three independent trajectories are calculated for each salt concentration, the results are qualitatively similar. Therefore, in the following discussions, unless explicitly stated, results for the longest simulation (50 ns) are discussed.

4.4.1 *Overall Conformational Stability of IHF in the Absence of DNA*

Without the DNA, it is expected that the structure of IHF undergoes relaxation away from its conformation in the IHF–DNA complex (which is the starting configuration of the MD

simulations). IHF is a heterodimer with two subunits, α and β , and can be divided into two domains according to secondary structure content and functional roles. The first domain (residues excluding 54 to 77 on both subunits, shown in green in Figure 4.2a) is made up of mainly α helices and is named as the core domain; the second "arm" domain (residue 54 to 77 on both subunits, shown in yellow in Figure 4.2a), on the other hand, consists mainly of β sheets and embraces the bound DNA in the IHF–DNA complex. As shown in Figure 4.2a, the core domain is relatively stable and the arm domain has more significant conformational changes during the MD simulations. To analyze the structural transitions more quantitatively, the RMSD of the backbone non-hydrogen atoms in the two domains were calculated along MD trajectories relative to the starting structure; the backbone non-hydrogen atoms of the core domain are used as the reference for best-fit in the RMSD calculations. As shown in Figure 4.2b, the RMSD of the core domain is ~ 2 Å throughout the 50 ns simulations at both no salt (0 mM KCl) and high-salt (350 mM KCl) conditions, which indicates that the core domain remains stable in the absence of DNA. The RMSD of the arm domain, however, can be as large as ~ 10 Å in both sets of trajectories, suggesting that the arm domain, which embraces DNA in the complex, becomes very floppy after DNA is removed. Moreover, the β -sheet structure in the arm domain (colored purple in Figure 4.2a) undergoes partial unfolding during simulations, which hints at the possibility that IHF–DNA binding is coupled with a local folding transition in the arm domain, which is often observed in the formation of specific protein–DNA complexes.¹⁴⁶

4.4.2 Salt Bridge Dynamics

In the proposal by Record and co-workers,¹¹⁵ 19 of the 23 cationic residues in the DNA binding interface have the potential to (re)form salt bridges with nearby anionic residues in the absence of DNA. The potential salt bridge partners for two His residues (H54 and H79) on the β subunit are two anionic residues (D98 and D99) near the C-terminus of the α subunit, which is missing in the crystal structure of the IHF–DNA complex and therefore not included in our simulation. Thus, these two His residues are not included in the subsequent analysis, and we focus on the remaining 17 cationic residues (all are Lys or Arg); they are referred to as the 17 binding-site cationic residues. Moreover, as mentioned in the introductory section, there are in total 36 cationic residues in IHF, thus we also explore the behaviors of the remaining 19 cationic residue in terms of the formation of salt bridge interactions.

4.4.2.1 Distribution of Salt Bridge Distances.

To analyze the propensity of all 36 cationic residues toward forming salt bridge interactions, we first monitor the shortest distance between the nitrogen atoms of each cationic residue and the oxygen atoms in all anionic residues ($r_{\text{min-NO}}$). To establish a distance criterion for defining salt bridge formation, a classical statistical study concluded that $r_{\text{min-NO}} \leq 4 \text{ \AA}$ should be used because this criterion leads to the largest difference in the frequency of observing oppositely charged pairs versus likely charged pairs in protein crystal structures.¹⁴⁷ In the analysis of Record and co-workers;¹¹⁵ however, an $r_{\text{min-NO}}$ of $\leq 3 \text{ \AA}$ was used instead as a criterion for dehydrated (i.e. no solvent between) salt bridges. To determine which criterion

is more appropriate for the current study, we calculate the normalized histogram, $H(r_{\text{min-NO}})$, for all 36 cationic residues collected from both no-salt and high-salt simulations; the volume factor $4\pi r_{\text{min-NO}}^2$ is not included for simplicity. As shown in Figure 4.3, there is a large and sharp peak between 2 and 3.5 Å, which corresponds to the dehydrated salt bridge state, and another small peak (shown in the inset of Figure 4.3) between 3.5 and 5.5 Å, which corresponds to the solvent-mediated ion pair. In a recent computational study of acetate–methylammonium (model compounds for salt bridges) association, three minima were observed in the potential of mean force: one for the direct (dehydrated) interaction and another two for solvent-separated interactions.¹²³ The positions of the first two minima in that work are essentially the same as those found here. The boundary between the two peaks in Figure 4.3 falls around 3.3 Å; therefore, the distance criterion for defining a dehydrated salt bridge is chosen as $r_{\text{min-NO}} \leq 3.3$ Å, which is used in all subsequent analysis. This criterion is similar to that used by Record and co-workers¹¹⁵ while more strict than that from the statistical study.¹⁴⁷ Comparison between the no-salt and high-salt results in Figure 4.3 suggests that an increasing salt concentration decreases the probability of forming dehydrated salt bridges (the first peak) and the solvent-mediated ion pair (the second peak); as discussed in more detail below, however, the magnitude of the effect is rather small.

4.4.2.2 Salt bridge formation for the 17 binding-site cationic residues in the absence of KCl

As shown in Figure 4.4–4.10, there is complex behavior in the salt-bridge dynamics. The salt bridge formation probability P for a specific cationic residue is defined as the fraction of

simulation time during which this residue is engaged in a salt bridge interaction as determined based on the criterion $r_{\text{min-NO}} \leq 3.3 \text{ \AA}$. Although we have only carried out three 25–50 ns trajectories for each salt concentration, there are significant fluctuations in the salt-bridge distances during the simulations for most cationic residues. Therefore, the overall trends in P are expected to be meaningful; thus, the qualitative behaviors of the salt-bridges are fairly similar among the three independent trajectories. As shown in Table 4.1, P varies rather significantly between 0 and 1 for the 17 binding-site cationic residues discussed by Record and co-workers.¹¹⁵ Nevertheless, the majority of these residues have formed salt bridges within 25–50 ns with considerable P values; this is true especially in the no-salt simulation. For example, if we (arbitrarily) choose $P = 0.1$ as the cutoff, 12 out of the 17 binding-site cationic residues form salt bridges in the no-salt simulation. This is quite remarkable since some of the cationic residues are rather far from any anionic residue in the starting (IHF–DNA complex) structure; the most striking example is R56 β , which is 12.4 \AA from any anionic residue in the initial structure but has a significant P value of ~ 0.3 in three independent trajectories. Some salt bridges form quickly and remain stable throughout the simulation; for example, K20 α , R55 α , K75 β , and R87 β all have P values higher than 0.90 in at least one of the three independent trajectories (Figure 4.4). Out of the 17 binding site cationic residues, 5 of them (K45 α , K57 α , R60 α , R59 β and K81 β) do not lead to significant salt bridge formation ($P < 0.01$) during any of the 25–50 ns of simulations (Figure 4.5); they are all rather far from anionic residues in the initial structure ($r_{\text{min-NO}} > 7.5 \text{ \AA}$); thus, salt bridge formation likely implicates structural transitions at longer time scales (for their location in

IHF, see Figure 11b). Nevertheless, even some of these residues come rather close to form stable salt-bridges during the simulations (e.g., see Figure 4.5 for R60 α , for which $r_{\text{min-NO}}$ decreases from ~ 14 to ~ 4 Å). In short, the simulations clearly illustrate that, in the absence of salt, a majority of the cationic residues in the DNA binding region have significant propensity to form salt bridges in the absence of DNA.

4.4.2.3 Salt bridge dynamics for the other 19 cationic residues

Among 19 other cationic residues, which are further away from the DNA binding site in the IHF–DNA complex structure, 11 of them are engaged in salt bridge interactions in the IHF–DNA complex (i.e., $r_{\text{min-NO}} < 3.3$ Å); all these, except K20 β (see below), have high P values throughout the simulation. Among the rest, 5 of them (K15 α , R21 α , R77 α , K97 α , and K69 β in Figure 4.7) also have significant P values (Table 2) although they are not engaged in salt bridges in the IHF–DNA complex. Therefore, this simulation suggests that the disruption of salt bridges involving these cationic residues may also be coupled to the DNA binding process and contribute to the unusual thermodynamic features of IHF–DNA binding. These residues were not considered by Record and co-workers because they are more than 6 Å away from the phosphoryl oxygen atoms of DNA in the crystal complex structure.¹¹⁴ Because electrostatic interactions are relatively long-ranged, it is not unreasonable that DNA binding can perturb interactions beyond the immediate binding region. On the other hand, to firmly support the involvement of these cationic residues, one needs to verify that these cationic

residues do not engage in salt bridge interactions in an MD simulation of the IHF–DNA complex, which is beyond the scope of this work.

As mentioned above, K20 β is somewhat unusual in that it forms salt bridges in the IHF–DNA complex structure but these salt bridges get disrupted completely in the absence of DNA in all three independent trajectories (see Table 2 and Figure 4.10). This behavior is strikingly different from that of the other 35 cationic residues and motivates further structural analysis of this residue. The local environment of K20 β at different stages of the simulation is shown in Fig.6: in the initial structure, K20 β forms bifurcated salt bridges with E23 β and D24 β ; in the absence of DNA, as shown by a snapshot at 22.4 ns in the no-salt simulation (high-salt simulation shows similar behavior) in Figure 4.12b, these two salt bridges are broken, and E23 β and D24 β form salt bridges with two of the 17 binding site cationic residues, K3 β and K27 β . Therefore, in addition to the disruption of salt bridges, there is also salt bridge switching (coupled disruption and formation) involved in the DNA binding process.

4.4.2.4 Effects of KCl concentration on salt bridge formation

To explore the effect of KCl on salt bridge formation, we compare P for all 36 cationic residues under no-salt and high-salt conditions; because only three trajectories are run for each salt concentration, we show the P values from these simulations as separate data points in Fig. 5a rather than attempting to compute standard deviations. As shown in Figure 4.11a, for most residues the effect of KCl concentration is rather minor. The exception is for four

cationic residues in the DNA binding region: R76 α , K88 α , R56 β , and R87 β . These four residues (shown in bold in Table 1 and in yellow in Figure 4.11b) have considerable P values under no-salt condition but essentially a zero P value with 350 mM KCl. A common feature for these four residues is that they are relatively far from anionic residues in the starting structure (Figure 4.4 and 4.6). The shortest $r_{\text{min-NO}}$ is for R87 β , which is 5.9 Å. As shown in Figure 4.6 for R56 β , although $r_{\text{min-NO}}$ is seen to decrease substantially from the initial (crystal) value of 12.4 Å to salt-bridge range (≤ 3.3 Å) in the no-salt simulation, the distance rarely decreases to below 5 Å in the high-salt simulation. Therefore, the overall trend is that KCl has a significant impact on salt bridge formation only if the charged residues are initially far away from each other. This trend makes physical sense since the screening effect associated with salt ions only plays a significant role at long range. At short distances (compared to the size of solvent), electrostatic screening is not expected to be important. For example, the computational study of Elcock and co-workers on the association of acetate and methylammonium (model compounds for salt bridges) found that the free energy minimum that corresponds to the dehydrated salt bridge state is not diminished even up to 2 M salt.¹²³ As the salt concentration increases from 0 to 0.3 M (similar to the high-salt condition here), the stability of the dehydrated salt bridge is reduced by only 0.2 kcal/mol.

These analyses suggest that even at 350 mM KCl, a significant fraction of salt bridges in the unbound form of IHF is expected to be stable (8 out of 17 residues have P_{salt} values larger than 0.1 in at least one 25–50 ns trajectory). This conclusion seems to be inconsistent with the proposal of Record and co-workers that salt bridges are unstable at 350 mM K^+ and hence that

there is no disruption of salt bridges coupled to DNA binding. This second hypothesis was proposed to explain the experimental observation that ΔH_{sp}° for specific binding increases (becomes less negative) significantly from -56.1 kcal/mol at 60 mM K^{+} to -10.8 kcal/mol at 350 mM K^{+} at 40 °C. More recent analyses,¹²⁴ however, found that a significant portion of the large salt dependence is due to the Hofmeister effect associated with Cl^{-} ; extrapolations of results in different salt solutions (KCl, KF, and KGlu) showed that, at low salt concentration, the binding enthalpy is essentially independent of the salt concentration. Nevertheless, it is of interest to discuss other factors that can potentially contribute to the salt dependence of binding thermodynamics in light of the current simulations. For example, since our simulation results indicate that the disruption of multiple salt bridges is still likely involved in DNA binding at even 350 mM K^{+} , we suspect that the increase of ΔH_{sp}° is due, at least in part, to the increase of the enthalpy change of disrupting a salt bridge (ΔH_d) with respect to the increase of K^{+} concentration. This can be understood by comparing the processes of salt bridge disruption at no-salt and high-salt conditions. The enthalpy change for salt bridge disruption at the no-salt condition ($\Delta H_d^{no-salt}$) is negative because of the increase in hydration enthalpy when two charged species are separated.¹⁴⁸ At higher salt concentration, however, the disruption of a salt bridge is coupled to the formation of two side-chain-counterion interaction pairs. As a result, the enthalpy change (ΔH_d^{salt}) should be $\Delta H_d^{no-salt}$ plus the enthalpy change of forming two side-chain-counterion pairs, which is positive, and therefore, ΔH_d^{salt} should be larger (less negative) than $\Delta H_d^{no-salt}$; at a qualitative level, this effect is embedded with the calculations for the enthalpy change for $K^{+}-Cl^{-}$ ion pair dissociation at different

concentrations. Whether this effect is important at a quantitative scale remains to be determined because the estimated impact for K^+-Cl^- ion pair dissociation is fairly modest in magnitude. Moreover, this contribution can be offset by similar effects, but of the opposite sign, associated with the formation of ionic interactions between the cationic residues in IHF and phosphoryl groups in DNA.

Clearly, the association of KCl is entropically driven ($\Delta S > 0$) while enthalpically unfavorable ($\Delta H > 0$); the magnitude of the enthalpic change decreases as a function of the [KCl], although the effect is fairly modest. Nevertheless, when a large number of salt-bridge interactions are involved, as in the case of protein/DNA interactions, this effect can be significant. For example, the binding enthalpy for IHF–DNA at 20° increases with salt concentration with a slope of 11 ± 2 kcal/(mol•M) for KF and KGlu,¹²² which translates to on the order of 3 kcal/mol at salt concentration of 300 mM; this magnitude is not too different from the cumulative effect from 10–20 salt-bridge interactions as predicted from Table 4.1. In reality, however, we realize that the situation is complex because there is a significant Hofmeister component in the experimentally observed salt dependence, and that the contribution that we discuss here can be offset by similar effects, but of the opposite sign, associated with the formation of ionic interactions between the cationic residues in IHF and phosphates in DNA.

4.4.3 *Impact on the Prediction of DNA Binding Sites*

As mentioned in the introductory section, an important goal of this study is to explore how sampling salt bridge dynamics impacts the prediction of DNA binding sites on proteins. The goal is motivated by the consideration that salt bridge formation or disruption is expected to significantly modulate the system electrostatics, which play a major role in many DNA binding site prediction algorithms.^{145,144,149,150,151} Indeed, many such algorithms have been tested or trained using the structures of protein–DNA complexes (with the DNA excised). If there is significant structural difference between the unbound and bound conformations of the protein, such as the formation or disruption of a large number of salt bridges, the electrostatic properties may differ significantly. As a result, an algorithm trained using bound state structures may not be effective because realistic applications will require using the unbound state as input.

To illustrate the change of surface electrostatic potential in IHF due to salt bridge dynamics, we calculate the differential electrostatic potential between IHF adopting the conformation in the IHF–DNA complex (PDB code 1IHF)¹¹⁴ and a snapshot from the no-salt simulation in which the maximum number (12 of 17) of binding-site cationic residues have formed salt bridges (see Figure 4.13). For the red regions in Figure 4.13, the residue-averaged electrostatic potential difference ($\Delta\phi_{\text{res}}$) is more than $5 \text{ kcal}\cdot\text{mol}^{-1}\cdot\text{e}^{-1}$; $\Delta\phi_{\text{res}}$ is less than $5 \text{ kcal}\cdot\text{mol}^{-1}\cdot\text{e}^{-1}$ for the blue regions, whereas it is between -5 and $5 \text{ kcal}\cdot\text{mol}^{-1}\cdot\text{e}^{-1}$ for the white regions. It is clear that for most of the DNA binding interface, the electrostatic potential is

decreased by more than $5 \text{ kcal} \cdot \text{mol}^{-1} \cdot \text{e}^{-1}$ as the IHF structure relaxes away from the conformation in the IHF–DNA complex. We emphasize here that the structural variations sampled in this study are limited to the time scale of 25–50 ns; with the realistic structure of the apo state IHF, the difference in the structural and electrostatic properties can be even greater.

The key question is whether such change in the surface electrostatic potential has a significant impact on the performance of structure-based algorithms for DNA binding site prediction. As discussed in the Computational Methods section, we tested this using two popular structure-based web servers. The first server is patch plus finder (PPF),¹⁴³ which finds the largest continuous patch with positive electrostatic potential on the protein surface.¹⁵¹ Using the IHF structure in the IHF–DNA complex as input, the predicted patch by PPF (see Figure 4.14a) contained 63 residues and coincided with the authentic DNA binding interface. Using the snapshot with altered salt bridge patterns as the input structure, however, the predicted patch (see Figure 4.14b) contained 35 residues and spanned only half of the arm domain.

The second server we tested was Preds,^{145,144} which makes prediction on the basis of not only surface electrostatic potential but also molecular shape features. An output of Preds is a statistical score, P_{score} , and the input protein is predicted to be a DNA binding protein if P_{score} is higher than 0.12. Using the IHF structure in the IHF–DNA complex as input, the predicted P_{score} was 0.27; the score becomes substantially lower (0.17) when the snapshot from simulation was used. Another output of Preds is the predicted binding sites, which are shown in Figure 4.14c and 4.14d with different IHF structures as input; the difference is relatively

small, and the predicted binding site is reduced from 90 to 73 residues when the snapshot from MD simulation is used instead of the IHF structure in the IHF–DNA complex.

Therefore, the prediction of DNA binding site appears to be more robust when electrostatic properties are augmented by geometrical considerations.

4.5 Conclusions

Protein–DNA binding processes likely involve many structural transitions at both domain and side-chain levels, which are not straightforward to capture using experiments alone. In this study, motivated by the proposal of Record and co-workers in recent thermodynamic studies of specific DNA binding to IHF,¹¹⁵ we have focused on the behavior of charged residues in IHF using explicit solvent molecular dynamics simulations. Even at the somewhat limited time scale of 25–50 ns, we have observed rather rich behaviors. Of the 17 cationic residues noted by Record and co-workers, most are engaged in salt-bridge interactions for a significant portion of the trajectories, especially under the no-salt condition. This observation suggests that, from a structural point of view, their proposal that IHF–DNA binding is coupled with the disruption of pre-existing salt-bridges in apo IHF is plausible. However, switching of salt bridge pairs, i.e. the simultaneous disruption and formation of salt bridges, that involve nonbinding site cationic residues has also been observed during the MD simulations. Therefore, the unusual thermodynamic characters for IHF–DNA binding likely arise from the interplay between fairly complex dynamics of charged residues both in and beyond the DNA binding site. With regard to the salt effect, the MD simulations suggest that it contributes to

the screening of electrostatic interactions only when salt bridge pairs are far away from each other, consistent with a recent computational study of small molecules that form salt bridges.¹²³ Therefore, the large dependence of the IHF–DNA binding enthalpy on salt concentration may not be due to a significant decrease in the number of stable salt bridges in apo IHF at high salt concentration; this is qualitatively consistent with more recent analysis,¹²⁴ which found that the salt dependence of binding enthalpy is largely a Hofmeister effect.

Our simulation study further highlights that the electrostatic properties of DNA-binding proteins can be rather different in the apo and DNA bound states. This has important implications to the design of methods for predicting DNA binding sites in proteins. As we have illustrated using two examples, it appears to be essential to explicitly consider sampling salt-bridge dynamics when evaluating electrostatic properties or to supplement electrostatic properties with geometrical criteria based on structural complementarity.

Acknowledgements. We acknowledge Professor Tom Record for encouraging us to examine the problem and for stimulating discussions. Computational resources from the National Center for Supercomputing Applications at the University of Illinois and the Centre for High Throughput Computing (CHTC) at UW-Madison are greatly appreciated. The authors thank Professor Tom Record for encouraging us to work on the subject and for stimulating discussions. The research has been supported by the National Institutes of Health (R01-GM071428 to Q.C. and R01-CA073808 to R.T.R.).

Table 1: r_{init} , $P_{\text{no-salt}}$, and P_{salt} Values for the 17 Binding-Site Cationic Residues^a

residue	r_{init} (Å)	$P_{\text{no-salt}}$	P_{salt}	residue	r_{init} (Å)	$P_{\text{no-salt}}$	P_{salt}
K20α	3.9	0.99	0.95	K3β	7.4	0.10	0.12
		0.96/0.97	0.98/0.97			0.19/0.13	0.07/0.00
K24α	7.0	0.22	0.31	K27β	3.7	0.80	0.42
		0.05/0.14	0.16/0.00			0.86/0.59	0.53/0.61
K45α	7.6	0.00	0.00	R56β	12.4	0.28	0.00
		0.00/0.00	0.00/0.00			0.33/0.32	0.00/0.00
R55α	5.9	0.99	0.83	R59β	9.3	0.00	0.00
		0.89/0.83	0.63/0.03			0.00/0.02	0.00/0.00
K57α	10.0	0.00	0.00	K75β	5.2	0.60	0.89
		0.00/0.00	0.00/0.00			0.95/0.65	0.89/0.87
R60α	12.0	0.02	0.00	K81β	9.5	0.00	0.00
		0.00/0.00	0.00/0.00			0.00/0.00	0.00/0.00
R63α	4.4	0.42	0.68	R87β	5.9	0.90	0.00
		0.38/0.93	0.90/0.66			0.55/0.99	0.00/0.00
R76α	6.6	0.77	0.00				
		0.01/0.00	0.00/0.00				
R82α	4.4	0.63	0.70				
		0.57/0.60	0.70/0.75				
K88α	9.3	0.55	0.00				
		0.03/0.16	0.00/0.00				

Table 4.1 Summary of salt-bridge activity for binding-site cationic residues

r_{init} (in angstroms) is the minimal distance between N in a cationic residue and O in all anionic residues in IHF in the IHF–DNA complex (PDB code 1IHF). $P_{\text{no-salt}}$ and P_{salt} are the probabilities of salt bridge formation in no-salt and high-salt simulations, respectively. Residues shown in bold exhibit the most significant difference between $P_{\text{no-salt}}$ and P_{salt} (also shown as circled red dots in Figure 4.11). For each residue, the first row gives the value from a 50 ns simulation, while the second row gives the value from two other independent 25 ns simulations. Summary of salt-bridge activity for binding-site cationic residues

Table 2: r_{init} , $P_{\text{no-salt}}$, and P_{salt} Values for the 19 Other Cationic Residues^a

residue	r_{init} (Å)	$P_{\text{no-salt}}$	P_{salt}	residue	r_{init} (Å)	$P_{\text{no-salt}}$	P_{salt}
K5α	3.0	0.87	0.97	R9β	2.9	0.76	0.96
		0.99/0.96	1.00/0.99			0.97/0.97	0.94/0.91
K15α	4.6	0.86	0.92	K20β	3.0	0.03	0.06
		0.96/0.91	0.89/0.86			0.02/0.15	0.04/0.02
R21α	5.4	0.43	0.54	R42β	3.0	0.76	0.88
		0.66/0.43	0.58/0.31			0.70/0.52	0.32/0.24
R35α	2.9	1.00	1.00	R46β	3.0	0.28	0.34
		1.00/1.00	1.00/1.00			0.11/0.25	0.39/0.21
R36α	3.3	0.88	0.65	R62β	6.7	0.00	0.39
		0.79/0.79	1.00/0.81			0.00/0.00	0.00/0.00
K66α	12.4	0.08	0.00	K65β	10.1	0.00	0.00
		0.00/0.00	0.00/0.00			0.00/0.00	0.00/0.00
R77α	3.6	0.83	0.94	K69β	6.6	0.36	0.26
		0.81/0.58	0.89/0.96			0.32/0.51	0.14/0.20
K86α	7.2	0.02	0.05	K84β	3.0	0.70	0.31
		0.10/0.02	0.14/0.00			0.40/0.81	0.26/0.25
R90α	3.0	1.00	1.00	R89β	2.8	0.99	1.00
		0.98/0.99	1.00/1.00			0.95/1.00	1.00/1.00
K97α	4.5	0.55	0.56				
		0.46/0.57	0.56/0.42				

Table 4.2 Summary of salt bridge activity for non-binding site cationic activity

r_{init} (in angstroms) is the minimal distance between N in a cationic residue and O in all anionic residues in IHF in the IHF–DNA complex (PDB code 1IHF). $P_{\text{no-salt}}$ and P_{salt} are the probabilities of salt bridge formation in no-salt and high-salt simulations, respectively. Residues shown in bold exhibit the most significant difference between $P_{\text{no-salt}}$ and P_{salt} (also shown as circled red dots in Figure 4.11). For each residue, the first row gives the value from a 50 ns simulation, while the second row gives the value from two other independent 25 ns simulations.

[KCl]	ΔG (kcal/mol)	ΔS (kcal/mol \cdot K $^{-1}$)	ΔH (kcal/mol)
0.2 M	-2.09	0.0087	0.50
0.5 M	-1.88	0.0075	0.37
0.8 M	-1.75	0.0071	0.36

Table 4.3 Dependence of thermodynamic properties of K–Cl association on [KCl]
 The potential mean force was inverted from the radial distribution function.
 The enthalpic and entropic components were calculated based on the finite
 difference between simulations at three temperatures (280 K, 300 K, 320 K).

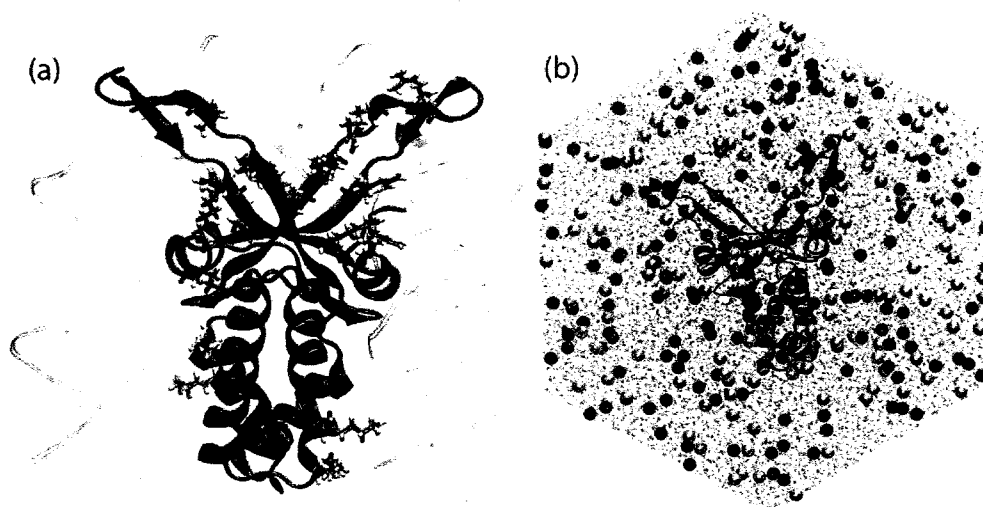


Figure 4.1 Structure of IHF.

(a) The crystal structure of IHF–DNA complex (pdb 1IHF) IHF is shown in New Cartoon and in purple while DNA is shown in Ribbons and in yellow. The 17 proposed cationic residues by Record and co-workers (not including two His residues, H54 and H79) are shown in Licorice. (b) A snapshot from MD simulations of apo-IHF at 350 mM KCl. The starting structure is obtained from the crystal structure of the IHF–DNA complex (PDB code 1IHF) from which the DNA is removed. IHF is shown in the Cartoon scheme and in purple; oxygen atoms of water molecules are shown as points and in iceblue. K⁺ and Cl⁻ ions are shown as spheres and in yellow and green, respectively. The figures are made using VMD.¹⁵²

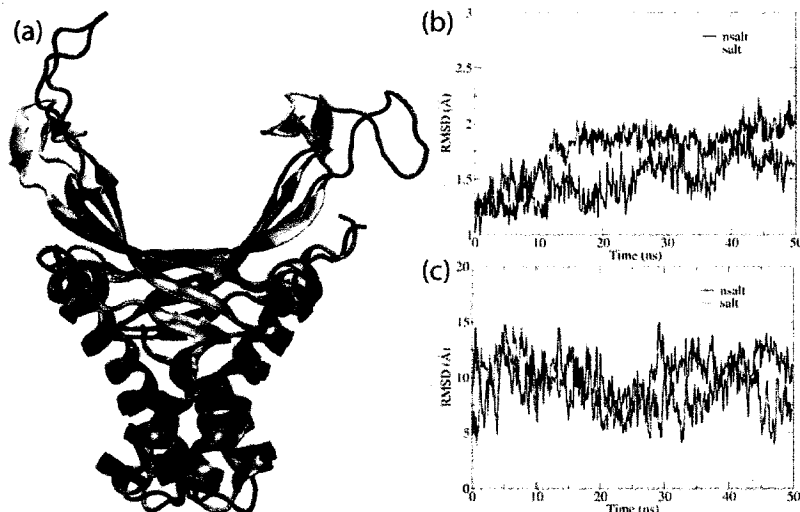


Figure 4.2 Conformational transitions in IHF observed within 50 ns MD simulations
 (a) Overlap of IHF conformation in the IHF–DNA complex (PDB entry 1IHF) and a random snapshot by the end of the no-salt MD simulation. The backbone atoms of the core domain were used as the best-fit region. The core and arm domains of the crystal conformation are colored green and yellow, respectively, while those in the MD snapshot are colored grey and purple, respectively. (b and c) the RMSD of backbone atoms of (b) the core domain and (c) the arm domain along MD trajectories with respect to the crystal conformation of IHF with the backbone atoms of the core domain as the best-fitting region.

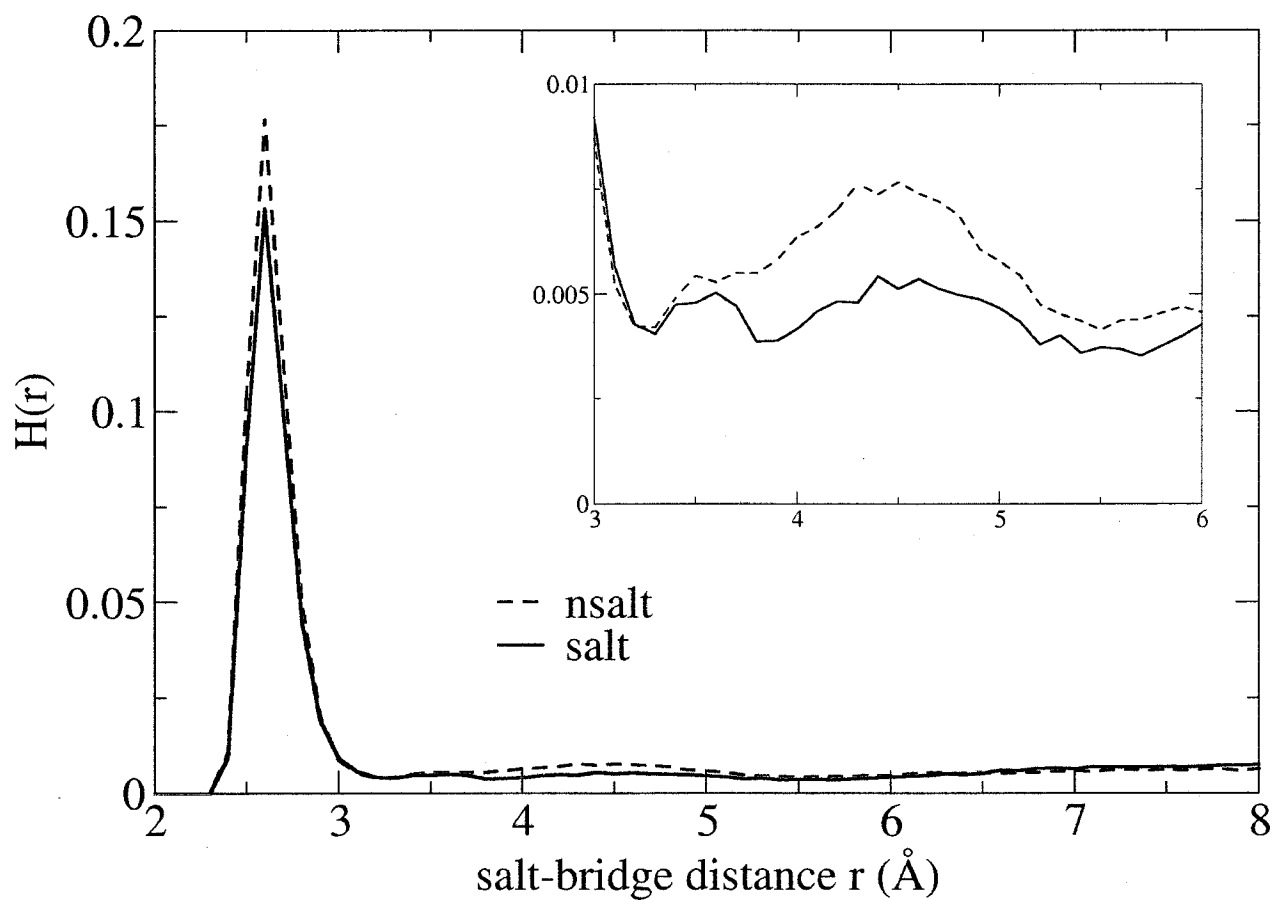


Figure 4.3 Normalized histogram $H(r)$ of salt bridge distance.

$r_{\text{min-NO}}$ is the minimal distance between N in a cationic residue and O in all anionic residues for all 36 cationic residues collected from no-salt and high-salt simulations. The inset shows the small peak between 3 and 6 Å.

Figure 4.4 Behaviors of stable salt bridges involving binding-site cationic residues during MD simulations

These illustrate no-salt (0 M KCl, top panel for each residue) and high-salt (350 mM KCl, bottom panel for each residue) conditions; results for other two independent 25 ns simulations for each salt concentration are qualitatively similar and therefore not shown. The salt-bridge distance r for a specific cationic residue is the minimal distance between its side chain N atom and side chain O atoms in all anionic residues; r_{init} indicates the value in the crystal structure.

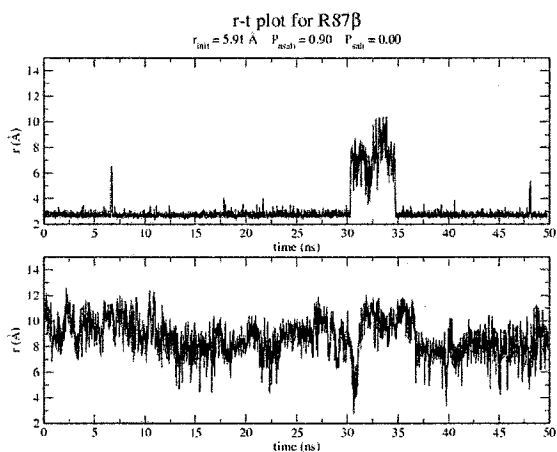
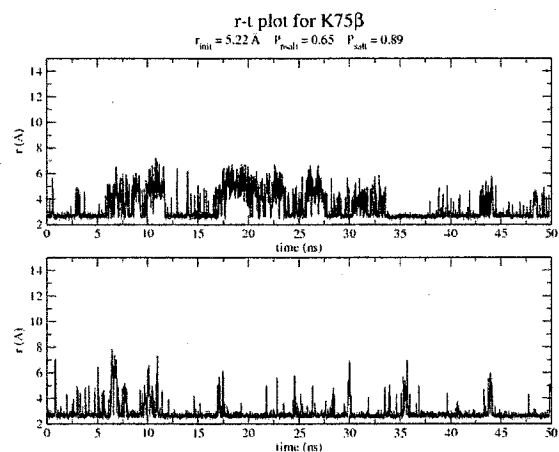
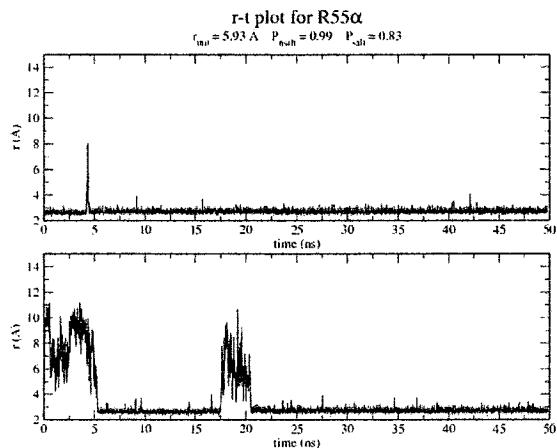
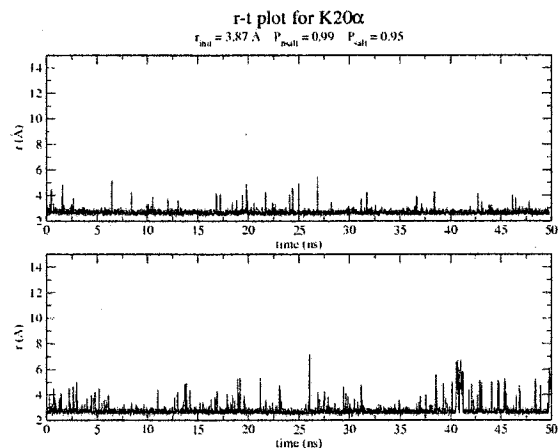


Figure 4.5 Behaviors of binding-site cationic residues without significant salt-bridge formation during MD simulations

These illustrate no-salt (0 M KCl, top panel for each residue) and high-salt (350 mM KCl, bottom panel for each residue) conditions; results for other two independent 25 ns simulations for each salt concentration are qualitatively similar and therefore not shown. The salt-bridge distance r for a specific cationic residue is the minimal distance between its side chain N atom and side chain O atoms in all anionic residues; r_{init} indicates the value in the crystal structure.

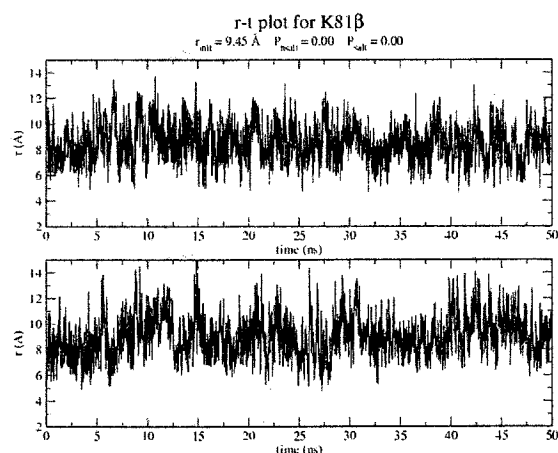
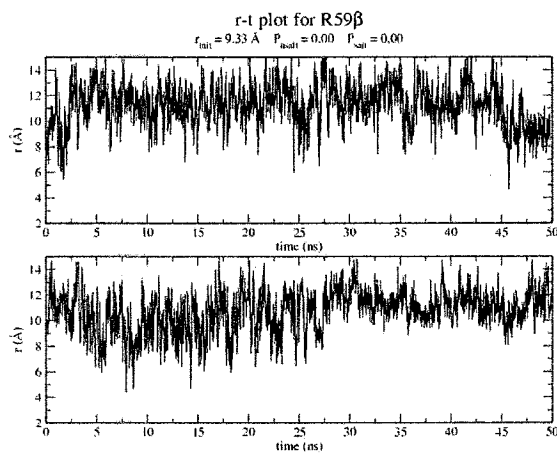
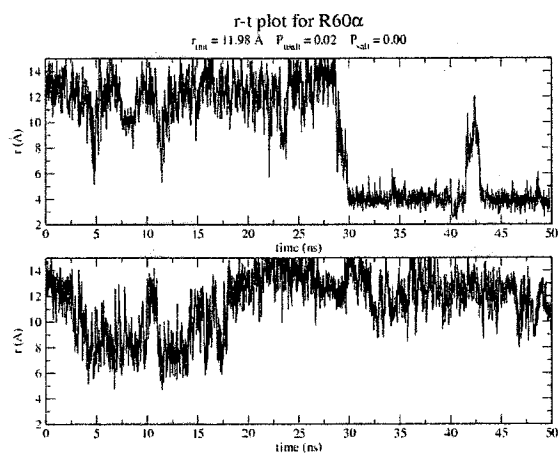
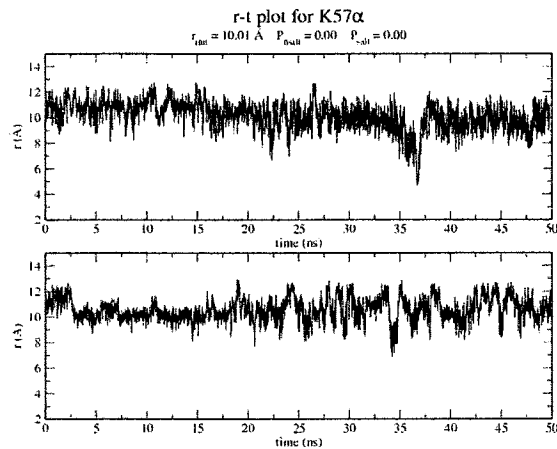
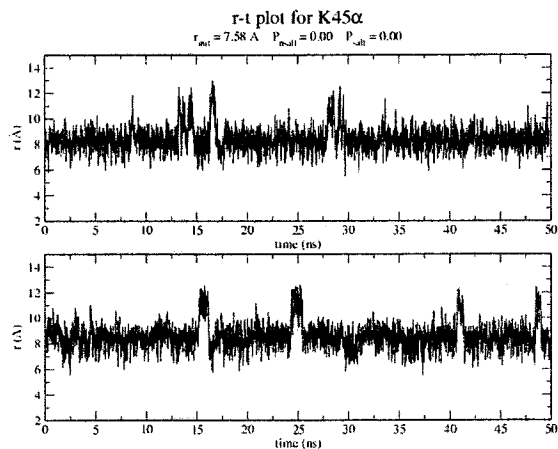
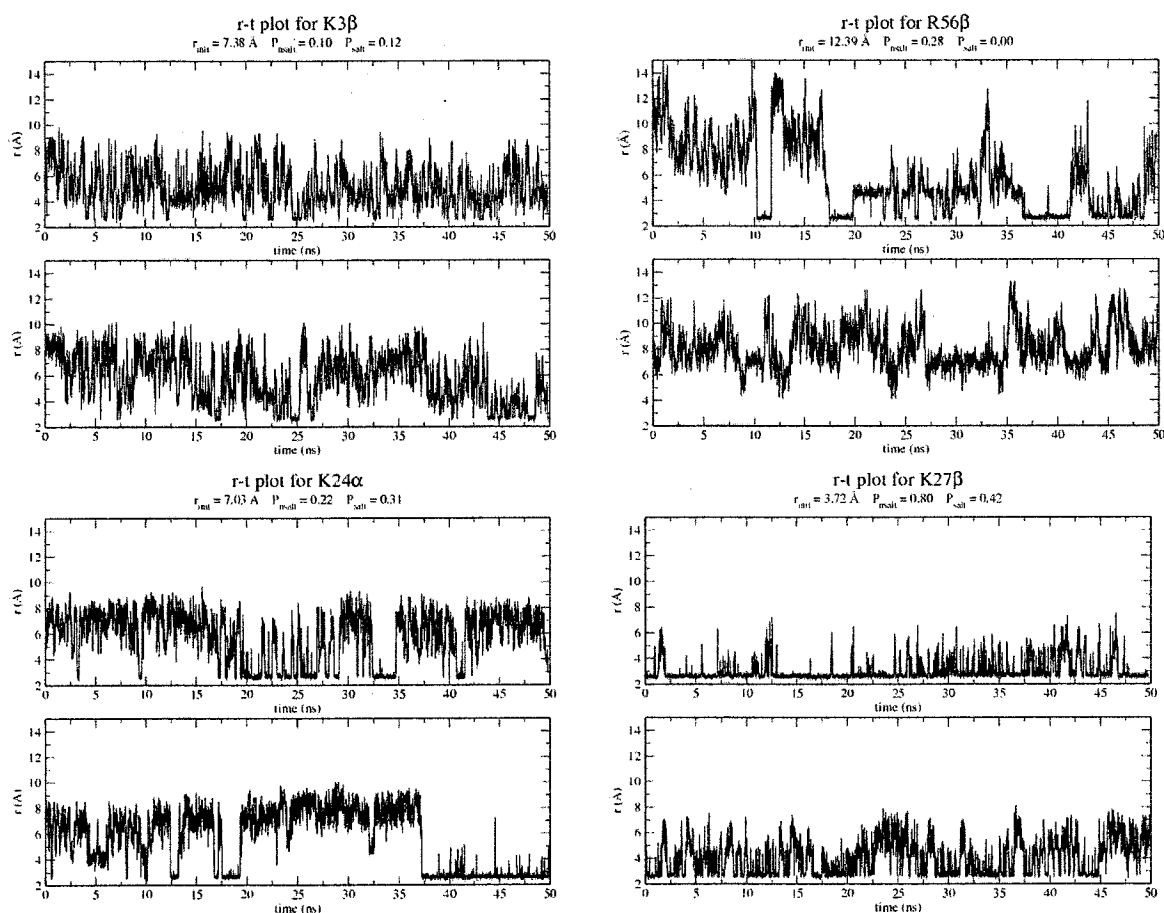


Figure 4.6 Behavior of salt-bridges of binding-site cationic residues in MD simulations

These illustrate no-salt (0 M KCl, top panel for each residue) and high-salt (350 mM KCl, bottom panel for each residue) conditions; results for other two independent 25 ns simulations for each salt concentration are qualitatively similar and therefore not shown. The salt-bridge distance r for a specific cationic residue is the minimal distance between its side chain N atom and side chain O atoms in all anionic residues; r_{init} indicates the value in the crystal structure.



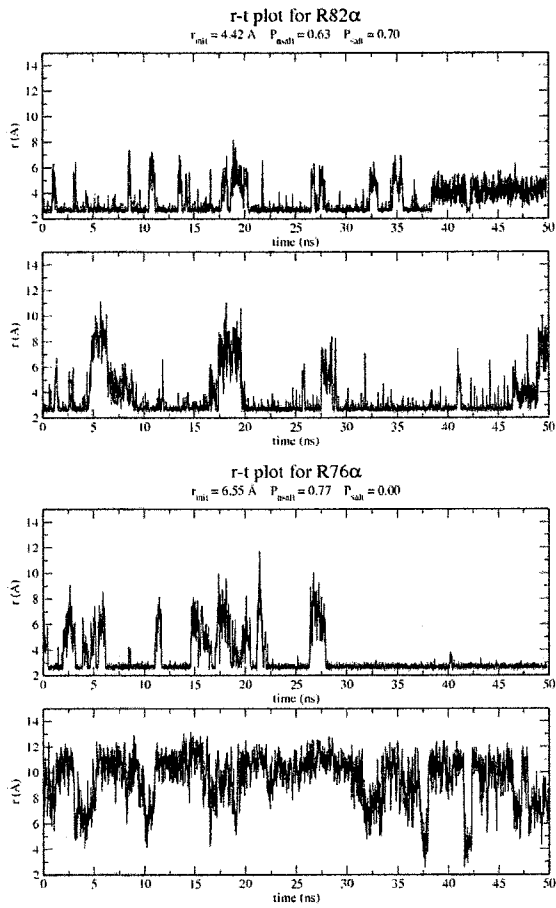
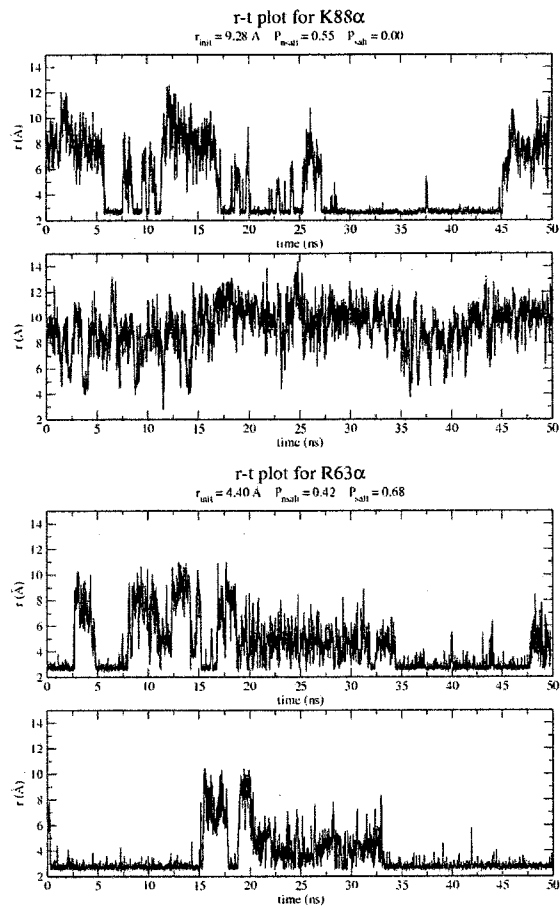


Figure 4.7 Behavior of non-binding site cationic residues with large r_{init} that engage in salt-bridge behavior during MD simulations

These illustrate no-salt (0 M KCl, top panel for each residue) and high-salt (350 mM KCl, bottom panel for each residue) conditions; results for other two independent 25 ns simulations for each salt concentration are qualitatively similar and therefore not shown. The salt-bridge distance r for a specific cationic residue is the minimal distance between its side chain N atom and side chain O atoms in all anionic residues; r_{init} indicates the value in the crystal structure. These residues do not engage in salt bridges in the IHF–DNA complex but spend a significant amount of time engaged in salt bridge interactions during the MD simulations.

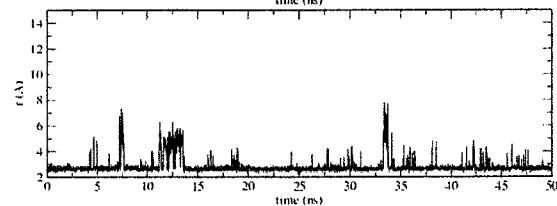
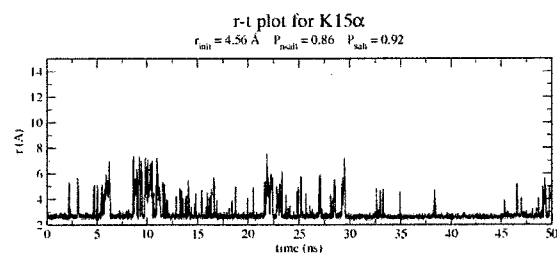
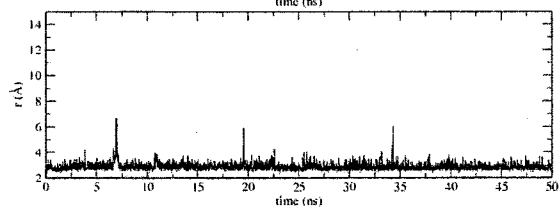
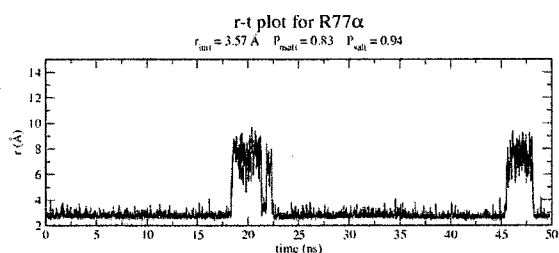
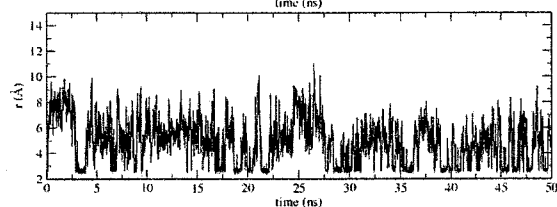
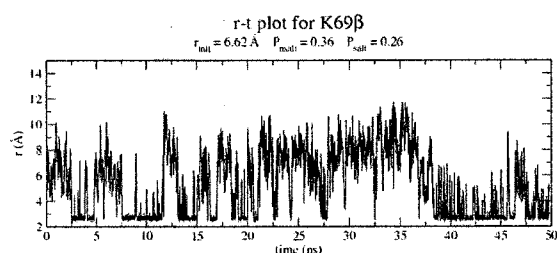
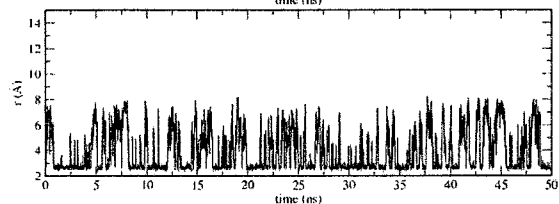
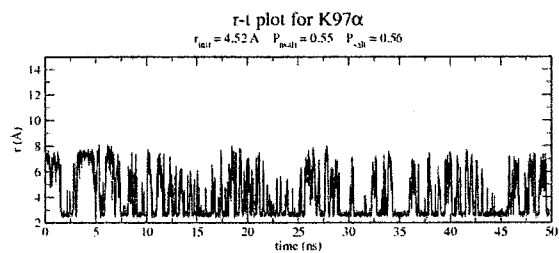
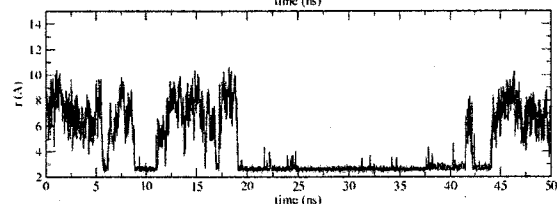
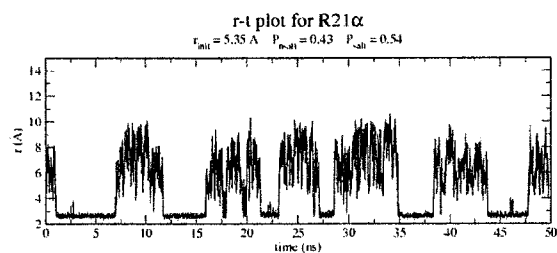
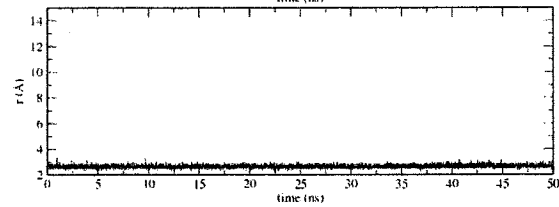
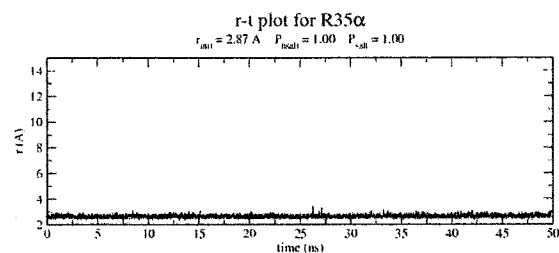
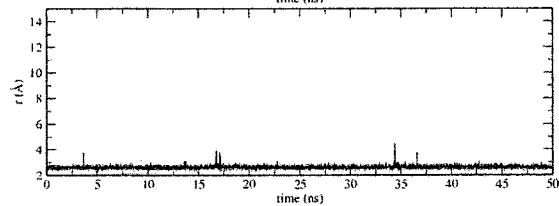
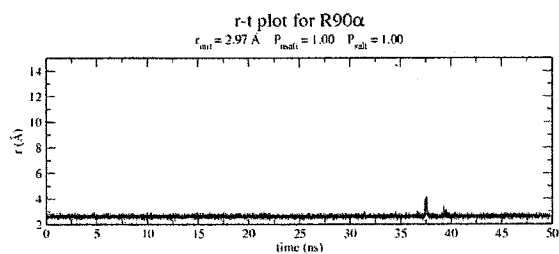
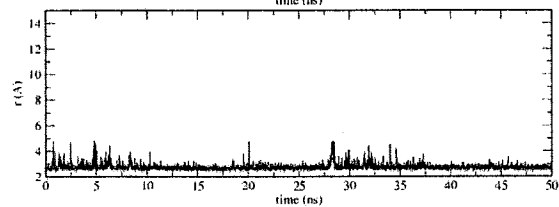
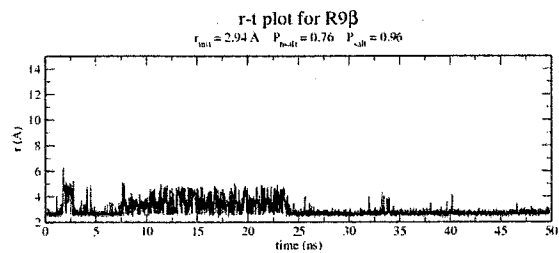
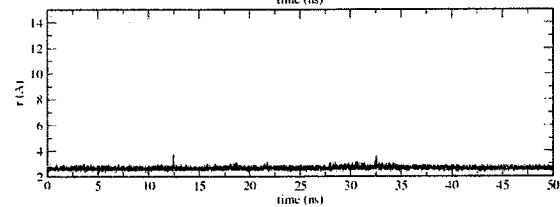
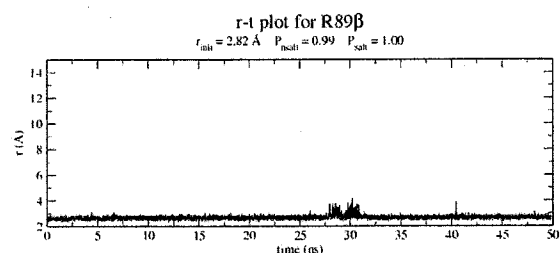
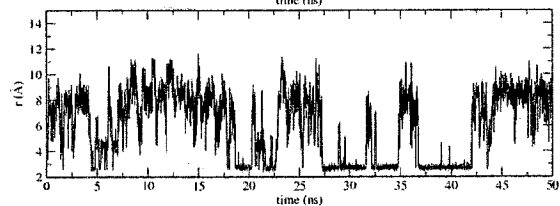
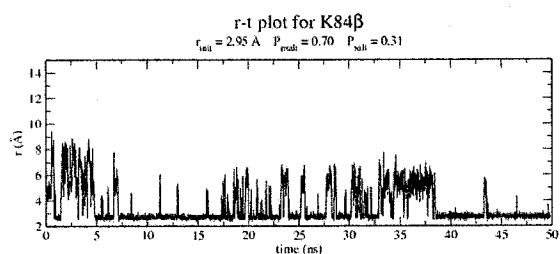
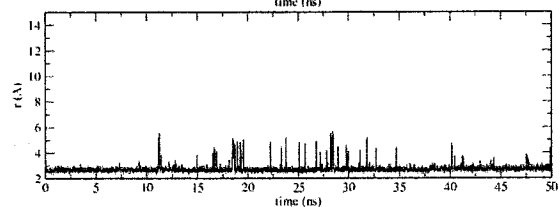
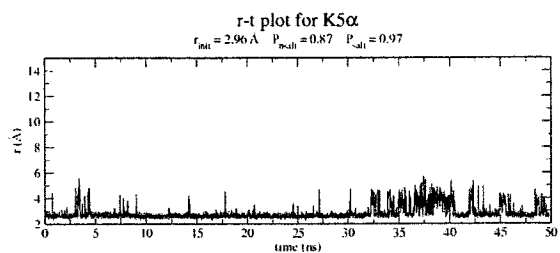


Figure 4.8 Behavior of non-binding-site cationic residues with small r_{init} values that demonstrate formation of salt-bridges during MD simulations

These illustrate no-salt (0 M KCl, top panel for each residue) and high-salt (350 mM KCl, bottom panel for each residue) conditions; results for other two independent 25 ns simulations for each salt concentration are qualitatively similar and therefore not shown. The salt-bridge distance r for a specific cationic residue is the minimal distance between its side chain N atom and side chain O atoms in all anionic residues; r_{init} indicates the value in the crystal structure. These residues engage in salt bridges in the IHF–DNA complex and spend a significant amount of time engaged in salt bridge interactions during the MD simulations.



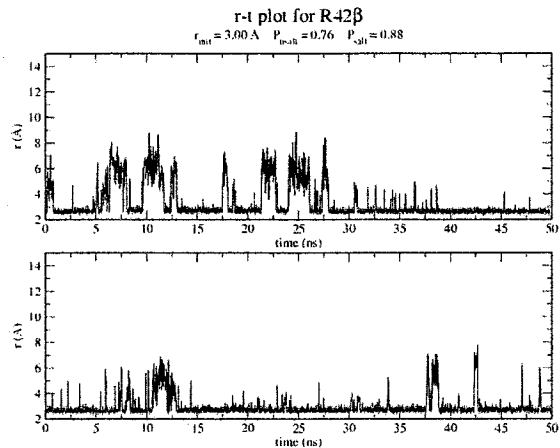
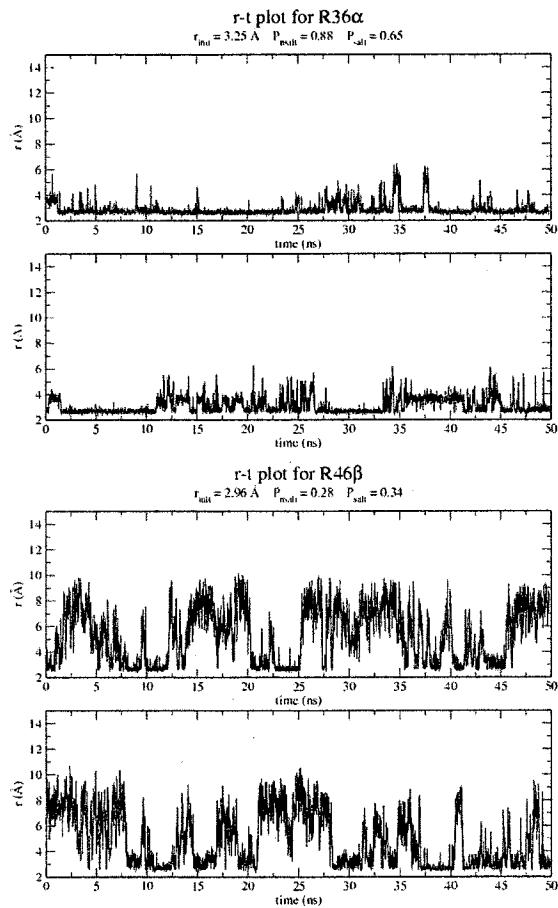


Figure 4.9 Behavior of non-binding site cationic residues with large r_{init} values that do not engage in significant salt-bridge interactions during MD simulations

These illustrate no-salt (0 M KCl, top panel for each residue) and high-salt (350 mM KCl, bottom panel for each residue) conditions; results for other two independent 25 ns simulations for each salt concentration are qualitatively similar and therefore not shown. The salt-bridge distance r for a specific cationic residue is the minimal distance between its side chain N atom and side chain O atoms in all anionic residues; r_{init} indicates the value in the crystal structure.

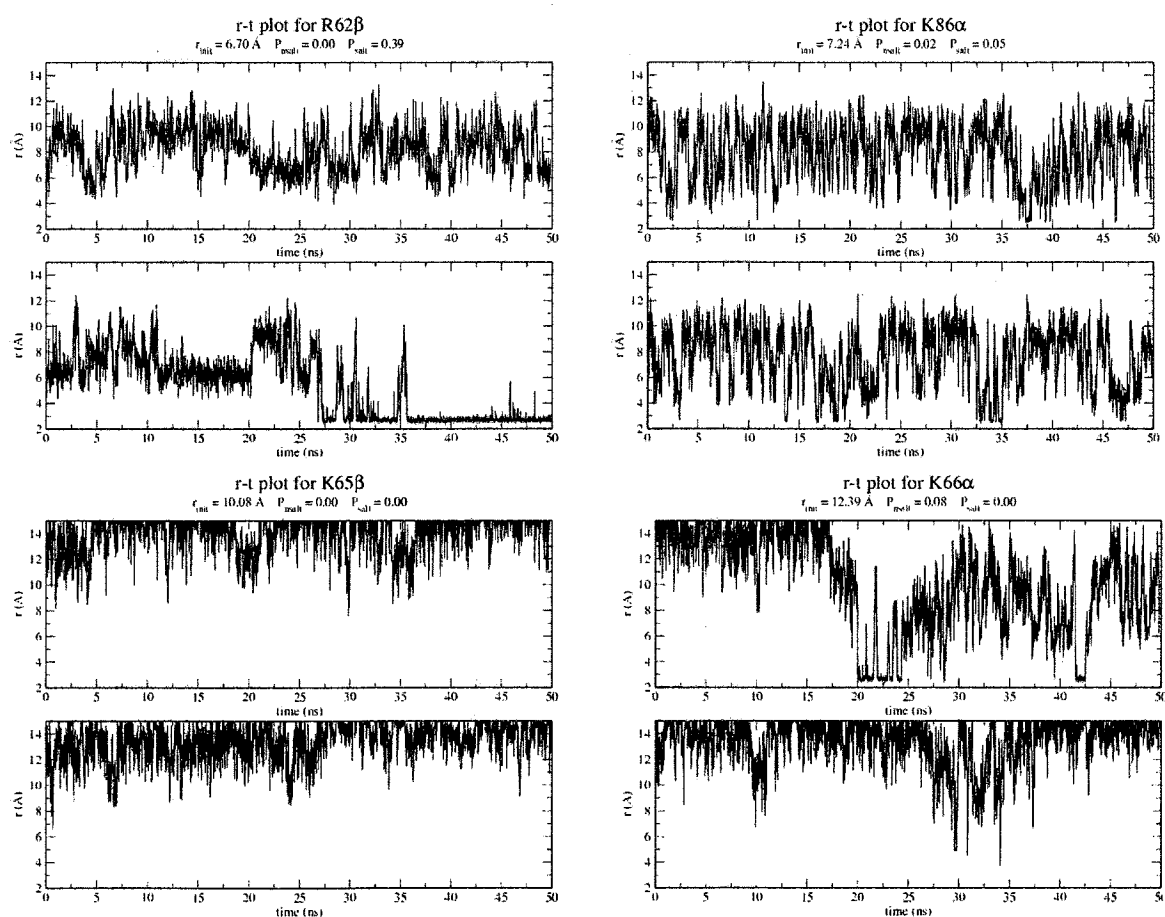


Figure 4.10 Salt-bridge behavior of K20 β , a non-binding site cationic residue, during MD simulations

This illustrates no-salt (0 M KCl, top panel for each residue) and high-salt (350 mM KCl, bottom panel for each residue) conditions; results for other two independent 25 ns simulations for each salt concentration are qualitatively similar and therefore not shown. The salt-bridge distance r for a specific cationic residue is the minimal distance between its side chain N atom and side chain O atoms in all anionic residues; r_{init} indicates the value in the crystal structure. Although this residue forms a salt bridge in the DNAIHF complex, it is rapidly disrupted during MD simulations

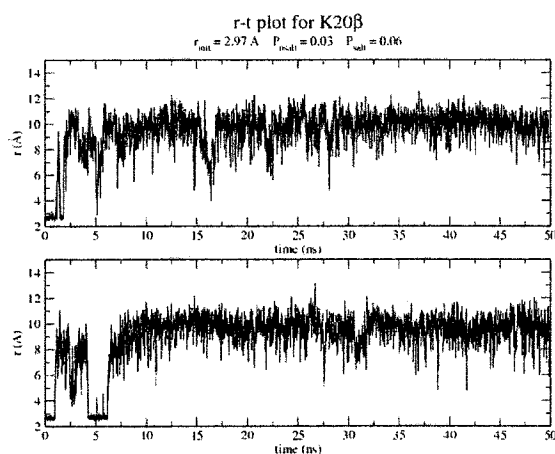
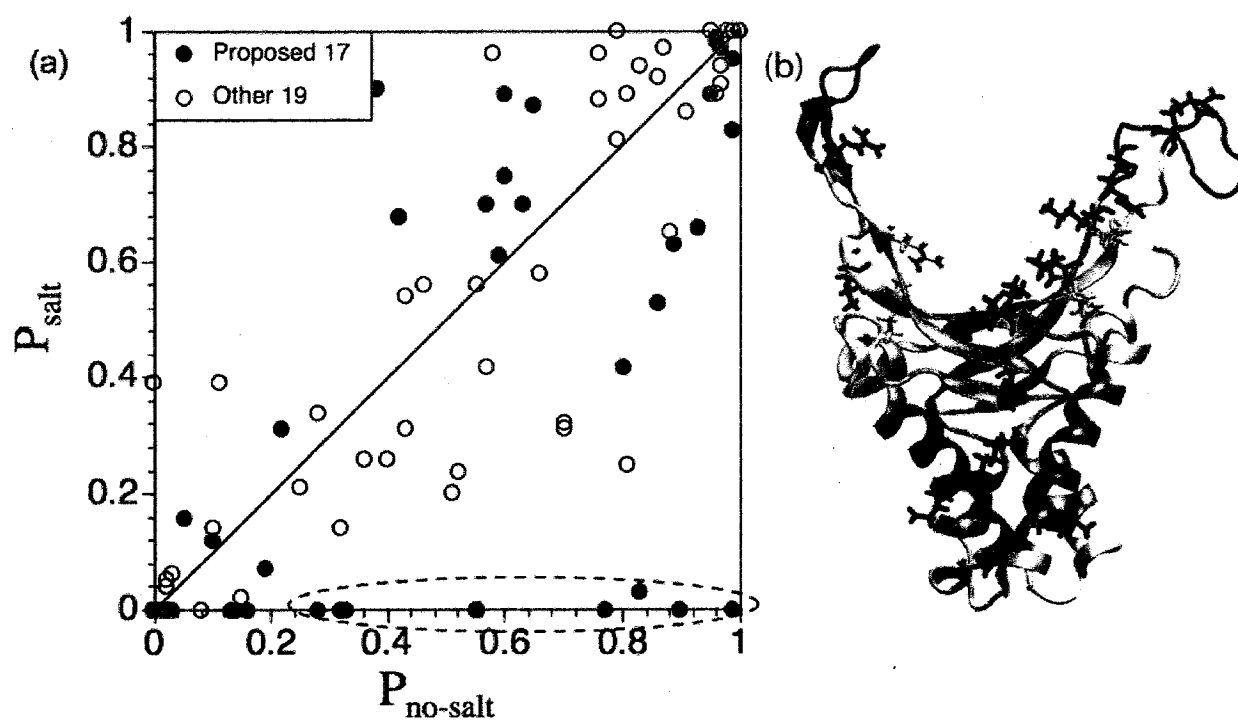


Figure 4.11 Behavior of cationic residues in IHF during MD simulations.

(a) Correlation between $P_{\text{no-salt}}$ and P_{salt} for all 36 cationic residues. The 17 binding-site cationic residues are shown as red dots while the other 19 are shown as open circles; for each residue, results for three independent pairs of simulations are shown as separate data points. The circled red dots indicate residues that exhibit the most significant differences between $P_{\text{no-salt}}$ and P_{salt} (also see Table 1). The $P_{\text{no-salt}} = P_{\text{salt}}$ line is meant to guide the eyes. (b) A random snapshot from no-salt simulation. IHF is shown in New Cartoon and colored according to the RMSF (red indicates high RMSF while blue low RMSF). The 17 binding-site cationic residues are shown in Licorice and in different colors according to their salt-bridge formation probabilities: residues whose $P_{\text{no-salt}}$ and P_{salt} are both greater than 0.10 are shown in red; residues whose $P_{\text{no-salt}}$ and P_{salt} are both lower than 0.10 are shown in blue; residues with high $P_{\text{no-salt}}$ but low P_{salt} (bold in Table 1 and circled in (a)) are shown in yellow.



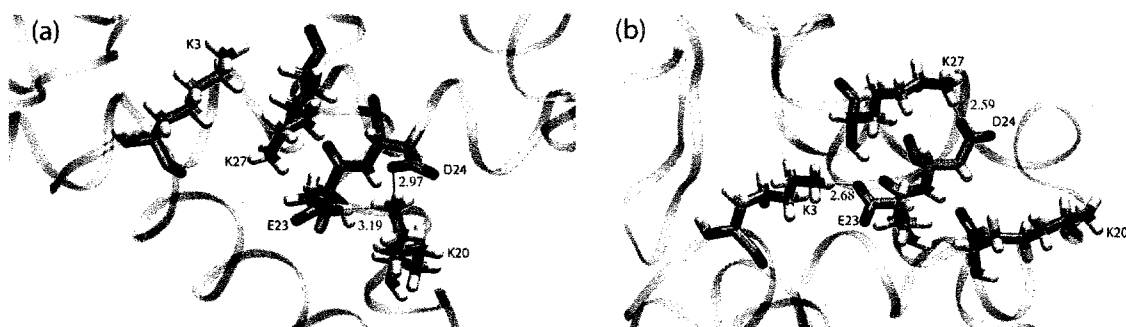


Figure 4.12 The positions of K3, K20, E23, D24, K27 on the β subunit.

(a) the IHF conformation in the IHF-DNA complex (PDB code 1IHF) and (b) a snapshot at 22.4 ns from the no-salt simulation. The five charged residues are shown in licorice scheme while the protein is shown in ribbons. The salt bridge distances ($r_{\text{min-NO}}$, in Å) for salt bridges are also shown. Comparison between (a) and (b) indicates that the salt bridge pattern involving K20 β changes during the simulation.

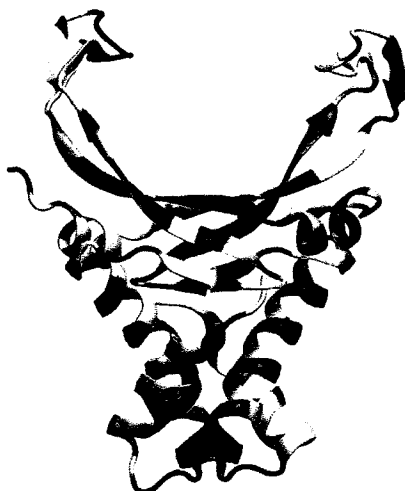


Figure 4.13 Differential residue-averaged electrostatic potential ($\Delta\phi_{\text{res}}$) between the simulated apo structure and the crystal apo structure, mapped onto the crystal apo structure.

$\Delta\phi_{\text{res}}$ is larger than $5 \text{ kcal}\cdot\text{mol}^{-1} \text{ e}^{-1}$, less than $-5 \text{ kcal}\cdot\text{mol}^{-1} \text{ e}^{-1}$ and between -5 and $5 \text{ kcal}\cdot\text{mol}^{-1} \text{ e}^{-1}$ for the blue, red and white regions, respectively.

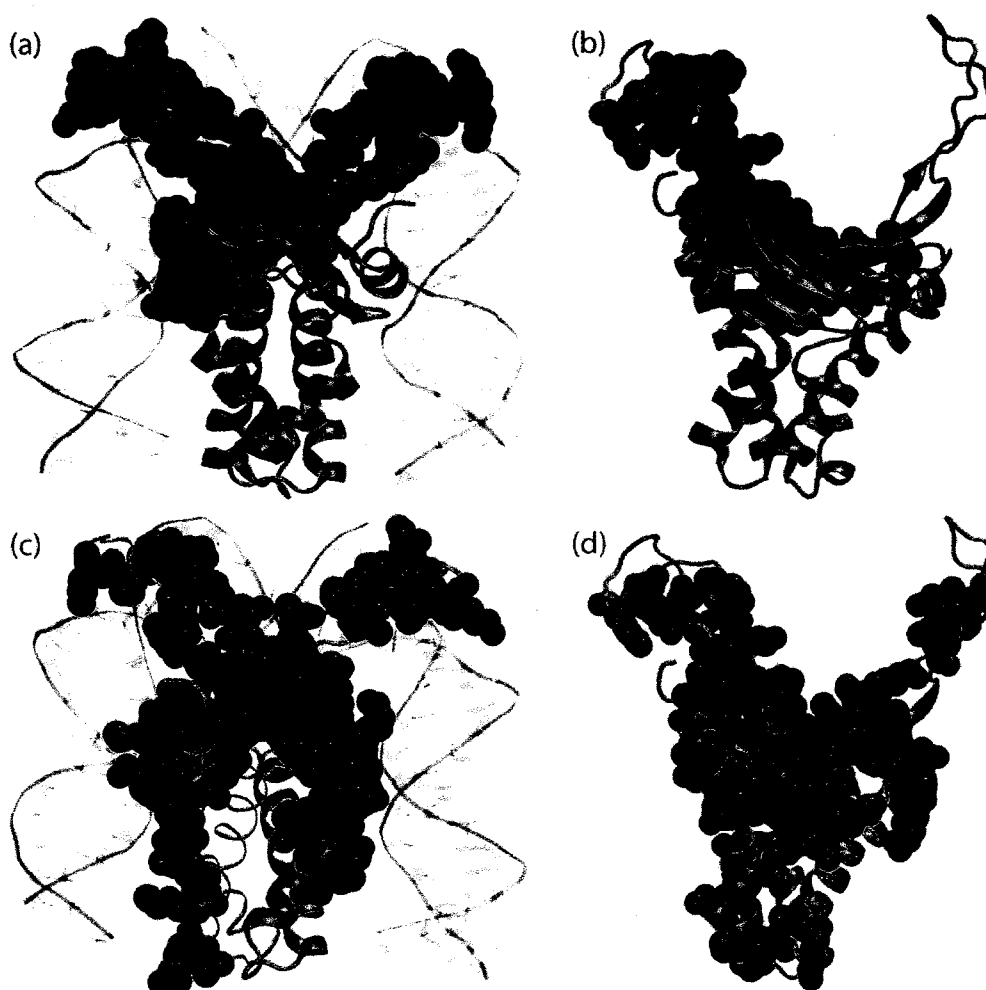


Figure 4.14 Results of DNA binding site prediction using two popular online servers. IHF is shown as a cartoon, and the residues predicted for the binding sites are colored blue in a van der Waals scheme. (a and b) DNA binding sites predicted by PPF for the (a) crystal apo and (b) simulated unbound IHF structures. (c and d) The DNA binding sites predicted by Preds for (c) the crystal apo structure and (d) the simulated unbound structure.

CHAPTER 5

Future Directions

5.1 Cellular Uptake of Pancreatic-type Ribonucleases

Secretory ribonucleases have provided a wealth of knowledge about protein structure and function in the past. Currently, ribonucleases demonstrate great promise as clinical therapies for a variety of pathological conditions. A critical step in the cytotoxic pathway of ribonucleases involves their cellular uptake. Previously, the internalization of these ribonucleases was believed to be due to an electrostatic attraction to the cell surface.^{32,72} Increased positive charge was shown to increase internalization and cytotoxicity, supporting this hypothesis.^{37,29} Increasing positive charge through site-directed mutagenesis or through chemical means may increase electrostatic association but these results have been confounded by specificity for species present on the cell surface. For example, heparan can inhibit the cytotoxicity of polyethylenimine-cationized RNase A, which demonstrates increased cytotoxicity compared to RNase A, via competition with the cell surface.¹⁵³

This thesis focused on using a combination of computational and experimental techniques to increase understanding about the cellular uptake of Onconase, RNase A, and RNase 1. While for Onconase, electrostatic forces are sufficient to cause cell association and internalization, the internalization of other ribonucleases is far greater than expected based on electrostatic forces estimated through computational analysis. Internalization can be increased by substituting positively charged amino acids without affinity for the cell surface with positively charged species with affinity for the cell surface. While this thesis has focused on understanding the cellular uptake of secretory ribonucleases, there are additional areas of

potential import for the development of chemotherapeutics based on ribonucleases, including increasing specificity towards desired cell type and increasing pharmacological half-life.

5.2 Pharmacological Targeting of Ribonucleases

Many older chemotherapeutics target rapidly proliferating cells, resulting in common side effects such as alopecia, nausea, and neutropenia. Interestingly, Onconase does not cause these side effects, suggesting that it is able to target cancer cells specifically.¹⁵⁴ However, the anti-tumoral effectiveness of ONC is limited by dose-limiting reversible renal toxicity. In order to increase the usefulness of ONC, strategies have been developed to increase its tumoral targeting. One of these strategies involves the development of immunoRNases.

ImmunoRNases are RNases that have been conjugated via a linker to an antibody targeting a tumor-associated-antigen present on cancer cell surfaces.¹⁵⁵ Several different immunoRNases have been developed. Onconase was conjugated to an anti-CD22 monoclonal antibody, LL2, resulting in a conjugate which exhibited cytotoxicity towards lymphoma cells at pM concentrations and demonstrated increased specificity in mice.¹⁵⁶ RNase 1 was conjugated to an anti-ErbB2 antibody and demonstrated increased cytotoxicity towards an ErbB2-positive murine cancer line as compared to the anti-ErbB2 antibody and RNase 1 individually.¹⁵⁷ Similar increases in cytotoxicity and specificity have been obtained with conjugates of RNase 1 with anti-CD30 antibodies¹⁵⁸ or with human epidermal growth factor.¹⁵⁹ While immunoRNases demonstrate great potential for targeting tumors clinically,

antibody-based chemotherapeutics can cause severe side effects as they can be highly immunogenic.¹⁶⁰

ImmunoRNases target tumor-associated-antigens on the cell surface but the protein expression profile of malignant cells also differs from normal cells. One example of such a protein is urokinase. Urokinase is a critical component for clot degradation within the coagulative process, but increased tumor expression and concentration of urokinase has been associated with poor clinical outcomes in several types of human cancer, including breast cancer.¹⁶¹ Specifically, urokinase is believed to be important for tumor cell proliferation and metastasis.¹⁶² Small-molecule inhibitors for urokinase could be useful as well as a novel strategy based on the development of a ribonuclease zymogen that would be enzymatically activated by urokinase, resulting in regional specificity.

Zymogens are inactive proteases that become active after an activation process, usually involving cleavage. Several ribonuclease zymogens have been developed that are activated by HIV-protease,¹⁶³ plasmepsin II from *Plasmodium falciparum*,¹⁶⁴ or the NS3 protease of hepatitis C.¹⁶⁵ The zymogens will only be cleaved in cells containing these proteases, resulting in an anti-viral and anti-parasitic therapeutic with high specificity. The three zymogens that were developed previously are based on RNase A and contain a peptide linker between the N and C termini. The peptide linker is between 10–14 amino acids in length and is composed of a protease recognition sequence for cleavage that, ideally, blocks access to the active site in order to abolish ribonucleolytic activity until cleaved by the appropriate protease.

RNase 1 is a promising candidate as a zymogen for urokinase. Because of the numerous design possibilities and questions, computational calculations can be a useful initial step to designing a RNase 1 zymogen. Specifically, explicit MD simulations could be used to test possible locations for the new N and C termini and the length of the peptide linker. Additionally, occlusion of the active site by the peptide linker could be predicted before and after cleavage. This prediction could reveal which zymogens can be expressed as soluble proteins in cells. Such solubility is critical to the development of an RNase 1 zymogen for urokinase as a clinical therapeutic due to the difficulties of purifying zymogens.

5.3 Plasma Clearance of Ribonucleases

Pharmacologic studies have shown only 10% of RNases remain in the plasma after only 15 min due to rapid renal filtration of ribonucleases.⁶⁴ The glomerulus filters proteins that are smaller than 70-kDa for excretion with the amount of protein filtered becoming progressively larger as protein size decreases.¹⁶⁶ Because ONC, RNase A, and RNase 1 range in size from 11.8–14.1 kDa, they are highly susceptible to rapid renal excretion. Several strategies have been developed to increase the pharmacological half-life of ribonucleases. Covalent tethering of ribonucleases to form trimeric conjugates resulted in effective tumor inhibition with decreased frequency of administration and an RNase 1 variant currently in Phase I clinical trials.²⁷ PEGylation of RNase A has been shown to increase circulation time, decrease susceptibility to protease degradation, and recently, to inhibit tumor growth dramatically in

xenograft mice with solid human tumors.¹⁶⁷⁻¹⁶⁹ However, these RNase variants demonstrate decreased cellular uptake due to the significant increase in their size.

Another approach to increasing circulation time could be to engineer ribonucleases that can bind albumin, resulting in a delayed release of the ribonuclease that would then demonstrate normal cellular uptake by tumorous cells. Preliminary results suggested that R-ONC binds bovine and human serum albumin. R-ONC exhibited greater amounts of cellular uptake than ONC in the presence of albumin; however, in the absence of albumin, R-ONC exhibited an even larger increase in internalization whereas ONC showed no difference. Further investigation of R-ONC is necessary as well as investigation of whether other cytotoxic ribonucleases can be engineered to bind albumin. Additionally, studies measuring the circulation time of R-ONC would be fruitful.

REFERENCES

- (1) Membranes: Their Structure, Function, and Chemistry. Becker, W. M.; Kleinsmith, L. J.; Hardin, J. In *The World of the Cell*; 5th ed.; Benjamin Cummings: San Francisco, 2003; Vol. 1, p 158-189.
- (2) Functions of phospholipid flippases. Tanaka, K.; Fujimura-Kamada, K.; Yamamoto, T. *J. Biochem.* **2011**, *149*, 131-143.
- (3) Roles of heparan-sulphate glycosaminoglycans in cancer. Sasisekharan, R.; Shriver, Z.; Venkataraman, G.; Narayanasami, U. *Nat. Rev. Cancer* **2002**, *2*, 521-528.
- (4) Endocytosis. Mukherjee, S.; Ghosh, R. N.; Maxfield, F. R. *Physiol. Rev.* **1997**, *77*, 760-803.
- (5) Mechanisms of phagocytosis in macrophages. Aderem, A.; Underhill, D. M. *Annu. Rev. Immunol.* **1999**, *17*, 593-623.
- (6) Regulated portals of entry into the cell. Conner, S. D.; Schmid, S. L. *Nature* **2003**, *422*, 37-44.
- (7) Heparan sulfate proteoglycan as a plasma membrane carrier. Belting, M. *Trends Biochem Sci* **2003**, *28*, 145-151.
- (8) Cell-penetrating peptides. A reevaluation of the mechanism of cellular uptake. Richard, J. P.; Melikov, K.; Vives, E.; Ramos, C.; Verbeure, B.; Gait, M. J.; Chernomordik, L. V.; Lebleu, B. *J. Biol. Chem.* **2003**, *278*, 585-590.
- (9) Classical electrostatics in biology and chemistry. Honig, B.; Nicholls, A. *Science* **1995**, *268*, 1144-1149.
- (10) Quantitative analysis of the effect of salt concentration on enzymatic catalysis. Park, C.; Raines, R. T. *J. Am. Chem. Soc.* **2001**, *123*, 11472-11479.
- (11) Catalysis by ribonuclease A is limited by the rate of substrate association. Park, C.; Raines, R. T. *Biochemistry* **2002**, *42*, 3509-3518.
- (12) Roles of the hemagglutinin of influenza A virus in viral entry and development of antiviral therapeutics and vaccines. Jiang, S.; Li, R.; Du, L.; Liu, S. *Protein Cell* **2010**, *1*, 342-354.
- (13) Pathway for polyarginine entry into mammalian cells. Fuchs, S. M.; Raines, R. T. *Biochemistry* **2004**, *43*, 2438-2444.
- (14) Polyarginine as a multifunctional fusion tag. Fuchs, S. M.; Raines, R. T. *Protein Sci.* **2005**, *14*, 1538-1544.

- (15) Ribonuclease A variants with potent cytotoxic activity. Leland, P. A.; Schultz, L. W.; Kim, B.-M.; Raines, R. T. *Proc. Natl. Acad. Sci. U.S.A.* **1998**, *98*, 10407-10412.
- (16) The ribonucleolytic activity of angiogenin. Leland, P. A.; Staniszewski, K. E.; Park, C.; Kelemen, B. R.; Raines, R. T. *Biochemistry* **2002**, *41*, 1343-1350.
- (17) Disruption of shape-complementarity markers to create cytotoxic variants of ribonuclease A. Rutkoski, T. J.; Kurten, E. L.; Mitchell, J. C.; Raines, R. T. *J. Mol. Biol.* **2005**, *354*, 41-54.
- (18) Evasion of ribonuclease inhibitor as a determinant of ribonuclease cytotoxicity. Rutkoski, T. J.; Raines, R. T. *Curr. Pharm. Biotechnol.* **2008**, *9*, 185-189.
- (19) Site-directed mutagenesis of histidine-13 and histidine-114 of human angiogenin. Alanine derivatives inhibit angiogenin-induced angiogenesis. Shapiro, R.; Vallee, B. L. *Biochemistry* **1989**, *28*, 7401-7408.
- (20) Recombinant human eosinophil cationic protein. Ribonuclease activity is not essential for cytotoxicity. Rosenberg, H. F. *J. Biol. Chem.* **1995**, *270*, 7876-7881.
- (21) Natural and engineered ribonucleases as potential cancer therapeutics. Arnold, U.; Ulbrich-Hofmann, R. *Biotechnol. Lett.* **2006**, *28*, 1615-1622.
- (22) Ribonucleases as novel chemotherapeutics: The ranpirnase example. Lee, J. E.; Raines, R. T. *BioDrugs* **2008**, *22*, 53-58.
- (23) Cytostatic and cytotoxic effect of Pannon (P-30 Protein), a novel anticancer agent. Darzynkiewicz, Z.; Carter, S. P.; Mikulski, S. M.; Ardelt, W. J.; Shogen, K. *Cell Tissue Kinet.* **1988**, *21*, 169-182.
- (24) Ribonuclease inhibitor as an intracellular sentry. Haigis, M. C.; Kurten, E. L.; Raines, R. T. *Nucleic Acids Res.* **2003**, *31*, 1024-1032.
- (25) Mechanism of ribonuclease inhibition by ribonuclease inhibitor protein based on the crystal structure of its complex with ribonuclease A. Kobe, B.; Deisenhofer, J. *J. Mol. Biol.* **1996**, *264*, 1028-1043.
- (26) Inhibition of human pancreatic ribonuclease by the human ribonuclease inhibitor protein. Johnson, R. J.; McCoy, J. G.; Bingman, C. A.; Phillips, G. N., Jr.; Raines, R. T. *J. Mol. Biol.* **2007**, *367*, 434-449.
- (27) Antitumor activity of ribonuclease multimers created by site-specific covalent tethering. Rutkoski, T. J.; Kink, J. A.; Strong, L. E.; Schilling, C. I.; Raines, R. T. *Bioconjugate Chem.* **2010**, *21*, 1691-1702.

- (28) Ribonucleases as a novel pro-apoptotic anticancer strategy: Review of the preclinical and clinical data for ranpirnase. Costanzi, J.; Sidransky, D.; Navon, A.; Goldsweig, H. *Cancer Invest.* **2005**, *23*, 643-650.
- (29) Cytotoxic ribonucleases: The dichotomy of Coulombic forces. Johnson, R. J.; Chao, T.-Y.; Lavis, L. D.; Raines, R. T. *Biochemistry* **2007**, *46*, 10308-10316.
- (30) Cellular uptake of Ribonuclease A relies on anionic glycans. Chao, T. Y.; Lavis, L. D.; Raines, R. T. *Biochemistry* **2010**, *49*, 10666-10673.
- (31) Comparison of RNases and toxins upon injection into *Xenopus* oocytes. Saxena, S. K.; Rybak, S. M.; Winkler, G.; Meade, H. M.; McGray, P.; Youle, R. J.; Ackerman, E. J. *J. Biol. Chem.* **1991**, *266*, 21208-21214.
- (32) Secretory ribonucleases are internalized by a dynamin-independent endocytic pathway. Haigis, M. C.; Raines, R. T. *J. Cell Sci.* **2003**, *116*, 313-324.
- (33) Intracellular pathway of Onconase that enables its delivery to the cytosol. Rodriguez, M.; Torrent, G.; Bosch, M.; Rayne, F.; Dubremetz, J.-F.; Ribó, M.; Benito, A.; Vilanova, M.; Beaumelle, B. *J. Cell Sci.* **2007**, *120*, 1405-1411.
- (34) A cytotoxic ribonuclease. Study of the mechanism of onconase cytotoxicity. Wu, Y.; Mikulski, S. M.; Ardelt, W.; Rybak, S. M.; Youle, R. J. *J. Biol. Chem.* **1993**, *268*, 10686-10693.
- (35) Onconase cytotoxicity relies on the distribution of its positive charge. Turcotte, R. F.; Lavis, L. D.; Raines, R. T. *FEBS J.* **2009**, *276*, 3846-3857.
- (36) Preparation of potent cytotoxic ribonucleases by cationization: Enhanced cellular uptake and decreased interaction with ribonuclease inhibitor by chemical modification of carboxyl groups. Futami, J.; Maeda, T.; Kitazoe, M.; Nukui, E.; Tada, H.; Seno, M.; Kosaka, M.; Yamada, H. *Biochemistry* **2001**, *26*, 7518-7524.
- (37) Increasing the potency of a cytotoxin with an arginine graft. Fuchs, S. M.; Rutkoski, T. J.; Kung, V. M.; Groeschl, R. T.; Raines, R. T. *Protein Eng. Des. Select.* **2007**, *20*, 505-509.
- (38) Endocytotic internalization as a crucial factor for the cytotoxicity of ribonucleases. Leich, F.; Stohr, N.; Rietz, A.; Ulbrich-Hofmann, R.; Arnold, U. *J. Biol. Chem.* **2007**, *282*, 27640-27646.
- (39) A nuclear localization sequence endows human pancreatic ribonuclease with cytotoxic activity. Bosch, M.; Benito, A.; Ribó, M.; Puig, T.; Beaumelle, B.; Vilanova, M. *Biochemistry* **2004**, *43*, 2167-2177.

- (40) The role of electrostatic interactions in the antitumor activity of dimeric RNases. Notomista, E.; Mancheño, J. M.; Crescenzi, O.; Di Donato, A.; Gavilanes, J.; D'Alessio, G. *FEBS J.* **2006**, *273*, 3687-3697.
- (41) Both aromatic and cationic residues contribute to the membrane-lytic and bactericidal activity of eosinophil cationic protein. Carreras, E.; Rosenberg, H. F.; Cuchillo, C. M.; Nogués, M. V. *Biochemistry* **2003**, *42*, 6636-6646.
- (42) Comparison of the membrane interaction mechanism of two antimicrobial RNases: RNase 3/ECP and RNase 7. Torrent, M.; Sánchez, D.; Buzón, V.; Nogués, V.; Cladera, J.; Boix, E. *Biochim. Biophys. Acta* **2009**, *1788*, 1116-1125.
- (43) A comprehensive model for the cellular uptake of cationic cell-penetrating peptides. Duchardt, F.; Fotin-Mleczek, M.; Schwarz, H.; Fischer, R.; Brock, R. *Traffic* **2007**, *8*, 849-866.
- (44) Barrel-stave model or toroidal model? A case study on melittin pores. Yang, L.; Harroun, T. A.; Weiss, T. M.; Ding, L.; Huang, H. W. *Biophys. J.* **2001**, *81*, 1475-1485.
- (45) Structure-Activity relationship of truncated and substituted analogues of the intracellular delivery vector Penetratin. Fischer, P. M.; Zhelev, N. Z.; Wang, S.; Melville, J. E.; Fahraeus, R.; Lane, D. P. *J. Pept. Res.* **2000**, *55*, 163-172.
- (46) The Antennapedia peptide penetratin translocates across lipid bilayers—the first direct observation. Thoren, P. E.; Persson, D.; Karlsson, M.; Norden, B. *FEBS Lett.* **2000**, *482*, 265-268.
- (47) Mechanisms of antimicrobial, cytolytic, and cell-penetrating peptides: From kinetics to thermodynamics. Almeida, P. F.; Pokorny, A. *Biochemistry* **2009**, *48*, 8083-8093.
- (48) Antimicrobial peptides in toroidal and cylindrical pores. Mihajlovic, M.; Lazaridis, T. *Biochim. Biophys. Acta* **2010**, *1798*, 1485-1493.
- (49) Distribution of amino acids in a lipid bilayer from computer simulations. MacCallum, J. L.; Bennett, W. F. D.; Tieleman, D. P. *Biophys. J.* **2008**, *94*, 3393-3404.
- (50) An exciting but challenging road ahead for computational enzyme design. Baker, D. *Protein Sci.* **2010**, *19*, 1817-1819.
- (51) Atomistic protein folding simulations on the submillisecond time scale using worldwide distributed computing. Pande, V. S.; Baker, I.; Chapman, J.; Elmer, S. P.; Khaliq, S.; Larson, S. M.; Rhee, Y. M.; Shirts, M. R.; Snow, C. D.; Sorin, E. J.; Zagrovic, B. *Biopolymers* **2003**, *68*, 91-109.

- (52) Reaching biological timescales with all-atom molecular dynamics simulations. Zwier, M. C.; Chong, L. T. *Curr. Opin. Pharmacol.* **2010**, *10*, 745-752.
- (53) Electrostatics in biomolecular structure and dynamics. Davis, M. E.; McCammon, J. A. *Chem. Rev.* **1990**, *90*, 509-521.
- (54) Bridging implicit and explicit solvent approaches for membrane electrostatics. Lin, J. H.; Baker, N. A.; McCammon, J. A. *Biophys. J.* **2002**, *83*, 1374-1379.
- (55) Poisson-Boltzmann solvents in molecular dynamics simulations. Wang, J.; Tan, C.; Tan, Y. H.; Lu, Q.; Luo, R. *Comm. Comp. Phys.* **2008**, *3*, 1010-1031.
- (56) Atomic structure of a voltage-dependent K⁺ channel in a lipid membrane-like environment. Long, S. B.; Tao, X.; Campbell, E. B.; MacKinnon, R. *Nature* **2007**, *450*, 376-382.
- (57) Prediction of protein orientation upon immobilization on biological and nonbiological surfaces. Talasz, A.; Davis, R. *Proc. Natl. Acad. Sci. U.S.A.* **2006**, *103*, 14773-14778.
- (58) A continuum method for determining membrane protein insertion energies and the problem of charged residues. Choe, S.; Hecht, K. A.; Grabe, M. *J. Gen. Physiol.* **2008**, *131*, 563-573.
- (59) Implicit solvent simulations of peptide interactions with anionic lipid membranes. Lazaridis, T. *Proteins* **2005**, *58*, 518-527.
- (60) On the track of antitumor ribonucleases. Benito, A.; Ribó, M.; Vilanova, M. *Mol. Biosyst.* **2005**, *1*, 294-302.
- (61) Ribonucleases as potential modalities in anticancer therapy. Ardelt, W.; Ardelt, B.; Darzynkiewicz, Z. *Eur. J. Pharm.* **2009**, *625*, 181-189.
- (62) Ribonucleases of different origins with a wide spectrum of medicinal applications. Fang, E. F.; Ng, T. B. *Biochim. Biophys. Acta* **2011**, *15*, 65-74.
- (63) Cellular uptake of ribonuclease A relies on anionic glycans. Chao, T. Y.; Lavis, L. D.; Raines, R. T. *Biochemistry* **2010**, *49*, 10666-73.
- (64) Molecular determinants in the plasma clearance and tissue distribution of ribonucleases of the ribonuclease A superfamily. Vasandani, V. M.; Wu, Y.-N.; Mikulski, S. M.; Youle, R. J.; Sung, C. *Cancer Res.* **1996**, *56*, 4180-4186.
- (65) Reversible nephrotoxicity of onconase and effect of lysine pH on renal onconase uptake. Vasandani, V. M.; Burris, J. A.; Sung, C. *Cancer Ther. Pharmacol.* **1999**, *44*, 164-169.

- (66) The third helix of the Antennapedia homeodomain translocates through biological membranes. Derossi, D.; Joliot, A. H.; Chassaing, G.; Prochiantz, A. *J. Biol. Chem.* **1994**, *269*, 10444-10450.
- (67) A truncated HIV-1 Tat protein basic domain rapidly translocates through the plasma membrane and accumulates in the cell nucleus. Vives, E.; Brodin, P.; Lebleu, B. *J. Biol. Chem.* **1997**, *272*, 16010-16017.
- (68) Stimulated endocytosis in penetratin uptake: Effect of arginine and lysine. Amand, H.; Fant, K.; Norden, B.; Esbjorner, E. *Biochem. Biophys. Res. Commun.* **2008**, *371*, 621-625.
- (69) Polyarginine enters cells more efficiently than other polycationic homopolymers. Mitchell, D. J.; Kim, D. T.; Steinman, L.; Fathman, C. G.; Rothbard, J. B. *J. Pept. Res.* **2000**, *56*, 318-325.
- (70) Roles of arginine and lysine residues in the translocation of a cell-penetrating peptide from ^{13}C , ^{31}P , and ^{19}F solid-state NMR. Su, Y.; Doherty, T.; Waring, A. J.; Ruchala, P.; Hong, M. *Biochemistry* **2009**, *48*, 4587-4595.
- (71) Optimum modification for the highest cytotoxicity of cationized ribonuclease. Futami, J.; Nukui, K.; Maeda, T.; Kosaka, M.; Tada, H.; Seno, M.; Yamada, H. *J. Biochem. (Tokyo)* **2002**, *132*, 223-228.
- (72) Design of cytotoxic ribonucleases by cationization to enhance intracellular protein delivery. Futami, J.; Yamada, H. *Curr. Pharm. Biotechnol.* **2008**, *9*, 180-184.
- (73) Arginine grafting to endow cell permeability. Fuchs, S. M.; Raines, R. T. *ACS Chem. Biol.* **2007**, *2*, 167-170.
- (74) Potent delivery of functional proteins into mammalian cells in vitro and in vivo using a supercharged protein. Cronican, J. J.; Thompson, D. B.; Beier, K. T.; McNaughton, B. R.; Cepko, C. L.; Liu, D. R. *ACS Chem. Biol.* **2010**, *5*, 747-752.
- (75) Effect of replacing the aspartic acid/glutamic acid residues of bullfrog sialic acid binding lectin with asparagine/glutamine and arginine on the inhibition of cell proliferation in murine leukemia P388 cells. Ogawa, Y.; Iwama, M.; Ohgi, K.; Tsuji, T.; Irie, M.; Itagaki, T.; Kobayashi, H.; Inokuchi, N. *Biol. Pharm. Bull.* **2002**, *25*, 722-727.
- (76) Onconase cytotoxicity relies on the distribution of its positive charge. Turcotte, R. F.; Lavis, L. D.; Raines, R. T. *FEBS J.* **2009**, *276*, 4270-4281.

- (77) Refined 1.7 Å X-ray crystallographic structure of P-30 protein, an amphibian ribonuclease with anti-tumor activity. Mosimann, S. C.; Ardelt, W.; James, M. N. G. *J. Mol. Biol.* **1994**, *236*, 1141-1153.
- (78) Amino acid sequence of an anti-tumor protein from *Rana pipiens* oocytes and early embryos. Ardelt, W.; Mikulski, S. M.; Shogen, K. *J. Biol. Chem.* **1991**, *266*, 245-251.
- (79) Potent inhibition of ribonuclease A by oligo(vinylsulfonic acid). Smith, B. D.; Soellner, M. B.; Raines, R. T. *J. Biol. Chem.* **2003**, *278*, 20934-20938.
- (80) Fluorogenic label for biomolecular imaging. Lavis, L. D.; Chao, T.-Y.; Raines, R. T. *ACS Chem. Biol.* **2006**, *1*, 252-260.
- (81) Contribution of active-site residues to the function of onconase, a ribonuclease with antitumoral activity. Lee, J. E.; Raines, R. T. *Biochemistry* **2003**, *42*, 11443-11450.
- (82) Contribution of structural peculiarities of onconase to its high stability and folding kinetics. Arnold, U.; Schulenburg, C.; Schmidt, D.; Ulbrich-Hofmann, R. *Biochemistry* **2006**, *45*, 3580-3587.
- (83) Two new staining procedures for quantitative estimation of proteins on electrophoretic strips. de St. Groth, S. F.; Webster, R. G.; Datyner, A. *Biochim. Biophys. Acta* **1963**, *3883*, 377-391.
- (84) Catalytic activity of bovine seminal ribonuclease is essential for its immunosuppressive and other biological activities. Kim, J.-S.; Souček, J.; Matoušek, J.; Raines, R. T. *Biochem. J.* **1995**, *308*, 547-550.
- (85) The interdependence between catalytic activity, conformational stability, and cytotoxicity of onconase. Schulenburg, C.; Ardelt, B.; Ardelt, W.; Arnold, U.; Shogen, K.; Ulbrich-Hoffmann, R.; Darzynkiewicz, Z. *Cancer Biol. Ther.* **2008**, *6*, 1233-1239.
- (86) Urea and guanidine hydrochloride denaturation curves. Shirley, B. A. *Methods Mol. Biol.* **1995**, *40*, 177-190.
- (87) Side-chain hydrophobicity scale derived from transmembrane protein folding into lipid bilayers. Moon, C. P.; Fleming, K. G. *Proc. Natl. Acad. Sci.* **2011**, *108*, 10174-10177.
- (88) Onconase: An unusually stable protein. Notomista, E.; Catanzano, F.; Graziano, G.; Piazz, F. D.; Barone, G.; D'Alessio, G.; Donato, A. D. *Biochemistry* **2000**, *39*, 8711-8718.

- (89) Thermal unfolding of eosinophil cationic protein/ribonuclease 3: A nonreversible process. Nikolovski, Z.; Buzón, V.; Ribó, M.; Moussaoui, M.; Vilanova, M.; Cuchillo, C. M.; Cladera, J.; Nogués, M. V. *Protein Sci.* **2006**, *15*, 2816-2827.
- (90) Endocytotic internalization as a crucial factor for the cytotoxicity of ribonucleases. Leich, F.; Stöhr, N.; Reitz, A.; Ulbrich-Hofmann, R.; Arnold, U. *J. Biol. Chem.* **2007**, *282*, 27640-27646.
- (91) Contribution of chain termini to the conformational stability and biological activity of onconase. Notomista, E.; Catanzano, F.; Graziano, G.; Di Gaetano, S.; Barone, G.; Di Donato, A. *Biochemistry* **2001**, *40*, 9097-103.
- (92) Effects of protein RNase inhibitor and substrate on the quaternary structures of bovine seminal RNase. Murthy, B. S.; De Lorenzo, C.; Piccoli, R.; D'Alessio, G.; Sirdeshmukh, R. *Biochemistry* **1996**, *35*, 3880-3885.
- (93) Tight-binding inhibition of angiogenin and ribonuclease A by placental ribonuclease inhibitor. Lee, F. S.; Shapiro, R.; Vallee, B. L. *Biochemistry* **1989**, *28*, 225-230.
- (94) Mechanism of ribonuclease A endocytosis: Analogies to cell-penetrating peptides. Chao, T. Y.; Raines, R. T. *Biochemistry* **2011**, *50*, 8374-8382.
- (95) Engineering receptor-mediated cytotoxicity into human ribonucleases by steric blockage of inhibitor interaction. Suzuki, M.; Saxena, S. K.; Boix, E.; Prill, R. J.; Vasandani, V. M.; Ladner, J. E.; Sung, C.; Youle, R. J. *Nat. Biotechnol.* **1999**, *17*, 265-270.
- (96) Electrostatics of nanosystems: application to microtubules and the ribosome. Baker, N. A.; Sept, D.; Joseph, S.; Holst, M. J.; McCammon, J. A. *Proc. Natl. Acad. Sci. USA* **2001**, *98*, 10037-10041.
- (97) Atomic resolution structures of ribonuclease A at six pH values. Berisio, R.; Sica, F.; Lamzin, V. S.; Wilson, K. S.; Zagari, A.; Mazzarella, L. *Acta Crystallogr., Sect. D* **2002**, *58*, 441-450.
- (98) All-atom empirical potential for molecular modeling and dynamics studies of proteins. MacKerell, A. D.; Bashford, D.; Bellott, M.; Dunbrack, R. L.; Evanseck, J. D.; Field, M. J.; Fischer, S.; Gao, J.; Guo, H.; Ha, S.; Joseph-McCarthy, D.; Kuchnir, L.; Kuczera, K.; Lau, F. T. K.; Mattos, C.; Michnick, S.; Ngo, T.; Nguyen, D. T.; Prodhom, B.; Reiher, W. E.; Roux, B.; Schlenkrich, M.; Smith, J. C.; Stote, R.; Straub, J.; Watanabe, M.; Wiorkiewicz-Kuczera, J.; Yin, D.; Karplus, M. *J. Phys. Chem. B* **1998**, *102*, 3586-3616.

- (99) PDB2PQR: An automated pipeline for the setup, execution, and analysis of Poisson–Boltzmann electrostatics calculations. Dolinsky, T. J.; Nielsen, J. E.; McCammon, J. A.; Baker, N. A. *Nucleic Acids Res.* **2004**, *32*, W665–W667.
- (100) PDB2PQR: Expanding and upgrading automated preparation of biomolecular structures for molecular simulations. Dolinsky, T. J.; Czodrowski, P.; Li, H.; Nielsen, J. E.; Jensen, J. H.; Klebe, G.; Baker, N. A. *Nucleic Acids Res.* **2007**, *35*, W522–W525.
- (101) Effective energy function for proteins in solution. Lazaridis, T.; Karplus, M. *Proteins* **1999**, *35*, 133–152.
- (102) The electrostatic properties of membranes. McLaughlin, S. *Annu. Rev. Biophys. Biophys. Chem.* **1989**, *18*, 113–136.
- (103) CHARMM: A program for macromolecular energy, minimization, and dynamics calculations. Brooks, B. R.; Brucoleri, R. E.; Olafson, B. D.; States, D. J.; Swaminathan, S.; Karplus, M. *J. Comput. Chem.* **1983**, *4*, 187–217.
- (104) Increased exposure of anionic phospholipids on the surface of tumor blood vessels. Ran, S.; Downes, A.; Thorpe, P. E. *Cancer Res.* **2002**, *62*, 6132–6140.
- (105) Aspects of the cytotoxic action of ribonucleases. Arnold, U. *Curr. Pharm. Biotechnol.* **2008**, *9*, 161–168.
- (106) Cellular catabolism of heparan sulfate proteoglycans. Yanagishita, M. *Trends in Glycoscience and Glycotechnology* **1998**, *10*, 57–63.
- (107) *Molecular Biology of the cell*. Alberts, B.; Bray, D.; Lewis, J.; Raff, M.; Roberts, K.; Watson, J. D.; Garland Publishing, Inc.: New York, 1994.
- (108) DNA polymerase-III holoenzyme of *Escherichia coli*. McHenry, C. S. *Annu. Rev. Biochem.* **1988**, *57*, 519–550.
- (109) Minor groove-binding architectural proteins: Structure, function, and DNA recognition. Bewley, C. A.; Gronenborn, A. M.; Clore, G. M. *Annu. Rev. Biophys. Biomol. Struct.* **1998**, *27*, 105–131.
- (110) Making DNA do a U-turn: IHF and related proteins. Rice, P. A. *Curr. Opin. Struct. Biol.* **1997**, *7*, 86–93.
- (111) IHF and HU: Flexible architects of bent DNA. Swinger, K. K.; Rice, P. A. *Curr. Opin. Struct. Biol.* **2004**, *14*, 28–35.
- (112) Electrostatic mechanisms of DNA deformation. Williams, L. D. *Annu. Rev. Biophys. Biomol. Struct.* **2000**, *29*, 497–521.

- (113) A computational framework for mechanical response of macromolecules: Application to the salt concentration dependence of DNA bendability. Ma, L.; Yethiraj, A.; Chen, X.; Cui, Q. *Biophys. J.* **2009**, *96*, 3543-3554.
- (114) Crystal structure of an IHF-DNA complex: A protein-induced DNA U-turn. Rice, P. A.; Yang, S. W.; Mizuuchi, K.; Nash, H. A. *Cell* **1996**, *87*, 1295-1306.
- (115) Specific and non-specific interactions of integration host factor with DNA: Thermodynamic evidence for disruption of multiple IHF surface salt-bridges coupled to DNA binding. Holbrook, J. A.; Tsodikov, O. V.; Saecker, R. M.; Record, M. T., Jr. *J. Mol. Biol.* **2001**, *310*, 379-401.
- (116) Structural features of protein-nucleic acid recognition sites. Nadassy, K.; Wodak, S. J.; Janin, J. *Biochemistry* **1999**, *38*, 1999-2017.
- (117) Two exposed amino acid residues confer thermostability on a cold shock protein. Perl, D.; Mueller, U.; Heinemann, U.; Schmid, F. X. *Nat. Struct. Biol.* **2000**, *7*, 380-383.
- (118) Protein surface salt bridges and paths for DNA wrapping. Saecker, R. M.; Record, M. T., Jr. *Curr. Opin. Struct. Biol.* **2002**, *12*, 311-319.
- (119) The role of surface-exposed lysines in wrapping DNA about the bacterial histone-like protein HU. Grove, A.; Saavedra, T. C. *Biochemistry* **2002**, *41*, 7597-7603.
- (120) Surface salt bridges modulate DNA wrapping by the type II DNA-binding protein TF1. Grove, A. *Biochemistry* **2003**, *42*, 8739-8747.
- (121) Contributions of engineered surface salt bridges to the stability of t4 lysozyme determined by directed mutagenesis. Daopin, S.; Sauer, U.; Nicholson, H.; Matthews, B. W. *Biochemistry* **1991**, *30*, 7142-7153.
- (122) Contribution of surface salt bridges to protein stability. Strop, P.; Mayo, S. L. *Biochemistry* **2000**, *30*, 7142-7153.
- (123) Direct observation of salt effects on molecular interactions through explicit-solvent molecular dynamics simulations: Differential effects on electrostatic and hydrophobic interactions and comparisons to Poisson-Boltzmann theory. Thomas, A. S.; Elcock, A. H. *J. Am. Chem. Soc.* **2006**, *128*, 7796-7806.
- (124) Formation of a wrapped DNA-protein interface: Experimental characterization and analysis of the large contributions of ions and water to the thermodynamics of binding IHF to H' DNA. Meulen, K. A. V.; Saecker, R. M.; Record, M. T., Jr. *J. Mol. Biol.* **2008**, *377*, 9-27.

- (125) Gromacs 3.0: A package for molecular simulation and trajectory analysis. Lindahl, E.; Hess, B.; van der Spoel, D. *J. Mol. Model.* **2001**, *7*, 306-317.
- (126) Gromacs: A message-passing parallel molecular-dynamics implementation. Berendsen, H. J. C.; Vanderspoel, D.; Vandrunen, R. *Comput. Phys. Commun.* **1995**, *91*, 43-56.
- (127) The OPLS potential functions for proteins: Energy minimizations for crystals of cyclic-peptides and crambin. Jorgensen, W. L.; Tiradorives, J. *J. Am. Chem. Soc.* **1988**, *110*, 1657-1666.
- (128) Comparison of simple potential functions for simulating liquid water. Jorgensen, W. L.; Chandrasekhar, J.; Madura, J. D.; Impey, R. W.; Klein, M. L. *J. Chem. Phys.* **1983**, *79*, 926-935.
- (129) A smooth particle mesh ewald method. Essmann, U.; Perera, L.; Berkowitz, M. L.; Darden, T.; Lee, H.; Pedersen, L. G. *J. Chem. Phys.* **1995**, *103*, 8577-8593.
- (130) New spherical-cutoff methods for long-range forces in macromolecular simulation. Steinbach, P. J.; Brooks, B. R. *J. Comput. Chem.* **1994**, *15*, 667-683.
- (131) Settle: An analytical version of the shake and rattle algorithm for rigid water models. Miyamoto, S.; Kollman, P. A. *J. Comput. Chem.* **1992**, *13*, 952-962.
- (132) Numerical-integration of cartesian equations of motion of a system with constraints: Molecular-dynamics of *n*-alkanes. Ryckaert, J. P.; Ciccotti, G.; Berendsen, H. J. C. *J. Comput. Phys.* **1977**, *23*, 327-341.
- (133) A unified formulation of the constant temperature molecular-dynamics methods. Nose, S. *J. Chem. Phys.* **1984**, *81*, 511-519.
- (134) Canonical dynamics: Equilibrium phase-space distributions. Hoover, W. G. *Phys. Rev. A* **1985**, *31*, 1695-1697.
- (135) Molecular dynamics with coupling to an external bath. Berendsen, H. J. C.; Postma, J. P. M.; Vangunsteren, W. F.; Dinola, A.; Haak, J. R. *J. Chem. Phys.* **1984**, *81*, 3684-3690.
- (136) Factors influencing the energetics of electron and proton transfers in proteins. What can be learned from calculations? Gunner, M. R.; Mao, J.; Song, Y.; Kim, J. *Biochim. Biophys. Acta* **2006**, *1757*, 942-968.
- (137) Very fast empirical prediction and interpretation of protein pK_a values. Li, H.; Robertson, A. D.; Jensen, J. H. *Proteins: Struct., Funct., Bioinf.* **2005**, *73*, 765-783.

- (138) Very fast prediction and rationalization of pK_a values for protein-ligand complexes. Bas, D. C.; Rogers, D. M.; Jensen, J. H. *Proteins: Struct., Funct., Bioinf.* **2008**, *73*, 765-783.
- (139) Electronic continuum model for molecular dynamics simulations of biological molecules. Leontyev, I. V.; Stuchebrukhov, A. A. *J. Chem. Theory Comput.* **2010**, *6*, 1498-1508.
- (140) Many-body polarization effects and the membrane dipole potential. Harder, E.; MacKerell, A. D., Jr.; Roux, B. *J. Am. Chem. Soc.* **2009**, *131*, 2760-2761.
- (141) Calculation of protein-ligand binding free energy by using a polarizable potential. Jiao, D.; Golubkov, P. A.; Darden, T. A.; Ren, P. *Proc. Natl. Acad. Sci. U.S.A.* **2008**, *105*, 6290-6295.
- (142) Optimized atomic radii for protein continuum electrostatics solvation forces. Nina, M.; Im, W.; Roux, B. *Biophys. Chem.* **1999**, *78*, 89-96.
- (143) Patch Finder Plus (PFplus): A web server for extracting and displaying positive electrostatic patches on protein surfaces. Shazman, S.; Celniker, G.; Haber, O.; Glaser, F.; Mandel-Gutfreund, Y. *Nucleic Acid Res.* **2007**, *35*, W526-W530.
- (144) PreDs: A server for predicting dsDNA-binding site on protein molecular surfaces. Tsuchiya, Y.; Kinoshita, K.; Nakamura, H. *Bioinformatics* **2005**, *21*, 1721-1723.
- (145) Structure-based prediction of DNA-binding sites on proteins using the empirical preference of electrostatic potential and the shape of molecular surfaces. Tsuchiya, Y.; Kinoshita, K.; Nakamura, H. *Proteins: Struct., Funct., Bioinf.* **2004**, *55*, 885-894.
- (146) Coupling of local folding to site-specific binding of proteins to DNA. Spolar, R. S.; Record, M. T., Jr. *Science* **1994**, *263*, 777-784.
- (147) Ion-pairs in proteins. Barlow, D. J.; Thornton, J. M. *J. Mol. Biol.* **1983**, *168*, 867-885.
- (148) Some factors in interpretation of protein denaturation. Kauzmann, W. *Adv. Protein Chem.* **1959**, *14*, 1-57.
- (149) Sequence-based prediction of DNA-binding sites on DNA-binding proteins. Gou, Z.; Hwang, S.; Kuznetsov, B. I. In *Proceedings of the Fifth International Conference on Bioinformatics of Genome Regulation and Structure 2006*; Vol. 1, p 268-271.
- (150) DISPLAR: An accurate method for predicting DNA-binding sites on protein surfaces. Tjong, H.; Zhou, H. X. *Nucleic Acids Res.* **2007**, *35*, 1465-1477.

- (151) Annotating nucleic acid-binding function based on protein structure. Stawiski, E. W.; Gregoret, L. M.; Mandel-Gutfreund, Y. *J. Mol. Biol.* **2003**, *326*, 1065-1079.
- (152) VMD: Visual Molecular Dynamics. Humphrey, W.; Dalke, A.; Schulten, K. *J. Mol. Graphics* **1996**, *14*, 33-38.
- (153) Intracellular delivery of proteins into mammalian living cells by Polyethylenimine-cationization. Futami, J.; Kitazoe, M.; Maeda, T.; Nukui, E.; Sakaguchi, M.; Kosaka, J.; Miyazaki, M.; Kosaka, M.; Tada, H.; Seno, M.; Sasaki, J.; Huh, N. H.; Namba, M.; Yamada, H. *J. Biosci. Bioeng.* **2005**, *99*, 95-103.
- (154) Ribonucleases as a novel pro-apoptotic anticancer strategy: Review of the preclinical and clinical data for ranpirnase. Costanzi, J.; Sidransky, D.; Navon, A.; Goldsweig, H. *Cancer Invest.* **2005**, *23*, 643-650.
- (155) From ImmunoToxins to ImmunoRNases. De Lorenzo, C.; D'Alessio, G. *Curr. Pharm. Biotechnol.* **2008**, *9*, 210-214.
- (156) Potent and specific antitumor effects of an anti-CD22-targeted cytotoxic ribonuclease: potential for the treatment of non-Hodgkin lymphoma. Newton, D. L.; Hansen, H. J.; Mikulski, S. M.; Goldenberg, D. M.; Rybak, S. M. *Blood* **2001**, *97*, 528-535.
- (157) A novel fully human antitumour immunoRNase targeting ErbB2-positive tumours. Borriello, M.; Laccetti, P.; Terrazzano, G.; D'Alessio, G.; De Lorenzo, C. *Brit. J. Cancer* **2011**, *104*, 1716-1723.
- (158) New anti-CD30 human pancreatic ribonuclease-based immunotoxin reveals strong and specific cytotoxicity *in vivo*. Braschoss, S.; Hirsch, B.; Dübel, S.; Stein, H.; Dürkop, H. *Leuk. Lymph.* **2007**, *2007*, 1179-1186.
- (159) Human pancreatic RNase1-human epidermal growth factor fusion: an entirely human 'immunotoxin analog' with cytotoxic properties against squamous cell carcinomas. Psarras, K.; Ueda, M.; Yamamura, T.; Ozawa, S.; Kitajima, M.; Aiso, S.; Komatsu, S.; Seno, M. *Protein Eng.* **1998**, *11*, 1285-1292.
- (160) Ribonucleases and ImmunoRNases as Anticancer Drugs. Rybak, S. M.; Arndt, M. A. E.; Schirrmann, T.; Dübel, S.; Krauss, J. *Curr. Pharm. Des.* **2009**, *15*, 2665-2675.
- (161) The urokinase plasminogen activator system: A target for anti-cancer therapy. Ullisse, S.; Baldini, E.; Sorrenti, S.; D'Armiento, M. *Curr. Cancer Drug Targets* **2009**, *9*, 32-71.
- (162) Extracellular proteases as targets for drug development. Cudic, M.; Fields, G. B. *Curr. Protein Pept. Sci.* **2009**, *10*, 297-307.

- (163) Design and characterization of an HIV-specific ribonuclease zymogen. Turcotte, R. F.; Raines, R. T. *AIDS Res. Human Retrovir.* **2008**, *24*, 1357-1363.
- (164) Creation of a zymogen. Plainkum, P.; Fuchs, S. M.; Wiyakrutta, S.; Raines, R. T. *Nat. Struct. Biol.* **2003**, *10*, 115-119.
- (165) A ribonuclease zymogen activated by the NS3 protease of the hepatitis C virus. Johnson, R. J.; Lin, S. R.; Raines, R. T. *FEBS J.* **1006**, 273, 5457-5465.
- (166) *Vander's Renal Physiology*. Eaton, D. C.; Pooler, J. P.; 6 ed.; McGraw-Hill, 2004.
- (167) Surface modification of enzymes for therapeutic use: Monomethoxypoly(ethylene glycol) derivatization of ribonuclease. Schiavon, O.; Caliceti, P.; Sartore, L.; Veronese, F. M. *Farmaco* **1991**, *46*, 967-978.
- (168) A branched monomethoxypoly(ethylene glycol) for protein modification. Monfardini, C.; Schiavon, O.; Caliceti, P.; Morpurgo, M.; Harris, J. M.; Veronese, F. M. *Bioconjugate Chem.* **1995**, *6*, 62-69.
- (169) Site-specific PEGylation endows a mammalian ribonuclease with antitumor activity. Rutkoski, T. J.; Kink, J. A.; Strong, L. E.; Raines, R. T. *Cancer Biol. Ther.* **2011**, *12*, 208-214.